The interactions between ocean, ice shelves and sea ice in the southeastern Amundsen Sea

A thesis submitted to the School of Environmental Sciences at
the University of East Anglia in partial fulfilment of the
requirements for the degree of Doctor of Philosophy

Yixi Zheng

1-September-2022

© This copy of the thesis has been supplied on condition that anyone who consults it is understood to recognise that its copyright rests with the author and that use of any information derived there from must be in accordance with current UK Copyright Law. In addition, any quotation or extract must include full attribution.

Abstract

Ice shelves buttressing the Antarctic Ice Sheet are losing mass rapidly mainly due to oceanic melt. In this thesis, I study the interactions between ocean, ice shelf, and sea ice in the southeastern Amundsen Sea, where the strongest melt has been reported, using multi-platform observations and idealised models, proposing physical mechanisms controlling those interactions.

This thesis presents the first winter meltwater distribution near Pine Island Ice Shelf, using hydrographic profiles collected by tagged seals, revealing a highly variable meltwater distribution, with two meltwater-rich layers connected by irregularly-spaced meltwater-rich columns. Year-round observations demonstrate that, due to the reduced vertical stratification, a substantial proportion of the meltwater rises to the surface in winter without undergoing intense mixing, providing near-surface heat to maintain polynyas, and nutrients to boost marine production. Velocity measurements in 2019 reveal, for the first time, a small ocean gyre in a habitually ice-covered region to the west of Thwaites Ice Shelf. This gyre rotates anti-cyclonically, despite the climatologically cyclonic wind stress curl in the Amundsen Sea. This thesis uses an idealised barotropic model to reproduce key features of the observed gyres. It shows that the presence of sea ice and/or ice shelves alters the magnitude of the integrated ocean surface stress curl, and hence regulates ocean gyre direction and strength, potentially allowing the gyre to rotate in the opposite sense to the wind stress curl.

The first full-depth well-resolved hydrographic time series in the Amundsen Sea

Polynya, sampled in autumn 2014, reveals intense mixed-layer cooling, salinification and deepening, with occasional abrupt cooling events that might be caused by storms, eddies and/or waves. An idealised 1-D mixed-layer model is also used to underpin the driving mechanism of the observed mixed-layer features.

Access Condition and Agreement

Each deposit in UEA Digital Repository is protected by copyright and other intellectual property rights, and duplication or sale of all or part of any of the Data Collections is not permitted, except that material may be duplicated by you for your research use or for educational purposes in electronic or print form. You must obtain permission from the copyright holder, usually the author, for any other use. Exceptions only apply where a deposit may be explicitly provided under a stated licence, such as a Creative Commons licence or Open Government licence.

Electronic or print copies may not be offered, whether for sale or otherwise to anyone, unless explicitly stated under a Creative Commons or Open Government license. Unauthorised reproduction, editing or reformatting for resale purposes is explicitly prohibited (except where approved by the copyright holder themselves) and UEA reserves the right to take immediate ‘take down’ action on behalf of the copyright and/or rights holder if this Access condition of the UEA Digital Repository is breached. Any material in this database has been supplied on the understanding that it is copyright material and that no quotation from the material may be published without proper acknowledgement.

Contents

Abstract iii

List of Figures ix

Acknowledgements xxvii

1 INTRODUCTION 1

1.1 Antarctic Ice Sheet and sea level rise 1

1.2 Ice shelves in the Amundsen Sea 3

1.3 Oceanography in the Amundsen Sea 5

1.4 Aims and structure of this thesis 10

2 WINTER SEAL-BASED OBSERVATIONS REVEAL GLACIAL MELTWATER SURFACING IN THE SOUTHEASTERN AMUNDSEN SEA 13

2.1 Abstract 13

2.2 Introduction 14

2.3 Results 17

2.3.1 Meltwater distribution in summer 17

2.3.2 Unambiguous meltwater signal in winter 22

2.4 Discussion 26

2.5 Methods 31

2.5.1 Ship-based datasets 31

2.5.2 Seal-tag hydrographic dataset 33

2.5.3 Calculation of meltwater content from hydrographic data . 34

2.5.4 Quantifying the effect of wintertime surface cooling on derived meltwater values 36

2.5.5 Calculation of meltwater content from noble gas datasets . 37

2.6 Supplementary information 38

3 REVERSAL OF OCEAN GYRES NEAR ICE SHELVES IN THE AMUNDSEN SEA CAUSED BY THE INTERACTION OF SEA ICE AND WIND **47**

3.1 Abstract 47

3.2 Introduction 48

3.3 Observations of gyres in the west of Thwaites Ice Tongue 51

3.4 Model experimental design 58

3.4.1 Model set-up 58

3.4.2 Wind forcing 59

3.4.3 Sea ice coverage 60

3.5 Model results 63

3.5.1 Effect of wind stress on simulated gyres 63

3.5.2 Effect of sea ice on simulated gyres 64

3.6 Discussion 75

3.7 Conclusion 79

3.8 Data availability 80

3.9 Code availability 80

4 Intense upper-ocean cooling and salinification in the Amundsen Sea Polynya in austral autumn 81

4.1 Abstract 81

4.2 Introduction 82

4.3 Data and Method 85

4.3.1 Hydrographic observations from the southeastern Amundsen Sea Polynya 85

4.3.2 Estimation of the accumulated sea ice formation from observations 88

4.3.3 Sea ice condition in the Amundsen Sea 91

4.3.4 One-dimensional mixed layer model 93

4.3.5 Atmosphere reanalyses from ERA5 94

4.3.6 Definition of the mixed-layer depth for observation and model results 95

4.4 Observed intense cooling, salinification and mixed layer deepening . 96

4.5 The effect of sea ice blocking air-sea fluxes on the upper-ocean processes . . . 99
    4.5.1 The modelled upper-ocean processes forced with different $pSIC$ values . . . 99
    4.5.2 Effect of advection on the upper ocean processes . . . 103
4.6 Discussion . . . 105
4.7 Conclusions . . . 106

5 CONCLUSIONS 109

5.1 Summary . . . 109
    5.1.1 Background to the thesis . . . 109
    5.1.2 Meltwater pathways in winter in front of Pine Island Ice Shelf110
    5.1.3 The influence of wind-ice interactions on ocean gyres . . . 111
    5.1.4 Upper-ocean processes in the Amundsen Sea Polynya in austral autumn . . . 112
5.2 Future work . . . 113
5.3 Broader implications of this thesis . . . 116

Bibliography 120

List of Figures

1.1 **Changes in thickness and volume of Antarctic ice shelves between 1994–2012 (adapted from *Paolo et al.*, 2015).** Trends of thickness change in metres per decade are shown between -25 (thinning) to +10 (thickening), with circle size showing the percentage of thickness change. Thickness gaining are in blue and thickness loss are in red. Time series and polynomial fit of average volume change in cubic kilometres for the West (in red) and East (in blue) Antarctic ice shelves are shown in bottom left. Ice Shelves in the Amundsen Sea are marked in green box. The ice shelves of relevance to this thesis are highlighted by green arrows: PIN (Pine Island Ice Shelf), THW (Thwaites Ice Shelf) and DOT (Dotson Ice Shelf). 2

1.2 **Maps of the Amundsen Sea.** **a** Bathymetry (Rtopo; *Schaffer and Timmermann*, 2019) of the Amundsen Sea. Red arrows show the inferred mCDW intrusion in the Amundsen Sea (e.g. *Nakayama et al.*, 2013). **b** The Amundsen Sea with sea ice imagery on 04/03/2019 (Worldview true colour image from Terra/MODIS corrected reflectance). Inset shows where the study region is in Antarctica. 4

1.3 **Interaction of water masses with cold- and warm-water cavities (adapted from *Holland et al.*, 2020). a** Schematic for cold-cavity ice shelves, showing that Circumpolar Deep Water is blocked by the Antarctic Slope Front and cannot enter the continental shelf, nor the ice cavity. The ice cavity here is filled by cold Dense Shelf Water. **b** Schematic for warm-cavity ice shelves, showing that Circumpolar Deep Water enters the continental shelf and intrudes into the ice cavity to melt ice shelves. 6

1.4 Conservative temperature-absolute salinity diagram showing the typical values of the mCDW, Winter Water and Antarctic Surface Water, with potential density contours and surface freezing line overlaid. 6

1.5 Conservative temperature-absolute salinity diagram showing the typical values of the mCDW, Winter Water and Antarctic Surface Water, with potential density contours and surface freezing line overlaid. 8

2.1 **Map of the study region.** Positions of the seal-tag hydrographic profiles collected in winter (July–September) 2014 are indicated by solid dots and diamonds coloured by the conservative temperature, Θ, above freezing at 2 dbar (upper colour scale in red and blue). Positions of ship-based hydrographic profiles collected by conductivity-temperature-depth sensor in February 2014 are indicated by green diamonds aligned perpendicular and along to PIIS. Positions of profiles collected by vertical microstructure profiler in February 2014 are indicated by the thick black line along PIIS. Ship-based conductivity-temperature-depth sensor profiles overlay seal-tag profiles, vertical-microstructure-profiler profiles are at the bottom. Thick grey arrows show the schematic of PIB gyre (*Thurnherr et al.*, 2014). Rectangles enclose the profiles (diamonds) used for sections used in Figure 2.3, 2.4, 2.5, 2.6. Bathymetry from RTOPO (*Schaffer and Timmermann*, 2019) is shaded with grey colour scale on the lefthand side and ice photography (MODIS image from the 11 February, 2014) is shaded in blue with coastline in black. Inset map shows the location of southeastern Amundsen Sea. 15

2.2 **Meltwater content calculated from profiles near PIIS. a** The observed values (thin lines and dots) and the depth-mean values (thick lines) passed through a 10-m moving-average filter of meltwater content in Section 1 (pink rectangle in Figure 2.1), calculated from hydrographic data collected by seals in winter (blue), noble gas tracers in summer (black), ship-based hydrographic data collected by conductivity-temperature-depth sensor in summer (red) and vertical-microstructure profiler in summer (grey). Figure 2.8a,2.8b show the same plot as a, but for potential temperature and absolute salinity. **b** The conservative temperature – absolute salinity (Θ–S_A) diagram of wintertime hydrographic data. The background shading indicates the meltwater content. The grey dots represent all data collected by seals in our study region (Figure 2.1) in winter 2014. Thick lines overlaying the grey dots denote the depth-mean profiles in different sections (pink, green, blue and orange for Sections 1–4 in rectangles Figure 2.1). WW and mCDW end-points (see Methods section 2.5) are marked by dots near "WW" and "mCDW" texts. Isopycnals are indicated by solid black lines with labels. **c** same as **b**, but for the summertime ship-based hydrographic data collected by conductivity-temperature-depth sensor and vertical-microstructure profiler. 18

2.3 **Section 1, along the PIIS calving front, from southwest to northeast.** **a** Conservative temperature (Θ) above freezing (red–blue colour scale) and potential-density isopycnals (in kg m^{-3}) contours from Section 1 (pink rectangle in Figure 2.1) collected by seals in austral winter (Jul–Sep) 2014, with positions of profiles marked as triangles at the top of the panel. **b** Same as **a**, but for data from hydrographic profiles collected by ship-based vertical-microstructure profiler in February 2014. **c**, **d** same as **a** and **b**, but coloured by meltwater content (blue colour scale). Summertime meltwater signal in water layers above 27.42 isopycnal is partly associated with solar warming so is masked (*Biddle et al.*, 2017, *Jacobs et al.*, 2011, *Jenkins et al.*, 2018, *Nakayama et al.*, 2013) in **d**. Meltwater content calculated from noble gas tracers are indicated by dots overlaying the meltwater content calculated by ship-based hydrographic data in **d**. Figure 2.9a, 2.9b show the same plots as **a** and **b**, but coloured by absolute salinity. 20

2.4 **Section 2, from the southwestern end of the PIIS calving front towards the northwest.** **a** Conservative temperature (Θ) above freezing (red–blue colour scale) and potential-density isopycnals (in kg m^{-3}) contours from Section 2 (green rectangle in Figure 2.1) collected by seal in winter 2014, with positions of profiles marked as triangles at the top of the panel. **b** Same as **a**, but for data from ship-based hydrographic profiles collected by conductivity-temperature-depth sensor in February 2014. **c**, **d** same as **a** and **b**, but coloured by meltwater content (blue colour scale). Summertime meltwater signal in water layers above 27.42 isopycnal is partly associated with solar warming (*Biddle et al.*, 2017, *Jacobs et al.*, 2011, *Jenkins et al.*, 2018, *Nakayama et al.*, 2013) so is masked in **d**. Meltwater contents calculated from noble gas tracers are indicated by dots overlaying the meltwater content calculated by ship-based hydrographic data in **d**. Figure 2.10a, 2.10b show the same plots as **a** and **b**, but coloured by absolute salinity. 22

2.5 **Section 3, starts from the southeastern end of PIIS calving front and oriented following to the PIB gyre direction.** **a** Conservative temperature (Θ) above freezing (red–blue colour scale) and potential density isopycnals (in kg m^{-3}) contours from Section 3 (blue rectangle in Figure 2.1) collected by seals in winter 2014, with positions of the profiles marked as triangles at the top of the panel. **b** Same as **a**, but coloured by meltwater content (blue colour scale). Figure 2.11a, 2.11b show the same plots as **a** and **b**, but coloured by absolute salinity. 23

2.6 **Section 4, starts from the northwestern end of PIIS calving front and oriented opposite to the PIB gyre direction.** **a** Conservative temperature (Θ) above freezing (red–blue colour scale) and potential density isopycnals (in kg m^{-3}) contours from Section 4 (orange rectangle in Figure 2.1) collected by seals in winter 2014, with positions of the profiles marked as triangles at the top of the panel. **b** Same as **a**, but coloured by meltwater content (blue colour scale). Figure 2.12a, 2.12b show the same plots as **a** and **b**, but coloured by absolute salinity. 24

2.7 **Schematic representation of the meltwater-rich water pathways in winter and summer.** **a** Wintertime meltwater-rich water either spreads along pycnocline or rises through uniform water layers without undergoing intense lateral mixing. Wintertime meltwater-rich water rising to near surface melts sea ice and forms polynyas. **b** Summertime meltwater-rich water spreads along pycnocline as well. However, in contrast to wintertime meltwater-rich water, summertime rising meltwater-rich water penetrating through stratified water mixes with ambient water intensively and spreads widely. 28

2.8 **Potential density and absolute salinity (S_A) in front of PIIS.** **a** The observed values (thin lines and dots) and the depth-mean values (thick lines) passed through a 10-m moving-average filter of potential density in section 1 (pink rectangle in Figure 2.1) profiles collected by seals (blue) in winter 2014 and ship-based hydrographic data collected by conductivity-temperature-depth sensor (red) and vertical microstructure profiler (grey) in summer 2014. **b** same as **a** but for absolute salinity. 39

2.9 **Absolute salinity (S_A) of section 1, along the PIIS calving front, from southwest to northeast.** **a** Absolute salinity (S_A, yellow-blue colour scale)) and potential-density isopycnals (in kg m^{-3}) contours from section 1 (pink rectangle in Figure 2.1) collected by seals in austral winter (Jul–Sep) 2014, with positions of profiles marked as triangles at the top of the panel. **b** Same as **a**, but for data from hydrographic profiles collected by ship-based vertical microstructure profiler in February 2014. 40

2.10 **Absolute salinity (S_A) of section 2, from the southwestern end of the PIIS calving front towards the northwest.** **a** Absolute salinity (S_A, yellow-blue colour scale) and potential-density isopycnals (in kg m^{-3}) contours from section 2 (green rectangle in Figure 2.1) collected by seals in winter 2014, with positions of profiles marked as triangles at the top of the panel. **b** Same as **a**, but for data from ship-based hydrographic profiles collected by conductivity-temperature-depth sensor in February 2014. 41

2.11 **Absolute salinity (S_A) of section 3, starts from the southeastern end of PIIS calving front and oriented following to the PIB gyre direction.** Absolute salinity (S_A, yellow-blue colour scale) and potential-density isopycnals (in kg m^{-3}) contours from section 3 (blue rectangle in Figure 2.1) collected by seals in winter 2014, with positions of the profiles marked as triangles at the top of the panel. 41

2.12 **Absolute salinity (S_A) of section 4, starts from the northwestern end of PIIS calving front and oriented opposite to the PIB gyre direction.** Absolute salinity (S_A, yellow-blue colour scale) and potential-density isopycnals (in kg m^{-3}) contours from section 4 (orange rectangle in Figure 2.1) collected by seals in winter 2014, with positions of the profiles marked as triangles at the top of the panel. 42

2.13 **Map of the whole Amundsen Sea.** Dots indicating the positions of the seal-tag hydrographic profiles collected in winter (July to September) 2014 are coloured by the conservative temperature, Θ, above freezing at 2 dbar. The relatively warm water is identified along the coastline near PIB and the east of Dotson Ice Shelf. 42

2.14 **The months when seal-tag profiles were collected.** Dots indicating the positions of the seal-tag hydrographic profiles collected in each section in winter (July to September) 2014 are coloured by the months when data were collected. 43

2.15 **The Θ–S_A diagram zoomed in for mCDW in PIB.** The dots in blue and red indicate the data collected in winter and summer, respectively. The stars in blue and red indicate the mCDW endpoints in winter and summer separately. Inset shows the Θ–S_A, diagram of all data collected in PIB in 2014. 43

2.16 **The meltwater content of section 1, along the PIIS, from southwest to northeast.** The meltwater content is calculated using **a** wintertime endpoint values and **b** summertime endpoint values. The positions of the profiles are marked as triangles at the top of the panel. 44

2.17 **The meltwater content of section 2, from the southwestern end of the PIIS calving front towards the northwest.** The meltwater content is calculated using **a** wintertime endpoint values and **b** summertime endpoint values. The positions of the profiles are marked as triangles at the top of the panel. 44

2.18 **The meltwater content of section 3, starts from the southeastern end of PIIS calving front and oriented following to the PIB gyre direction.** The meltwater content is calculated using **a** wintertime endpoint values and **b** summertime endpoint values. The positions of the profiles are marked as triangles at the top of the panel. 45

2.19 **The meltwater content of section 4, starts from the northwestern end of PIIS calving front and oriented opposite to the PIB gyre direction.** The meltwater content is calculated using **a** wintertime endpoint values and **b** summertime endpoint values. The positions of the profiles are marked as triangles at the top of the panel. 45

2.20 **The Θ–S_A diagram of all data generated for Monte-Carlo simulation.** The black circles represent the two-hundred randomly-generated hydrographic measurements. The dots shaded by the meltwater content represent the 10,000 perturbed observations. WW and mCDW endpoints are marked by dots near "WW" and "mCDW" texts. Isopycnals are indicated by solid black lines with labels. 46

2.21 **Histograms showing the meltwater content bias induced by seal-tag data accuracy using Monte Carlo simulations.** Bias within one standard deviation are highlighted in orange. . . . 46

3.1 **Map of the southeastern Amundsen Sea.** Schematics of Pine Island Bay and Thwaites gyres are shown by thick blue arrows in front of Pine Island Ice Shelf and to the west of Thwaites Ice Tongue, respectively. The ice imagery is from Worldview Aqua/MODIS corrected reflectance (true colour) on 3 March 2019. The climatological 10 m wind velocity from 2009–2019 ERA5 reanalysis (*Hersbach et al.*, 2018) data (0.25° × 0.25° resolution; wind velocity data are interpolated to 0.25° × 0.125° resolution. Only every other arrow in the zonal direction is plotted for clarity) is denoted by orange arrows (see orange scale vectors). The blue box covers the region of Thwaites gyres that is used for Figure 3.2 and 3.4. The inset map shows our study region. 50

3.2 **Map of the Thwaites gyre region.** The blue arrows indicate the depth-averaged (30–430 m) current velocity from sADCP measurements (observations are averaged to 2 km × 2 km bins; see blue scale vectors). The red star indicates the gyre centre. The orange arrows indicate the 2009–2019 climatological wind from the ERA5 reanalysis (*Hersbach et al.*, 2018) (0.25° × 0.25° resolution; for clarity, velocity data are interpolated to 0.25° × 0.125° resolution; see orange scale vectors). The pink shaded dots show the full-depth-averaged meltwater content calculated from ship-based CTD data (see colour bar). 52

3.3 **Vertical structure of the Thwaites gyre.** **a** Tangential velocity of the Thwaites gyre with distance to the gyre centre (colours). All velocity profiles are horizontally averaged into 1 km radius bins (pale dots and lines) and then vertically averaged into 30m bins (thick lines). **b–d** Section plots of CTD measurements collected in the Thwaites gyre region, with distance to the gyre centre. Potential-density isopycnals (in kg m^{-3}) are denoted by grey contours. Positions of profiles are marked as triangles at the top of the panel. Below 650 m, the water column is occupied by modified Circumpolar Deep Water and is very stable so is not presented here. Conservative temperature above freezing is presented in **b**. Absolute salinity is presented in **c**. Meltwater content is presented in **d**. 54

3.4 **The ice conditions in the Thwaites gyre region.** The orange arrows denote daily-averaged wind speed from the ERA5 reanalysis (*Hersbach et al.*, 2018) (0.25°× 0.25°resolution; for clarity, velocity data are meridionally interpolated to 0.25°× 0.125°resolution). Dots are coloured by the wind stress curl calculated from the interpolated 0.25°× 0.125°resolution daily-averaged wind speed from the ERA5 reanalysis (*Hersbach et al.*, 2018). Thick blue arrows indicate the Thwaites gyre. Ice imagery is from **a** 25 January, **b** 1 February, **c** 13 February and **d** 23 February 2019, respectively, as stated above each panel. 57

3.5 **Model schematic.** Sea ice is indicated by the pale grey patch covering the northwestern half of the gyre domain. The orange arrow indicates the wind direction, perpendicular to the ice shelf front. 58

3.6 **Wind fields applied in this study. a** The wind field representing simplified climatological conditions in the southeastern Amundsen Sea. **b** Same as **a**, but with wind stress curl reduced by 50 %. **c** Same as **a**, but anticyclonic. **d** Same as **c**, but with wind stress curl reduced by 50 %. The arrows show wind stress (only every 13th arrow is plotted for clarity), with the scale on the southwestern corner of **c**. Shading shows wind stress curl, red for cyclonic and blue for anticyclonic. 60

3.7 **Ice coverages applied in this study. a** Comparison of all ice coverages. Angles are between the ice edges (thick coloured lines) and wind direction (thick orange line). The thick black line denotes the ice shelf front. **b–f** Schematics of sea ice coverage (shaded patches) and sea ice edge (thick coloured lines), with the same colour scheme as shown in **a**. Ice-free regions are shaded in pale blue. 62

3.8 **Simulated steady-state gyre streamfunction (Ψ) and current velocity, when sea ice is absent.** Shading indicates streamfunction while arrows indicate current velocity (only every eighth arrow is plotted for clarity). The wind forcing for each of panels **a–d** is shown in Figure 3.6a–d. 63

3.9 **Ocean surface stress curl (OSSC) and simulated gyre streamfunction (Ψ) for simulation with the WeakCyclonic wind field and the SeaIce$\frac{\pi}{4}$ and 0 % τ ice coverage. a** Shading indicates OSSC, and arrows indicate wind stress (only every 13th arrow is plotted for clarity). **b** Shading indicates simulated gyre Ψ, and arrows indicate current velocity (only every eighth arrow is plotted for clarity). 66

3.10 **Simulated maximum gyre streamfunction (Ψ) for cyclonic wind stress curl experiments.** Positive streamfunction values are cyclonic and negative values are anticyclonic. The line colours indicate the angle between the wind direction and the sea ice edge, as shown in Figure 3.7. Thick lines denote the simulations with strong wind stress curl (i.e. StrongCyclonic; Figure 3.6a) while thin lines denote the simulations with weak wind stress curl (i.e.WeakCyclonic; Figure 3.6b). Blue dots mark the turning points where the lines of simulated 9 have a discontinuity in gradient caused by the occurrence of dipoles or tripoles. Orange circles with texts mark the simulations shown in Figure 3.8, 3.9, 3.12, 3.13. 67

3.11 **Simulated maximum streamfunction (Ψ) changes with area-integrated OSSC over model domain.** There are 11 filled or open circles for each combination of different sizes and colours, indicating simulations with 11 percentages of wind stress transferred to the ocean. Positive streamfunctions are cyclonic (in the Southern Hemisphere) and negative streamfunctions are anticyclonic (in the Southern Hemisphere), while the opposite is true for OSSC. The colours of circles indicate the angle between sea ice edge and ice shelf front, as shown in Figure 3.7. Filled circles denote the simulations with cyclonic wind stress curl forcings while open circles denote the simulations with anticyclonic wind stress curl forcings. Large circles denote the simulations with strong wind stress curl forcings while small circles denote the simulations with weak wind stress curl forcings. Orange circles with texts mark the simulations shown in Figure 3.8, 3.9, 3.12, 3.13. 68

3.12 **a–d** Ocean surface stress (arrows; only every 13th arrow is plotted for clarity) and ocean surface stress curl (shading) for **a** 20 % τ; **b** 40 % τ; **c** 80 % $\tau$and **d** 200 % τ transferred to the ocean. Sea ice covers the northwestern half of the gyre domain (i.e. SeaIce$\frac{\pi}{4})andtheStrongCyclonicwindfieldisapplied.\mathbf{e} - -\mathbf{h}Simulatedstreamfunction(\Psi$; shading) and ocean current velocity (arrows; only every eighth arrow is plotted for clarity) resulting from the forcing in panels **a–d** respectively. 70

3.13 **Simulated gyre streamfunction (Ψ) when wind field is StrongCyclonic and sea ice completely blocks the wind (i.e. 0 % τ).** Arrows indicate the current speed (only every eighth arrow is plotted for clarity). Sea ice coverage information for panels **b–f** is shown in Figure 3.7b–f. 73

3.14 **Ocean surface stress curl (OSSC) and simulated gyre streamfunction (Ψ) for the simulation with the WeakCyclonic wind field.** Sea ice covers the whole model domain. Sea ice in the northeast has 200 % of τ transferred to the ocean (representing mobile ice) while sea ice in the southwest has 0 % of τ transferred to the ocean (representing fast ice). **a** The shading indicates the OSSC and the arrows indicate the wind stress. **b** The shading indicates the simulated gyre Ψ and the arrows indicate the current velocity. 75

4.1 **Map of the southeastern Amundsen Sea. a.** Ice photography (MODIS Terra on 14 March 2014) overlaid by locations of *EM959* seal tag profiles, coloured by year day of data collection. Profiles used to analyse temporal variation in Figs. 4 and 5 are indicated by solid dots encircled by the pink circle in the map, with their data-collection year day marked by pink rectangle in the colour bar. Dots with white edges indicate supplementary profiles collected from 1-13 May 2014 (from MEOP), with their data-collection year day marked by the orange rectangle in the colour bar. Black triangles with white edges indicate the profiles collected on 1 September 2014 (from MEOP). The curvy white-blue line is the schematic of the shape of Bear Ridge (modified from *Bett et al.* (2020)). The orange arrows show the averaged wind speed and direction during the *EM959* measuring period. The dashed white box marks the four ERA5 gridpoints we use to area-average the ERA5 reanalysis. **b.** Same as **a**, but for the bathymetry. Location of the study region in Antarctica is shown in the inset. 85

4.2 **The overview of calibration. a.** The salinity profiles from EM959 and CTD used for calibration. b. Temperature-salinity diagram showing the EM959 and CTD profiles used for calibration. 87

4.3 **Examples of the MODIS Terra visible images.** To best represent the sea ice condition in each month, we only use satellite images with minimum cloud covers. Pink circles indicate the *EM959* observational site. Dates when ice imageries were taken are shown in the bottom left of each panel. Scale of the map is shown in panel **i**. 92

4.4 Time series of ERA5 reanalyses used as atmospheric forcing and for air-sea fluxes estimation. **a.** Downward radiation. **b.** 2-m air temperature. **c.** 10-m wind stress. **d.** Precipitation **e.** Comparison among modelled top-200-m heat content forced by reanalysis at four different grids. 95

4.5 Conservative temperature - absolute salinity (Θ–S_A) diagrams, coloured by **a** depth and **b** year day of measurement. Filled dots show the recovered *EM959*, with year day indicated by the pink rectangle in the colour bar above panel **b**. Open circles show MEOP measurements from 01-13 May 2014, with year day indicated by the orange rectangle. Circles that are connected by grey lines are measurements from 01 Sep 2014; they are coloured in dark grey in panel **b**. Observations obtained in later dates overlay observations obtained in earlier dates. 97

4.6 **Time series of conservative temperature (Θ) above freezing, absolute salinity (S_A), and water stratification ($log_{10}N^2$).** This figure includes all measurement points collected by *EM959* during year day 51-106 (pink circle in the map in Figure 4.1 and the pink rectangle in the colour bar in Figure 4.1). The thick grey/black lines denote potential density that has been vertically bin-averaged into 5-m bins. The thin white lines with black edges are the bottom of the mixed layer. 99

4.7 **Examples of time series of modelled temperature and salinity.** **a** and **b** are for 0 %-*pSIC*, c and d are for 50 %-*pSIC*, and **e** and **f** are for 100 %-*pSIC*. Contours indicate potential density. The colour schemes are the same as in Figure 4.6. 101

4.8 **Comparison among observations and model results with different *pSIC*.** **a** Upper 200 m heat content. Model results are coloured by the colour scheme shown on the top of the panel. Observations collected by *EM959* are coloured in black, with the thin line for the heat content of each profile and the thick line for daily-averaged heat content. **b** Same as **a** but for sea ice formation. The line for heat-budget-derived ice formation is coloured in black and the line for salt-budget-derived ice formation is coloured in grey. **c** Same as **a** but for mixed-layer depths. 105

Acknowledgements

I can never speak out how grateful I am to my supervisors, Karen, Ben and Dave, for their support, emotionally and academically (it is in the intended order). They always guide me in the right direction in my research, with sincere (or insincere - it does not matter) encouragement and endless patience (which is extremely precious when it comes to my procrastination and stupid questions). Their passion for oceanography has been a beacon for me whenever I feel apathetic. Karen provided me with genuine mentoring, guiding me to discover my path in academia and demonstrating how to be a confident and passionate female researcher who is also curious, caring, supportive, and kind. She (and sometimes her dog too) is always there when I am stressed and anxious, (continually trying to persuade me to take holidays,) helping me to think through what I want and need. Ben is one of the most brilliant people I have ever met and always understands all my badly-phrased scientific questions immediately and answers my questions whenever I am in doubt. He is always patient to listen to my (*very*) long research plans, and always able to give me creative and constructive suggestions. Dave is the most chilled person in our meetings and always provides me with the most genuine comments. He cares about all the details of my research plans and is willing to read my (catastrophic) model code, spotting all tiny errors - that can easily be ignored by me for months and give me complex numbers for temperature (and a broken heart) in every model run.

Huge thanks also to my friends, officemates, and practically, shipmates, who have been keeping me sane during my PhD. I do not trust myself on naming everyone now but I do not think I can get through any challenge in my life without you. I am not a very social person but you have made me realise how important friendship is to me (in a random order as I go through my WhatsApp list): Joanna, Asmara, Callum, Sharon, Aleksandra, Peter, Li, Salar, Bastien, Barry, Daisy, Filip, Jiamin, Yanxin, Yuanxu, Tianyu, Imogen, Tiago and Laura. Thank you for being tolerant of our cooking skills as well, for which we can truly empathise with your pain.

Finally, thanks to my family. To my grandparents, for loving me, raising me, and naively believing me to be the smartest and kindest kid in the world since my year 0. They have taught me how to love and how to be happy. And to Shenjie, for his love, which I believe is the only thing in my life that I will never lose, for those (>3,000) cats we have petted (on streets in different countries), books we shared and countryside roads we cycled in Norfolk, for helping me with the dull code debugging and thesis formatting, and the most important, for being here with me always.

1

INTRODUCTION

Antarctica is losing ice rapidly in the current changing climate, which might dramatically affect global sea level and consequently human society (e.g. *Pattyn and Morlighem*, 2020). However, as a remote continent with a harsh environment, large portions of its area are highly under-sampled and the processes controlling the ice mass loss are poorly understood. The ice mass loss of Antarctica has been largely attributed to the oceanic melting of ice shelves, the floating portion of glaciers above the ocean (e.g. *Pritchard et al.*, 2012), emphasising the importance of the ocean to the future of ice sheets. Therefore, in this thesis, I study the oceanography in the Amundsen Sea, where some of the most rapidly melting glaciers in the world drain (Figure 1.1), with a focus on the interactions between the ocean, ice shelves and sea ice, and try to propose mechanisms explaining how these interactions have affected and will affect the Antarctic environment in the future.

1.1 Antarctic Ice Sheet and sea level rise

The ice mass loss of the Antarctic Ice Sheet is accelerating (e.g. *Pattyn and Morlighem*, 2020). This mass loss is highly uncertain and could cause more than 1 m of sea-level rise by 2100 (*Bamber et al.*, 2019, *DeConto and Pollard*, 2016, *Meredith et al.*, 2019). Antarctica has contributed about 0.3 mm per year to sea level between 1992 and 2017 (*Shepherd et al.*, 2018). Recent observations from remote sensing further reveal an increasing contribution of Antarctic Ice Sheet melting to sea level rise (*Rignot et al.*, 2019). Although different projections of the Antarctic sea level contribution show considerable discrepancies between them, reducing this uncertainty is very challenging (e.g. *Pattyn and Morlighem*, 2020), as it requires a more detailed monitoring of the Antarctic Ice Sheet and a better understanding of physical processes controlling the mass loss.

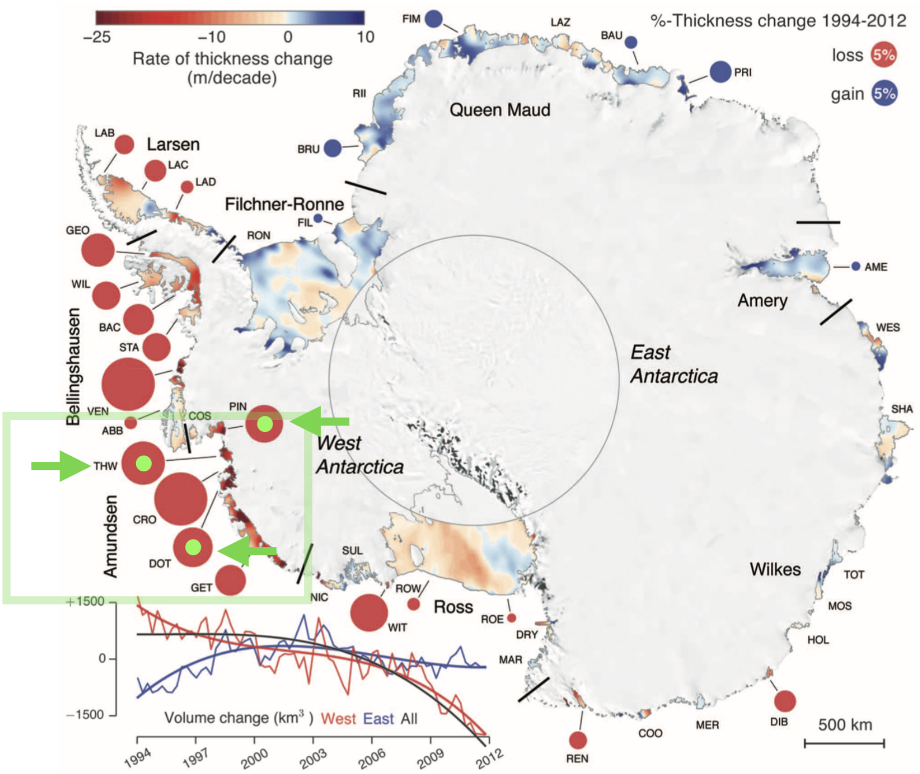
−25
−10
0
10
Rate of thickness change
(m/decade)
%-Thickness change 1994-2012
loss 5%
gain 5%
FIM
LAZ
BAU
PRI
RII
Queen Maud
LAB
Larsen
LAC
LAD
BRU
Filchner-Ronne
FIL
GEO
RON
WIL
AME
Amery
BAC
STA
WES
East
Antarctica
Bellingshausen
VEN
COS
PIN
SHA
ABB
West
Antarctica
THW
Amundsen
CRO
DOT
SUL
GET
NIC
ROW
Ross
ROE
WIT
DRY
MAR
Wilkes
TOT
MOS
HOL
+1500
0
−1500
Volume change (km³) West East All
1994
1997
2000
2003
2006
2009
2012
REN
COO
MER
DIB
500 km

Figure 1.1: **Changes in thickness and volume of Antarctic ice shelves between 1994–2012 (adapted from *Paolo et al.*, 2015).** Trends of thickness change in metres per decade are shown between -25 (thinning) to +10 (thickening), with circle size showing the percentage of thickness change. Thickness gaining are in blue and thickness loss are in red. Time series and polynomial fit of average volume change in cubic kilometres for the West (in red) and East (in blue) Antarctic ice shelves are shown in bottom left. Ice Shelves in the Amundsen Sea are marked in green box. The ice shelves of relevance to this thesis are highlighted by green arrows: PIN (Pine Island Ice Shelf), THW (Thwaites Ice Shelf) and DOT (Dotson Ice Shelf).

This ice mass loss results largely from the melting of the base of ice shelves (e.g. *Pritchard et al.*, 2012). Ice sheets flow from the interior on land to the ocean due to gravity via marine-terminating glaciers. The grounded ice and the floating ice shelves are then separated by the groundling line. Floating ice shelves are critical for the stability of ice sheets as they buttress the ice sheets and decelerate the flow of their grounded ice (e.g. *Scambos et al.*, 2014). Nonetheless, many ice shelves around Antarctica are thinning rapidly, reducing of the effect of buttressing and threatening the stability of the Antarctic Ice Sheet (Figure 1.1) (e.g. *Greene et al.*, 2022, *Paolo et al.*, 2015, *Pritchard et al.*, 2012).

1.2 Ice shelves in the Amundsen Sea

The ice mass loss of the Antarctic Ice Sheet has been concentrated on the West Antarctic Ice Sheet, especially near the Amundsen and Bellingshausen Seas (*Paolo et al.*, 2015, *Pritchard et al.*, 2012). The greatest ice shelf mass loss in Antarctica has been reported in those ice shelves terminating towards the Amundsen Sea, such as Pine Island Ice Shelf (PIIS), Thwaites Ice Shelf and Dotson Ice Shelf (*Paolo et al.*, 2015, *Rignot et al.*, 2019) (Figure 1.2). The accelerated ice flow, thinning and grounding line retreat of these ice shelves in the Amundsen Sea have dominated the mass loss of West Antarctic Ice Sheet (*Pattyn and Morlighem*, 2020).

Regardless of the importance of the ice shelves in the Amundsen Sea, the observations around ice shelves are very limited, because of the logistic constraints in this remote area (e.g. *Heywood et al.*, 2016). Compared with the Antarctic Peninsula, where many countries' research stations are located so that local surveys are carried annually and nearly year-round, the Amundsen Sea is sparsely observed as it is far away from any inhabited areas, with heavy sea ice covering the ocean nearly ten months a year. The lack of long-term observations of the glaciers, oceanography, atmosphere, biogeochemistry and bathymetry have substantially restricted our understanding of the current ice shelf melting processes, bringing uncertainties to model prediction of ice shelf futures (e.g. *Holland et al.*, 2020).

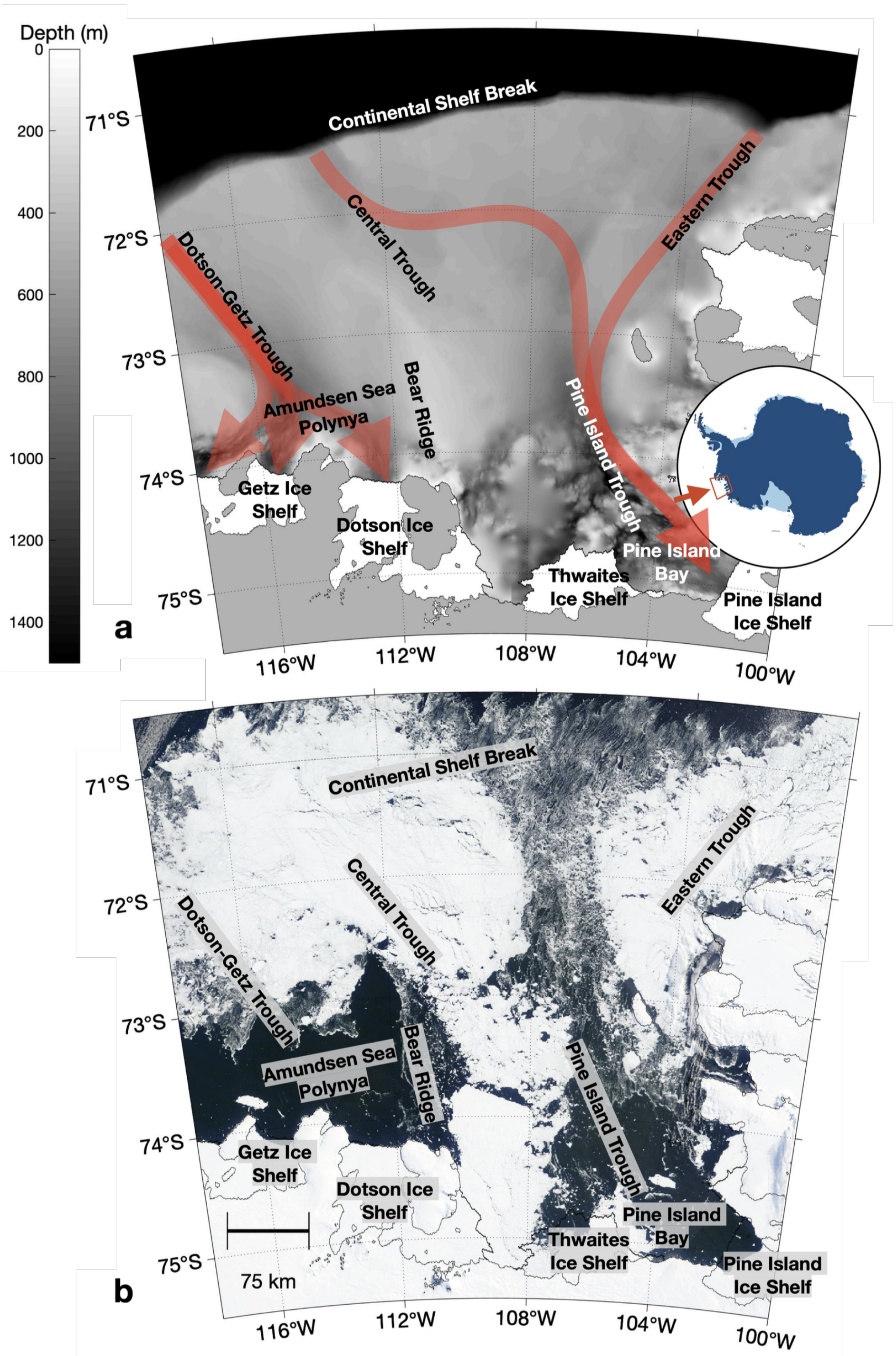
Depth (m)
0
200
400
600
800
1000
1200
1400
a
71°S
72°S
73°S
74°S
75°S
116°W
112°W
108°W
104°W
100°W
Continental Shelf Break
Central Trough
Eastern Trough
Dotson-Getz Trough
Amundsen Sea Polynya
Bear Ridge
Pine Island Trough
Getz Ice Shelf
Dotson Ice Shelf
Thwaites Ice Shelf
Pine Island Bay
Pine Island Ice Shelf
b
75 km

Figure 1.2: **Maps of the Amundsen Sea.** **a** Bathymetry (Rtopo; *Schaffer and Timmermann*, 2019) of the Amundsen Sea. Red arrows show the inferred mCDW intrusion in the Amundsen Sea (e.g. *Nakayama et al.*, 2013). **b** The Amundsen Sea with sea ice imagery on 04/03/2019 (Worldview true colour image from Terra/MODIS corrected reflectance). Inset shows where the study region is in Antarctica.

1.3 Oceanography in the Amundsen Sea

Two main processes that control the ice mass loss of ice shelves are iceberg calving and ice shelf melting (e.g. *Shepherd et al.*, 2018). The fast melting of ice shelves in the Amundsen Sea is due primarily to oceanic basal melting (e.g. *Pritchard et al.*, 2012). These ice shelves are so-called "warm-cavity ice shelves", with their ice-shelf cavities (i.e. ocean beneath the ice shelf) flooded by warm modified Circumpolar Deep Water (mCDW, about 3 °C above freezing; Figure 1.3) transporting heat to ice shelves via bathymetric troughs crossing the Amundsen Sea continental shelf (e.g. *Heywood et al.*, 2016, *Kim et al.*, 2021, *Mallett et al.*, 2018) (Figure 1.2a). Depending on factors such as the bathymetry at the continental shelf break and across the shelf, Ekman suction strength, and the glaciers' distance to the continental shelf break, some ice shelves are not in contact with mCDW. Instead of being flooded by mCDW, their cavities are filled by cold Dense Shelf Water that is at about the freezing point, so are called "cold-cavity ice shelves" (Figure 1.3). Cold-cavity ice shelves are often characterised by low basal melt rates and stable grounding lines, such as most ice shelves in the Weddell Sea and the Ross Sea, e.g. the Filchner-Ronne Ice Shelf and Ross Ice Shelf (e.g. *Hellmer et al.*, 2012, *Paolo et al.*, 2015). On the contrary, warm-cavity ice shelves have high basal melt rates and significantly retreating grounding lines, such as ice shelves in the Amundsen Sea and Bellingshausen Sea (e.g. *Heywood et al.*, 2016, *Holland et al.*, 2020). For warm cavity ice shelves, the local hydrography controls the amount of heat that can be transported into the ice cavity so is crucial to the ice shelf melting.

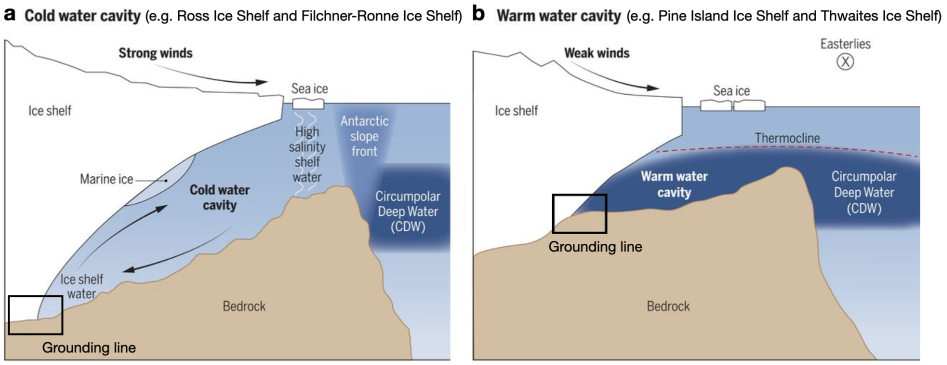
a Cold water cavity (e.g. Ross Ice Shelf and Filchner-Ronne Ice Shelf)
Strong winds
Sea ice
Ice shelf
High salinity shelf water
Antarctic slope front
Marine ice
Cold water cavity
Circumpolar Deep Water (CDW)
Ice shelf water
Bedrock
Grounding line
b Warm water cavity (e.g. Pine Island Ice Shelf and Thwaites Ice Shelf)
Weak winds
Easterlies
Sea ice
Ice shelf
Thermocline
Warm water cavity
Circumpolar Deep Water (CDW)
Grounding line
Bedrock

Figure 1.3: **Interaction of water masses with cold- and warm-water cavities (adapted from *Holland et al.*, 2020). a** Schematic for cold-cavity ice shelves, showing that Circumpolar Deep Water is blocked by the Antarctic Slope Front and cannot enter the continental shelf, nor the ice cavity. The ice cavity here is filled by cold Dense Shelf Water. **b** Schematic for warm-cavity ice shelves, showing that Circumpolar Deep Water enters the continental shelf and intrudes into the ice cavity to melt ice shelves.

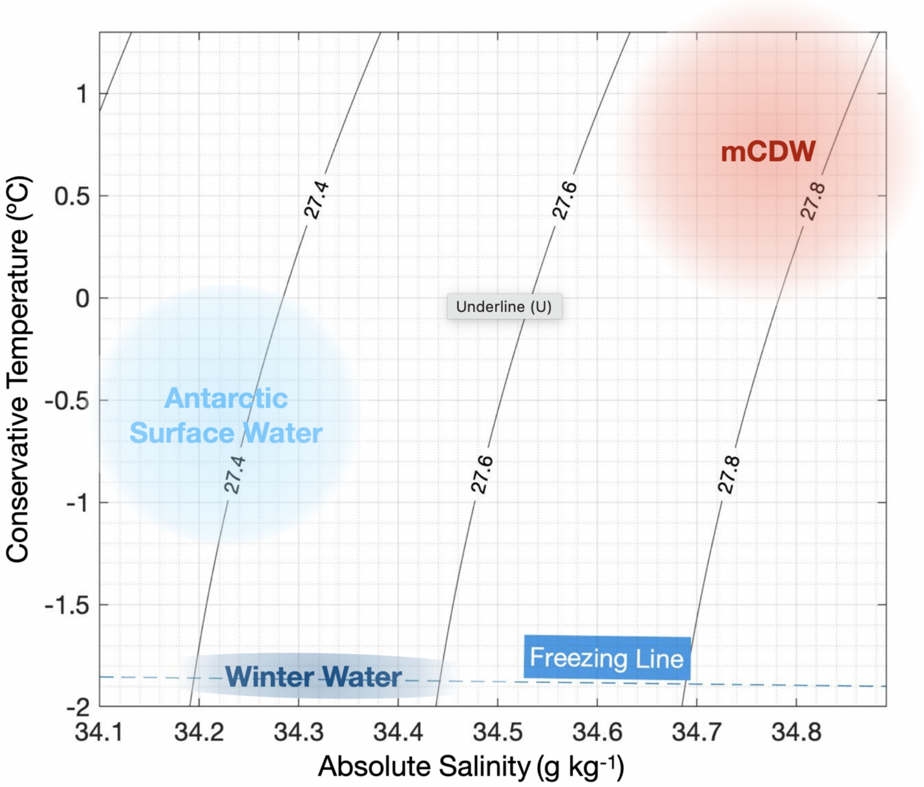

Figure 1.4: Conservative temperature-absolute salinity diagram showing the typical values of the mCDW, Winter Water and Antarctic Surface Water, with potential density contours and surface freezing line overlaid.

The Amundsen Sea generally consists of three main water masses, including mCDW, Winter Water and Antarctic Surface Water (Figure 1.4). mCDW is a mixture of the local water masses in the Amundsen Sea continental shelf, and the Circumpolar Deep Water found north of the continental shelf break that circulates within Antarctic Circumpolar Current. Circumpolar Deep Water has a core temperature of about 2 °C, and when it enters the Amundsen Sea via crosscutting bathymetric troughs, it transforms into mCDW (e.g. *Jacobs et al.*, 2012), the warmest water mass in the Amundsen Sea. mCDW fills the bottom layer (typically > 450 m) in most of the Amundsen Sea and is characterised by a warm conservative temperature, high absolute salinity and high potential density (marked in red in Figure 1.4). Winter Water is the remnant of the winter mixed layer formed during winter by intense surface cooling and wind stirring so is the coldest water mass in the Amundsen Sea. It has a temperature near the freezing point and is fresher and slightly lighter than mCDW so that it lies above mCDW (marked in dark blue in Figure 1.4). In summer, WW becomes capped, by the solar heating and the sea ice melt, which forms Antarctic Surface Water. Antarctic Surface Water is therefore fresher and warmer than Winter Water (marked in light blue in Figure 1.4), though its hydrographic characteristics vary depending on many factors such as the intensity of solar warming and sea ice formation and melt rates. In addition to these three water masses, the ocean receives glacial meltwater as the direct consequence of glacier melting. The surface runoff (i.e. glacial meltwater formed by surface melt) stays at the sea surface because it is very fresh and therefore light. As shown in 1.5, at the base of glacier, where it comes into contact with relatively warm mCDW, melting occurs. The resultant composition of water discharged from the ice cavity is the glacial modified water, which is a mixture of mCDW and glacial meltwater. Glacial modified water exhibits a combination of temperature and salinity characteristics dependent on the proportions of mCDW and glacial meltwater in the final composition. Due to the dynamic processes of melting and mixing within the ice cavity, the fractions of mCDW and glacial meltwater undergo spatial and temporal changes. Consequently, the density of glacial modified water varies, leading it to flow towards levels where it reaches its neutral density. Hence, glacial basal meltwater can disperse across a wide range of depths above the mCDW, contingent upon the amount of glacial meltwater entrained within the glacial modified water. Meltwater will affect the water stratification and the associated flow pattern.

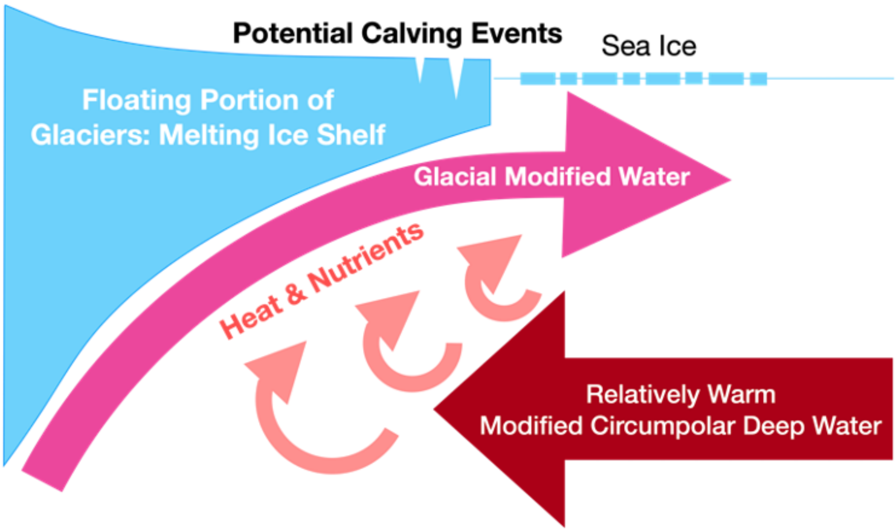
Potential Calving Events
Sea Ice
Floating Portion of Glaciers: Melting Ice Shelf
Glacial Modified Water
Heat & Nutrients
Relatively Warm Modified Circumpolar Deep Water

Figure 1.5: Conservative temperature-absolute salinity diagram showing the typical values of the mCDW, Winter Water and Antarctic Surface Water, with potential density contours and surface freezing line overlaid.

Although most Amundsen Sea waters are a combination of these three water masses and meltwater, the hydrographic properties in front of different ice shelves vary dramatically. The mCDW in front of Pine Island and Thwaites Ice Shelves is about 1 °C (e.g. *Yoon et al.*, 2022) while the mCDW in front of Dotson Ice Shelf is about 0.6 °C (e.g. *Kim et al.*, 2016, *Randall-Goodwin et al.*, 2015). This spatial difference of hydrography in front of different ice shelves has been attributed to many factors such as the location of winter polynyas (i.e. open ocean surrounded by sea ice; e.g. *St-Laurent et al.*, 2015), local wind field (e.g. *Steiger et al.*, 2021), distance from ice shelves to the continental shelf break (e.g. *Assmann et al.*, 2013) and bathymetric troughs that steer mCDW (e.g. *Jenkins et al.*, 2010). mCDW flows towards ice shelves in the southeastern Amundsen Sea via Pine Island Trough, Dotson Trough and Central Trough (Figure 1.2). Pine Island Trough has a deeper bathymetry, and consequently a higher mCDW temperature.

Most observations in the Amundsen Sea are obtained during summer, while the oceanography in non-summer seasons is heavily under-sampled. Traditionally, the two platforms used in the Amundsen Sea during winter are moorings and satellites. Although both platforms give us a great amount of observations and a chance to have a glance at wintertime oceanography, their capabilities are limited by many factors. Moorings require regular cruises to deploy and recover them, and they only provide observations at fixed locations at several fixed levels below 200 m, since they are vulnerable to icebergs so rarely have sensors installed in the top 200 m. Satellite measurements cannot provide hydrographic observations in depth and are often affected by perturbations like frequent storms and cloud changes.

Seal tags are conductivity-temperature-depth (CTD) satellite relay data loggers attached on seals (e.g. *Roquet et al.*, 2013). Deployments of seal tags have remarkably filled the sparseness of the non-summer observations in the Amundsen Sea (e.g. *Boehme et al.*, 2021, *Mallett et al.*, 2018), giving us new tools to investigate the oceanography during non-summer seasons. Data from these seal-borne sensors will be explored in this thesis.

The Amundsen Sea continental shelf sea surface is usually covered by a layer of sea ice, whose shape and type change seasonally and inter-annually. Although the sea ice season duration has decreased in recent decades, it still reaches about 300 days per year (*Stammerjohn et al.*, 2015). Sea ice can modify the air-sea heat exchange and momentum exchange (e.g. *Meneghello et al.*, 2018, *Pellichero et al.*, 2017) so may further change the water properties and flow pattern in the Amundsen Sea. Sea ice condition changes can be partially explained by winds, but the interactions between ice and ocean are largely unknown (*Stammerjohn et al.*, 2015), due to the limited hydrographic measurements below ice. Ice-tethered profilers have shown their capability to obtain observations below ice in the Amundsen Sea (e.g. *Ackley et al.*, 2015), and long-term observations below ice in other polar oceans (e.g. *Porter et al.*, 2018). However, like moorings, ice-tethered-profilers often require multiple cruises and only have sensors at fixed depths. In February 2019, scientists on board RV *Nathaniel B. Palmer* in the Amundsen Sea witnessed the breaking of fast ice west of the Thwaites Ice Tongue, and obtained hydrographic measurements in the habitually ice-covered area. These measurements enabled the work described in this thesis to look into the flow pattern in ice-covered regions.

1.4 Aims and structure of this thesis

In this thesis, I focus on the oceanography in front of ice shelves, where interactions between ocean, ice shelf and sea ice play a crucial role in ice shelf melting. I use state-of-art observations, combined with idealised models, to propose new mechanisms that control the local physical oceanic processes.

Among the four water masses in the Amundsen Sea, basal meltwater draws my attention first. When mCDW melts ice shelves, the meltwater enriched mCDW contains heat and nutrients, changing the water properties in locations it flows to, melting the sea ice and boosting the local productivity. Meltwater is usually identified by its hydrographic signature (i.e. temperature and salinity) and its pathway has been detected in many sites in the Amundsen Sea in summer (e.g. *Biddle et al.*, 2017, *Naveira Garabato et al.*, 2017); however, its wintertime pathway has not yet been investigated. My co-authors and I reveal the wintertime meltwater distribution using a set of full-depth hydrographic measurements and attribute the seasonal meltwater distribution we find to the seasonal upper-ocean stratification. Those results are presented in Chapter 2, *Winter seal-based observations reveal glacial meltwater surfacing in the southeastern Amundsen Sea.* This chapter was published as a paper in *Communications Earth & Environment* (*Zheng et al.*, 2021).

Ocean velocity measurements obtained onboard RV *Nathaniel B. Palmer* in

2019 reveal a 25-km-radius gyre in a habitually ice-covered region, rotating anticyclonically (i.e. anti-clockwise in the Southern Hemisphere), regardless of the climatologically cyclonic wind forcing in this region. Gyres modulate the heat transported towards ice shelves, which motivates my further study. I compare the sea ice conditions in the gyre region with another cyclonic gyre, influenced by a wind field with the same wind stress curl direction, and hypothesise that the presence of ice may change the gyre direction. We use an idealised barotropic model to support our hypothesis, and summarise the results into Chapter 3, *Reversal of ocean gyres near ice shelves in the Amundsen Sea caused by the interaction of sea ice and wind.* This chapter was published as a paper in *The Cryosphere* (*Zheng et al.*, 2022).

The Amundsen Sea Polynya is the most productive polynya in coastal Antarctica (*Arrigo and van Dijken*, 2003) but is yet poorly sampled with its formation processes largely unknown. My co-authors and I present full-depth hydrographic observations obtained at the southeastern corner of the Amundsen Sea Polynya in autumn to show the upper-ocean evolution in this sea ice/polynya formation season. I also use an idealised 1-D model to show that sea ice regulation of heat exchange may play a role in upper-ocean salinification, cooling and mixed-layer deepening. This leads to the third results chapter, Chapter 4, *Intense upper-ocean cooling and salinification in the Amundsen Sea Polynya in austral autumn.* This chapter is presented as a draft paper intended for submission shortly.

The main results and implications of this thesis, with some suggestions for future work, are summarised in Chapter 5, *Conclusions.*

2

WINTER SEAL-BASED OBSERVATIONS REVEAL GLACIAL MELTWATER SURFACING IN THE SOUTHEASTERN AMUNDSEN SEA

2.1 Abstract

Determining the injection of glacial meltwater into polar oceans is crucial for quantifying the climate system response to ice sheet mass loss. However, meltwater is poorly observed and its pathways poorly known, especially in winter. Here we present winter meltwater distribution near Pine Island Glacier using data collected by tagged seals, revealing a highly variable meltwater distribution with two meltwater-rich layers in the upper 250 m and at around 450 m, connected by scattered meltwater-rich columns. We show that the hydrographic signature of meltwater is clearest in winter, when its presence can be unambiguously mapped. We argue that the buoyant meltwater provides near-surface heat that helps to maintain polynyas close to ice shelves. The meltwater feedback onto polynyas and air-sea heat fluxes demonstrates that although the processes determining the distribution of meltwater are small-scale, they are important to represent in Earth system models.

2.2 Introduction

Floating ice shelves buttress the Antarctic Ice Sheet and decelerate the flow of its grounded ice. However, many ice shelves around Antarctica are thinning rapidly due primarily to basal melting (e.g. *Pritchard et al.*, 2012). The strongest melt has been reported in West Antarctic ice shelves such as the Pine Island Ice Shelf (PIIS) and Thwaites Ice Shelf (e.g. *Paolo et al.*, 2015, *Rignot et al.*, 2019) where the deep (below about 450 m) intrusion of warm modified Circumpolar Deep Water (mCDW) transports heat southward via bathymetric troughs crossing the continental shelf (e.g. *Heywood et al.*, 2016). The warm mCDW (about 3 °C above freezing) then enters the ice-shelf cavity (i.e. ocean beneath the ice shelf), circulates beneath the ice shelf providing heat for basal melting, and forms a relatively fresh meltwater-rich water mass that is colder than mCDW but warmer than the surrounding Winter Water (WW; e.g. *Heywood et al.*, 2016, *Jacobs et al.*, 2011, *Jenkins et al.*, 2018).

The fate and impact of the meltwater-rich water depends greatly on the depth at which it achieves neutral buoyancy and leaves the region flowing along density surfaces. If the relatively fresh meltwater-rich water rises, it could offset the brine rejected by sea ice formation and reduce occurrences of deep convection and bottom-water formation (e.g. *Mackie et al.*, 2020, *Silvano et al.*, 2018). The relatively warm meltwater-rich water may also melt the sea ice in front of the ice shelf (e.g. *Bindschadler et al.*, 2011, *Le Brocq et al.*, 2013, *Mankoff et al.*, 2012). The resulting polynya would allow air-sea heat exchange and feedback onto ice-shelf basal melt by influencing the upper-ocean heat content (e.g. *Fogwill et al.*, 2015, *Mackie et al.*, 2020, *Pritchard et al.*, 2012). The outflow of meltwater may boost the overturning circulation resulting in an enhanced heat flux into the ice cavity (e.g. *Jourdain et al.*, 2017, *Nakayama et al.*, 2014, *Naveira Garabato et al.*, 2017, *Webber et al.*, 2019). The meltwater-rich water is also a key supply of iron for continental shelf seas (e.g. *St-Laurent et al.*, 2019). Therefore, although the volume of meltwater produced is small in comparison with the volumes of

Antarctic shelf seas, it is believed to exert a disproportionate influence on regional and circumpolar circulation and climate.

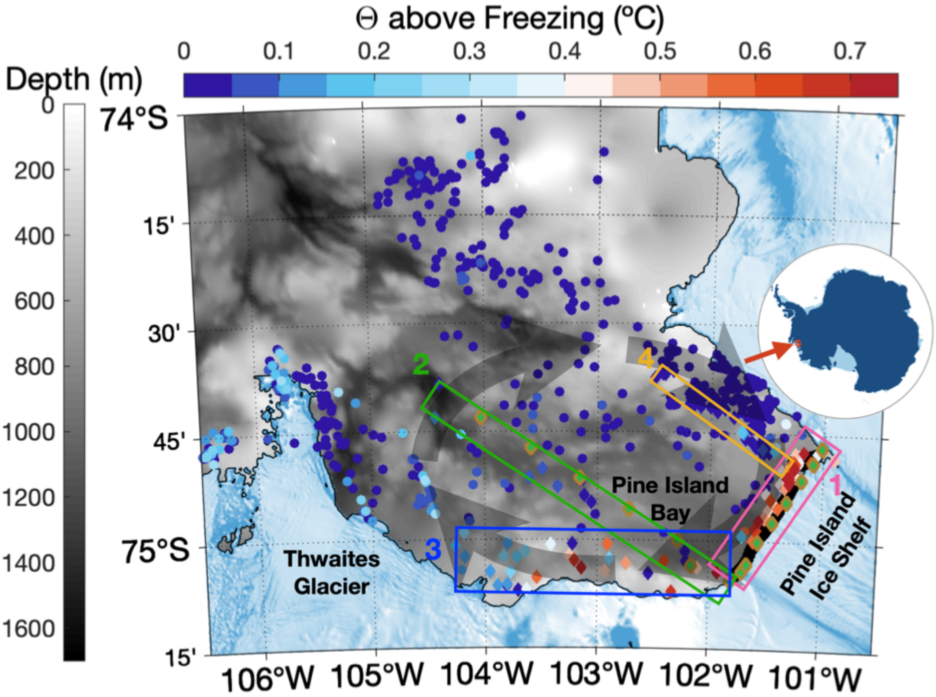

Figure 2.1: **Map of the study region.** Positions of the seal-tag hydrographic profiles collected in winter (July–September) 2014 are indicated by solid dots and diamonds coloured by the conservative temperature, Θ, above freezing at 2 dbar (upper colour scale in red and blue). Positions of ship-based hydrographic profiles collected by conductivity-temperature-depth sensor in February 2014 are indicated by green diamonds aligned perpendicular and along to PIIS. Positions of profiles collected by vertical microstructure profiler in February 2014 are indicated by the thick black line along PIIS. Ship-based conductivity-temperature-depth sensor profiles overlay seal-tag profiles, vertical-microstructure-profiler profiles are at the bottom. Thick grey arrows show the schematic of PIB gyre (*Thurnherr et al.*, 2014). Rectangles enclose the profiles (diamonds) used for sections used in Figure 2.3, 2.4, 2.5, 2.6. Bathymetry from RTOPO (*Schaffer and Timmermann*, 2019) is shaded with grey colour scale on the lefthand side and ice photography (MODIS image from the 11 February, 2014) is shaded in blue with coastline in black. Inset map shows the location of southeastern Amundsen Sea.

PIIS is one of the most rapidly melting ice shelves (e.g. *Paolo et al.*, 2015, *Rignot et al.*, 2019). Although meltwater has been identified in front of PIIS (e.g. *Biddle et al.*, 2017, 2019, *Heywood et al.*, 2016, *Jacobs et al.*, 2011, *Jenkins et al.*, 2018, *Nakayama et al.*, 2013, *Naveira Garabato et al.*, 2017), its spatial pattern is complex and poorly observed and understood. Meltwater is usually detected by its signature in hydrographic (i.e. temperature and salinity) observations. Nonetheless, as solar warming in the near-surface layer (upper 200 m) can be mistaken for the signal of relatively warm meltwater exiting the ice-shelf cavity, the apparent near-surface meltwater-rich layer deduced from austral summer hydrographic observations is usually thought to be an artefact of solar warming and is therefore neglected (e.g. *Biddle et al.*, 2017, *Jacobs et al.*, 2011, *Jenkins et al.*, 2018, *Nakayama et al.*, 2013). Thus, to date, the primary scientific focus in front of warm-cavity ice shelves has been on the deep meltwater layer with a maximum concentration at around 200–400 m (e.g. *Biddle et al.*, 2017, *Jacobs et al.*, 2011, *Nakayama et al.*, 2013, *Naveira Garabato et al.*, 2017). However, in austral winter, when there can be no effect of solar radiation on the calculation of meltwater, the vertical meltwater distribution has hitherto been completely unknown due to the lack of available observations. *Naveira Garabato et al.* (2017) also describes that when the meltwater injects into the stratified water columns in front of PIIS in summer, it stretches the water column and tilts the isopycnals. The pressure gradients caused by the tilted isopycnals induce a localised geostrophic flow. This localised flow is featured by an anticyclonic relative vorticity that surpasses the magnitude of the local planetary vorticity, resulting in the centrifugal instability. However, prior to this study, no wintertime observations have been available to reveal the fate of meltwater injection in winter when the upper ocean in front of PIIS is homogenous. The cyclonic Pine Island Bay (PIB) gyre is well defined from the sea surface to about 700-m depth in front of PIIS in both observational data (*Heywood et al.*, 2016, *Thurnherr et al.*, 2014) and model outputs (*Schodlok et al.*, 2012), but the sparse observations have not yet clearly revealed the influence of the PIB gyre on the meltwater distribution. Introducing new datasets and approaches in this region is therefore important for ocean, cryosphere and climate research.

In this study we turn to newly available Antarctic winter observations (July–September 2014) to determine the distribution of near-surface meltwater exiting from beneath PIIS in winter. In winter, heat loss to the atmosphere and wind mixing lead to a mixed layer of cold WW with no summertime warm water remaining near the sea surface. The meltwater-rich water is much warmer (up to about 1 °C above freezing) than other upper-ocean water masses which have temperatures near the freezing point (about -1.9 °C) in winter. In this way we unambiguously distinguish ice-shelf basal meltwater from ambient water masses. Here we present a set of 625 novel wintertime full-depth profiles of salinity and temperature collected by sensors attached onto three seals (see Methods section 2.5), yielding four sections across PIB (Figure 2.1). A meltwater signal is apparent in all sections in both winter (Figure 2.2b, 2.2c, 2.3c, 2.4c, 2.5b, 2.6b) and summer (Figure 2.3d, 2.4d). Our winter observations reveal clear signals of meltwater both at depth and near the surface, connected by distinct meltwater-rich columns, while much of the WW layer remains meltwater-poor. This spatial heterogeneity is in contrast to the relatively high and horizontally-uniform upper-ocean meltwater content indicated by summer ship-based hydrography and previously-unpublished near-surface noble gas measurements. We argue that in winter, compared with the cold and dense ambient water, the meltwater-rich water has sufficient buoyancy to rise to near surface without undergoing intense lateral mixing. The winter processes revealed by our study are likely important for bringing nutrients to the near-surface layer prior to the spring bloom, and for bringing heat to the surface to prevent sea ice from forming and thus maintaining the polynyas in front of the ice shelves.

2.3 Results

2.3.1 Meltwater distribution in summer

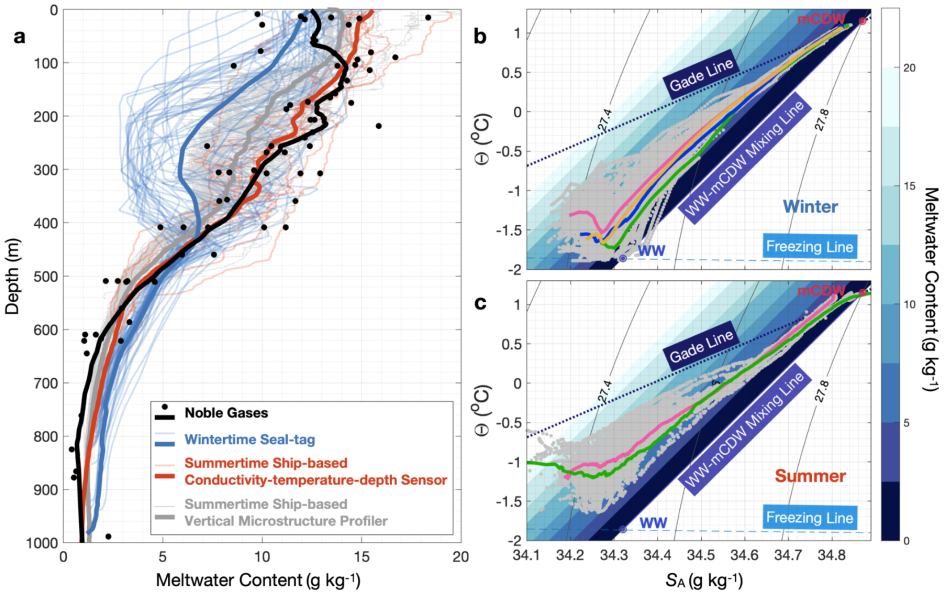

Figure 2.2: **Meltwater content calculated from profiles near PIIS. a** The observed values (thin lines and dots) and the depth-mean values (thick lines) passed through a 10-m moving-average filter of meltwater content in Section 1 (pink rectangle in Figure 2.1), calculated from hydrographic data collected by seals in winter (blue), noble gas tracers in summer (black), ship-based hydrographic data collected by conductivity-temperature-depth sensor in summer (red) and vertical-microstructure profiler in summer (grey). Figure 2.8a,2.8b show the same plot as a, but for potential temperature and absolute salinity. **b** The conservative temperature – absolute salinity (Θ–S_A) diagram of wintertime hydrographic data. The background shading indicates the meltwater content. The grey dots represent all data collected by seals in our study region (Figure 2.1) in winter 2014. Thick lines overlaying the grey dots denote the depth-mean profiles in different sections (pink, green, blue and orange for Sections 1–4 in rectangles Figure 2.1). WW and mCDW end-points (see Methods section 2.5) are marked by dots near “WW” and “mCDW” texts. Isopycnals are indicated by solid black lines with labels. **c** same as **b**, but for the summertime ship-based hydrographic data collected by conductivity-temperature-depth sensor and vertical-microstructure profiler.

Meltwater content values calculated from ship-based hydrographic and noble gas data are fairly consistent below about 150 m but significantly different above 150 m (Figure 2.2a), where higher values from hydrographic data might be partly an artefact related to solar warming (e.g. *Biddle et al.*, 2017, *Jacobs et al.*, 2011, *Jenkins et al.*, 2018, *Nakayama et al.*, 2013). Noble gas tracers are considered a more reliable indicator of meltwater as no known processes other than glacial ice melting can generate the noble gas signal (e.g. *Beaird et al.*, 2015, *Hohmann et al.*, 2002, *Loose et al.*, 2014). Hence, the meltwater content calculated from noble gas tracers is used to constrain our meltwater content calculated solely from hydrographic tracers (i.e. temperature and salinity, see Methods). Although noble gas can be lost to the atmosphere, which can slightly decrease the value of the calculated meltwater content, this uncertainty is small compared with the uncertainties caused by air-sea interaction on the hydrographic tracers (e.g. *Loose et al.*, 2009, *Stanley et al.*, 2009). Thus, noble gas provides information of the near-surface meltwater distribution complementary to what we calculated from hydrographic measurements. We therefore mask the meltwater content located above the 27.42 isopycnal (approximately the upper 200 m) that is calculated from hydrographic data in summer in Figure 2.3d, 2.4d. In the following text, for the meltwater content in the masked region (Figure 2.3d, 2.4d), we only discuss results calculated from noble gas data.

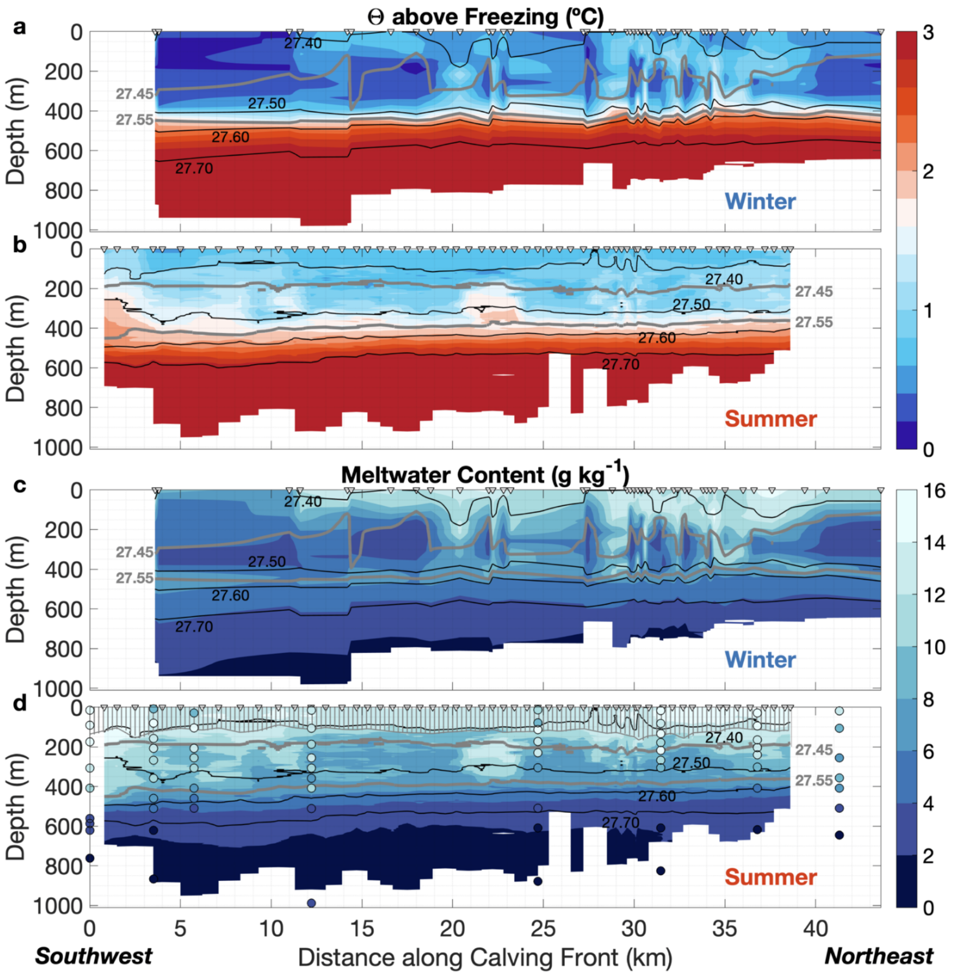

Figure 2.3: **Section 1, along the PIIS calving front, from southwest to northeast.** **a** Conservative temperature (Θ) above freezing (red–blue colour scale) and potential-density isopycnals (in kg m^{-3}) contours from Section 1 (pink rectangle in Figure 2.1) collected by seals in austral winter (Jul–Sep) 2014, with positions of profiles marked as triangles at the top of the panel. **b** Same as **a**, but for data from hydrographic profiles collected by ship-based vertical-microstructure profiler in February 2014. **c**, **d** same as **a** and **b**, but coloured by meltwater content (blue colour scale). Summertime meltwater signal in water layers above 27.42 isopycnal is partly associated with solar warming so is masked (*Biddle et al.*, 2017, *Jacobs et al.*, 2011, *Jenkins et al.*, 2018, *Nakayama et al.*, 2013) in **d**. Meltwater content calculated from noble gas tracers are indicated by dots overlaying the meltwater content calculated by ship-based hydrographic data in **d**. Figure 2.9a, 2.9b show the same plots as **a** and **b**, but coloured by absolute salinity.

The hydrographic data reveal a strongly stratified water column above the 27.55 isopycnal (at about 450 m in summer, Figs. 3b, 4b). This stratification results from summertime solar warming, sea ice meltwater and surface runoff. The meltwater-rich water exported from ice cavity with density greater than the 27.55 kg m^{-3} stays below the 27.55 isopycnal while the rest keeps ascending until it reaches neutral buoyancy. Summertime hydrographic and noble gas data in front of PIIS (dots and lines in black and red, Figure 2.2a) reveal the meltwater content to gradually increase from about 500 m to about 100 m.

The summertime meltwater content above 27.55 isopycnal is always greater than 5 g kg^{-1}, which makes the horizontal variability of meltwater content relatively small in summer (Figure 2.2a, 2.2c, 2.3d, 2.4d). Note that there is no indication of meltwater-poor layers nor columns above 400 m in summer from either the noble gas or hydrographic data in front of PIIS (Figure 2.2a, 2.2c, 2.3d, 2.4d).

We identify a clear isopycnal dome centred at about 32 km from PIIS (Figure 2.4b) that may be associated with the cyclonic PIB gyre (*Thurnherr et al.*, 2014). The meltwater content is highest in front of PIIS and decreases with distance from PIIS until the centre of the PIB gyre, where it reaches its minimum value (Figure 2.4d). The meltwater content then increases with distance from the gyre centre to the northwestern edge of the PIB gyre along Section 2 (Figure 2.4d). This suggests that the PIB gyre is transporting meltwater from PIIS cyclonically to the outer PIB.

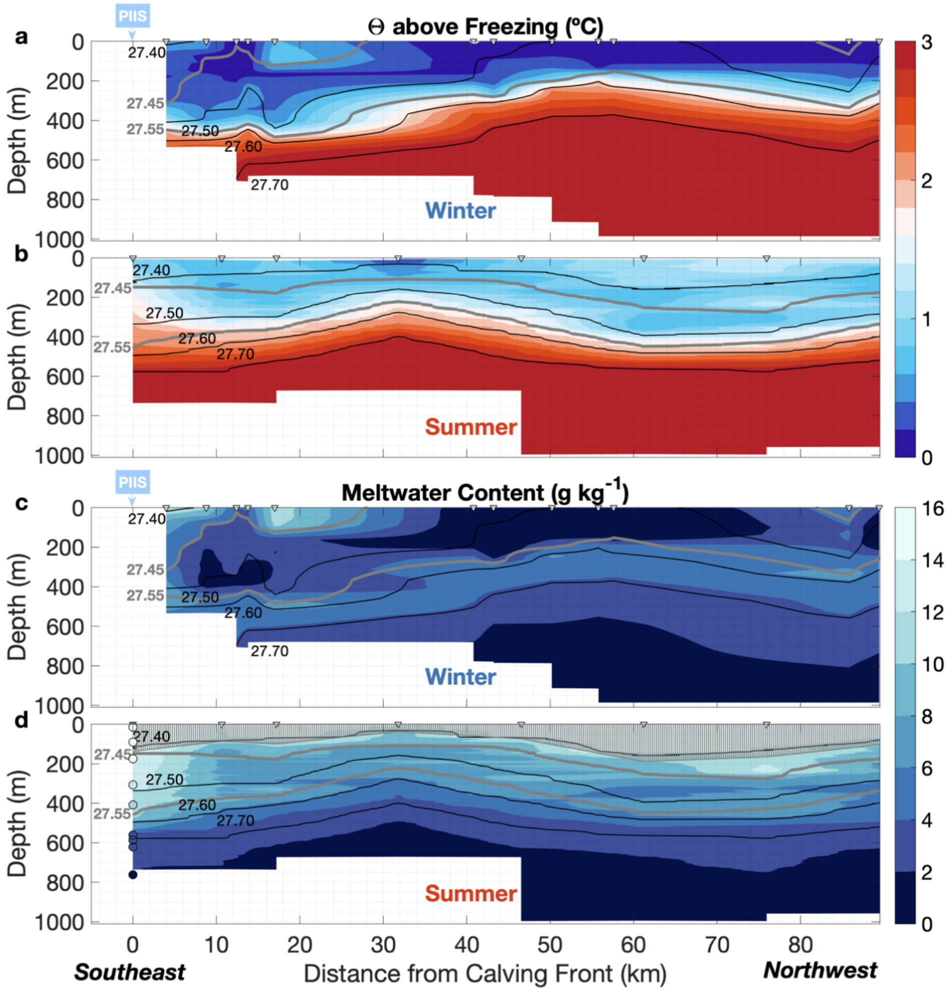

Figure 2.4: **Section 2, from the southwestern end of the PIIS calving front towards the northwest.** **a** Conservative temperature (Θ) above freezing (red–blue colour scale) and potential-density isopycnals (in kg m^{-3}) contours from Section 2 (green rectangle in Figure 2.1) collected by seal in winter 2014, with positions of profiles marked as triangles at the top of the panel. **b** Same as **a**, but for data from ship-based hydrographic profiles collected by conductivity-temperature-depth sensor in February 2014. **c**, **d** same as **a** and **b**, but coloured by meltwater content (blue colour scale). Summertime meltwater signal in water layers above 27.42 isopycnal is partly associated with solar warming (*Biddle et al.*, 2017, *Jacobs et al.*, 2011, *Jenkins et al.*, 2018, *Nakayama et al.*, 2013) so is masked in **d**. Meltwater contents calculated from noble gas tracers are indicated by dots overlaying the meltwater content calculated by ship-based hydrographic data in **d**. Figure 2.10a, 2.10b show the same plots as **a** and **b**, but coloured by absolute salinity.

2.3.2 Unambiguous meltwater signal in winter

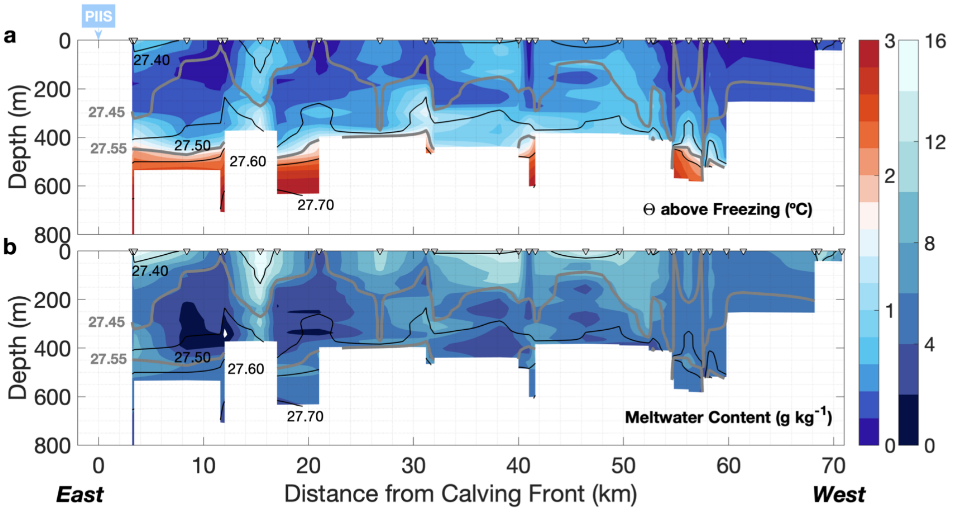

Figure 2.5: **Section 3, starts from the southeastern end of PIIS calving front and oriented following to the PIB gyre direction.** **a** Conservative temperature (Θ) above freezing (red–blue colour scale) and potential density isopycnals (in kg m^{-3}) contours from Section 3 (blue rectangle in Figure 2.1) collected by seals in winter 2014, with positions of the profiles marked as triangles at the top of the panel. **b** Same as **a**, but coloured by meltwater content (blue colour scale). Figure 2.11a, 2.11b show the same plots as **a** and **b**, but coloured by absolute salinity.

In austral winter, the consistently negative air-sea heat flux leads to a cold WW layer occupying the upper 400 m (Figure 2.3a, 2.4a, 2.5a, 2.6a). However, Figure 2.1 reveals a striking near-surface warm signature in front of PIIS spreading from the northeastern end of PIIS toward the southwest and along the coast toward Thwaites Ice Shelf, probably following the cyclonic PIB gyre. This water is about 0.6 °C above freezing, suggesting the existence of a heat source, which can only be the warm meltwater-rich water rising from the ice-shelf cavity that forms a warm near-surface meltwater-rich layer. Unlike summertime temperature measurements, which need noble gas data to confirm a near-surface meltwater content (*Biddle et al.*, 2017, *Jacobs et al.*, 2011, *Jenkins et al.*, 2018, *Nakayama et al.*, 2013), wintertime temperature data themselves are robust enough to allow us to unambiguously identify the presence of meltwater-rich water from the cold ambient water. Seal-tag profiles to the east of Thwaites Ice Shelf and in front of Dotson Ice Shelf, further west in the Amundsen Sea, also show a similar surface warming feature (Figure 2.13). We propose that this near-surface warming induced by the rising meltwater is a common but previously unidentified feature for warm-cavity ice shelves.

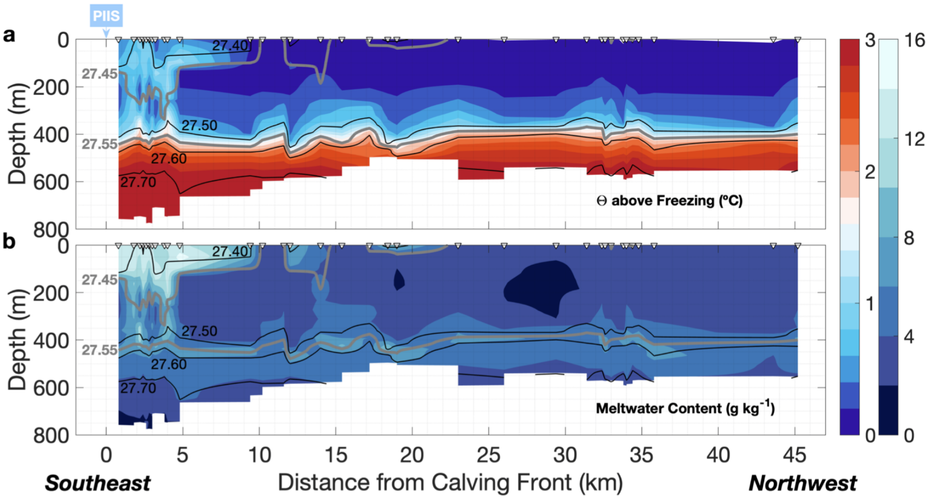

Figure 2.6: **Section 4, starts from the northwestern end of PIIS calving front and oriented opposite to the PIB gyre direction.** **a** Conservative temperature (Θ) above freezing (red–blue colour scale) and potential density isopycnals (in kg m^{-3}) contours from Section 4 (orange rectangle in Figure 2.1) collected by seals in winter 2014, with positions of the profiles marked as triangles at the top of the panel. **b** Same as **a**, but coloured by meltwater content (blue colour scale). Figure 2.12a, 2.12b show the same plots as **a** and **b**, but coloured by absolute salinity.

Close to PIIS (within about 5 km), unlike the relatively spatially uniform summertime meltwater distribution (Figure 2.2a, 2.3d, 2.4d), the wintertime meltwater distribution is highly heterogeneous both horizontally and vertically (Figure 2.2a, 2.3c, 2.4c, 2.5b, 2.6b). A near-surface meltwater-rich layer spreading above the cold WW (between the surface and the 27.45 isopycnal at about 250 m) and a deep meltwater-rich layer at around 450 m spreading below WW (near the 27.55 isopycnal) in front of PIIS, are clearly identified in all sections in winter (Figure 2.3c, 2.4c, 2.5b, 2.6b). There are meltwater-rich columns connecting the deep and near-surface meltwater-rich layers through the WW layer, while a large proportion of the WW remains meltwater-poor (Figure 2.2a, 2.2b, 2.3c, 2.4c, 2.5b, 2.6b). The meltwater-rich columns may be produced by sub-ice channels, which have been observed along the underside of the ice shelf (*Bindschadler et al.*, 2011, *Le Brocq et al.*, 2013, *Mankoff et al.*, 2012, *Payne et al.*, 2007). These channels can potentially focus the glacial meltwater outflow as an inverted stream of buoyant freshwater that is trapped beneath the ice shelf until it exits the cavity in the form of plumes (*Bindschadler et al.*, 2011, *Le Brocq et al.*, 2013, *Mankoff et al.*, 2012, *Payne et al.*, 2007).

To characterise the meltwater spreading away from PIIS in winter, we examine three sections that start from PIIS (Figure 2.4c, 2.5b, 2.6b). Section 2 starts at the southwestern end of PIIS and extends across the whole PIB gyre toward the northwest (green rectangle in Figure 2.1). The isopycnal doming associated with the PIB gyre is about 25 km further northwest in winter than summer in 2014 (Figure 2.4c, 2.4d). Similar to the meltwater distribution pattern in summer (Figure 2.4d), the meltwater distribution pattern in winter along Section 2 is concentrated near the ice-shelf front and the northwestern edge of the PIB gyre, and decreases towards the gyre centre (Figure 2.4c). Section 3 also starts from the southwestern end of the ice-shelf front, but extends to the west downstream in the PIB gyre (blue rectangle in Figure 2.1). In Section 3, we detect a meltwater distribution pattern very similar to Section 1 (Figure 2.3c), characterised by the two-layer structure and scattered meltwater-rich columns (Figure 2.5b). The similarity of the meltwater distribution between Sections 1 and 3 suggests that large amounts of meltwater are transported westwards, which may impede the meltwater flowing toward the gyre centre and therefore cause the meltwater-poor gyre centre identified in Section 2 (Figure 2.4c). Section 4 starts at the northeastern end of PIIS calving front and extends to the northwest against the direction of rotation of the PIB gyre (orange rectangle in Figure 2.1). The near-surface meltwater from PIIS is apparent up to about 23 km along Section 4 (extends against the PIB gyre circulation, Figure 2.6b), about 35 km along Section 2 (almost across the PIB gyre centre, Figure 2.4c) and at least 70 km along Section 3 (extends along the PIB gyre circulation, Figure 2.5b). These differences may further imply that the PIB gyre plays an important role in the distributions of meltwater and its associated heat, and probably also nutrients such as iron, in PIB.

Unlike the summertime strongly stratified upper ocean, surface cooling and wind stirring lead to a homogeneous mixed layer above the 27.55 isopycnal in winter in regions where the meltwater-rich water and the heat it carries are absent (Figure 2.3a, 2.4a, 2.5a, 2.6a). Therefore, the water above mCDW is denser in winter than in summer, which may allow meltwater-rich water to be comparably more buoyant and rise to a shallower depth in winter than in summer.

2.4 Discussion

The near-surface meltwater-rich layer appears to spread less far from PIIS than the deep meltwater-rich layer in Sections 2 and 4 in winter (Figure 2.4c, 2.6b). Wintertime surface air-sea-ice interaction processes could be partially responsible for this apparent rapid loss of near-surface meltwater content. As soon as the meltwater exits the cavity and reaches the surface (and prior to the measurements being recorded by seals), some of the meltwater-rich-water-related warm signal is likely to be quickly eroded by the strong surface cooling and likewise, the meltwater-related fresh signal may be obscured by brine rejected during sea ice formation (*Silvano et al.*, 2018). Thus, the actual heat and freshwater supply from the meltwater-rich water could be larger than implied by our surface temperature and salinity measurements. Figure 2.2b reveals that both an increase of salinity and a decrease of temperature can lower the value of calculated meltwater content. Typical wintertime heat (*ERA5*, 2017) and salt fluxes (*Tamura et al.*, 2008, 2011) induced by air-sea-ice interactions in front of PIIS might cause a decrease in meltwater content on the order of 2 g kg^{-1} day^{-1} (about 20 % of the averaged wintertime near-surface meltwater content, see Methods section 2.5).

Although the meltwater content calculated by wintertime hydrographic data may be decreased by surface processes, we suggest that it provides a reliable lower bound of the meltwater content rising to near surface in winter, because the observed meltwater-rich water signal near surface cannot be an artefact caused by solar warming, but only generated by meltwater-rich water itself. Noble gas measurements during both winter and summer would be necessary to accurately determine the extent of meltwater spreading (*Biddle et al.*, 2019, *Kim et al.*, 2016) but would be challenging to obtain in a region covered in sea ice for 10 months each year.

As mentioned above, there are meltwater-poor columns and two meltwater-rich layers in winter but not in summer (Figure 2.3c, 2.3d, 2.4c, 2.4d, 2.5b, 2.6b). We hypothesise that the seasonal meltwater distributions found in the WW layer are caused by the seasonal stratification (Figure 2.7). Previous research suggests that, in summer, when solar warming, sea ice melting and surface runoff stratify the WW layer (Figure 2.3b, 2.4b), the rising meltwater-rich water can tilt isopycnals and trigger a centrifugal instability and related intense lateral mixing (*Naveira Garabato et al.*, 2017). In contrast, in winter when surface cooling and wind mixing generate a homogeneous WW layer (Figure 2.3a, 2.4a, 2.5a, 2.6a), we propose that rising meltwater-rich water can penetrate through WW via the meltwater-rich columns without undergoing intense lateral mixing (Figure 2.7a). Therefore, in summer, the rising meltwater-rich water mixes intensely with the ambient water and spreads throughout the WW layer (Figure 2.3d, 2.4d), whereas in winter, it spreads through meltwater-rich columns in the WW layer and leaves the rest of the WW layer meltwater-poor (Figure 2.3c, 2.4c, 2.5b, 2.6b). Consequently, the spatial and temporal inhomogeneities of meltwater distribution are reduced in summer but strongly maintained in winter.

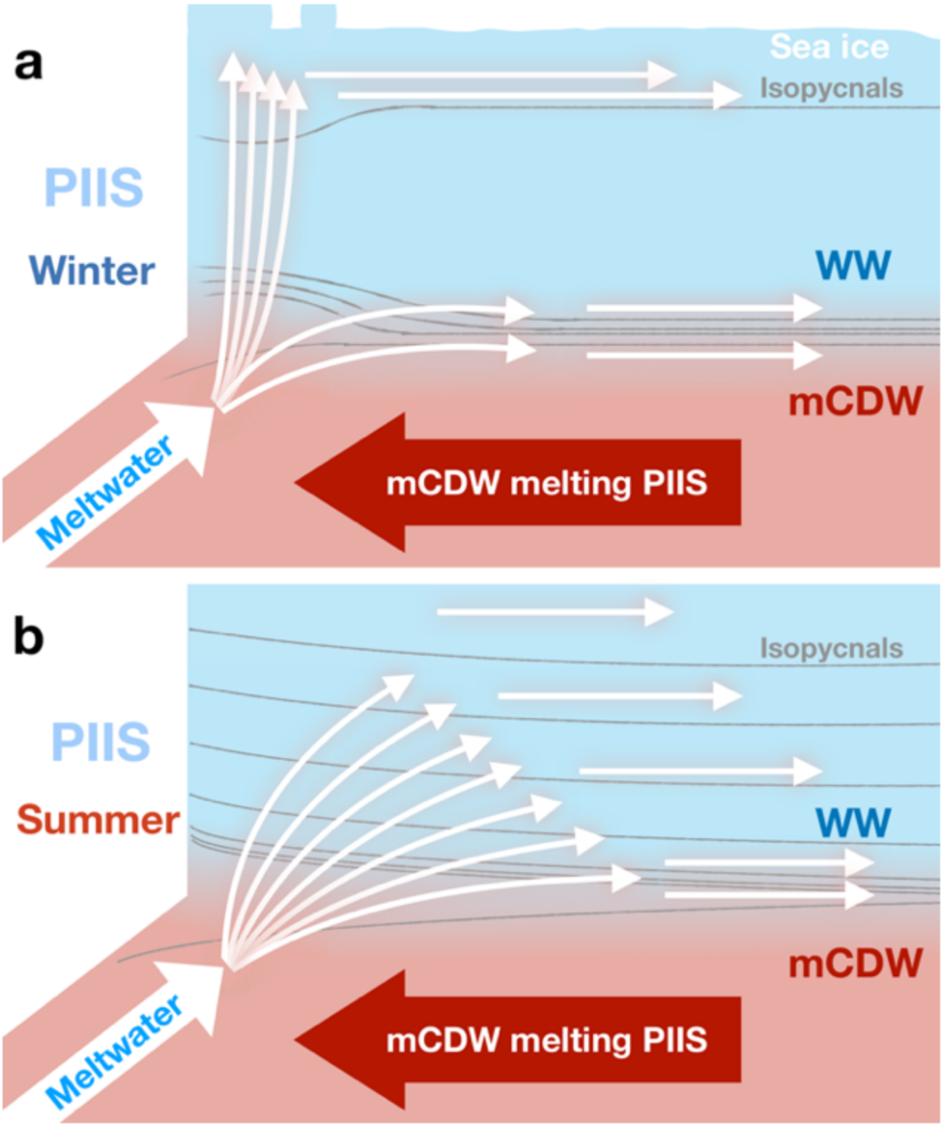
a
PIIS
Winter
Sea ice
Isopycnals
WW
mCDW
Meltwater
mCDW melting PIIS
b
PIIS
Summer
Isopycnals
WW
mCDW
Meltwater
mCDW melting PIIS

Figure 2.7: **Schematic representation of the meltwater-rich water pathways in winter and summer. a** Wintertime meltwater-rich water either spreads along pycnocline or rises through uniform water layers without undergoing intense lateral mixing. Wintertime meltwater-rich water rising to near surface melts sea ice and forms polynyas. **b** Summertime meltwater-rich water spreads along pycnocline as well. However, in contrast to wintertime meltwater-rich water, summertime rising meltwater-rich water penetrating through stratified water mixes with ambient water intensively and spreads widely.

Near the outflow region of the Totten Ice Shelf, a warm-cavity ice shelf in East Antarctica, an unstratified upper ocean, similar to the WW layer in front of PIIS in winter, was observed when sea ice blocks solar warming in summer (*Silvano et al.*, 2017). Just as we identify in front of PIIS in winter, the meltwater distribution near Totten Ice Shelf is variable (*Silvano et al.*, 2017), which may suggest that the mixing between the meltwater-rich water and the ambient water is also weak in the unstratified near-surface layer near the Totten Ice Shelf. This supports our hypothesis that upper-ocean stratification strongly influences the upward motion of basal meltwater-rich water from warm-cavity ice shelves.

The two layers of meltwater-rich water in winter suggest that different mechanisms create and/or control them. The melt rate of PIIS can vary by more than one order of magnitude within a month (*Davis et al.*, 2018) and might form meltwater-rich water with different buoyancies (*Kimura et al.*, 2016). As the wintertime upper ocean dominated by WW is uniform, meltwater-rich water with density greater than WW (about 1027.56 kg m^{-3}) remains in the pycnocline below the WW layer while the remaining less dense meltwater-rich water can rise. Process model results show that meltwater-rich water with a buoyancy of 2×10^{-3} m s^{-2}, equivalent to a density of about 1027.36 kg m^{-3}, will be trapped in stratified water and cannot surface (*Naveira Garabato et al.*, 2017). Therefore, the pycnocline at the mCDW-WW interface year-round may trap part of the rising meltwater-rich water and contribute to the deep meltwater-rich layer, while the meltwater-rich water with a density less than 1027.36 kg m^{-3} is likely to surface.

The seasonal meltwater distribution may vary interannually due to a range of processes. For example, in high-melting years, meltwater-rich water tends to be more buoyant and more likely to rise across isopycnals and reach a shallower depth (*Kimura et al.*, 2017, *Naveira Garabato et al.*, 2017). In addition, interannual variability of the temperature and volume of mCDW might change the meltwater distribution by changing the melt rate and the pycnocline depth, where the deep meltwater-rich layer is located. The presence of sea ice blocking solar radiation could also alter the summertime meltwater distribution by weakening the solar-warming-related stratification of the upper ocean, as occurs near Totten Ice Shelf (*Silvano et al.*, 2018). The spatially uniform meltwater distribution therefore may not be apparent in summer every year. However, due to the persistently negative net heat flux and strong wind stirring in winter, the wintertime upper-ocean stratification tends to be consistently weak. Thus, the highly variable meltwater distribution and weak lateral mixing of the rising meltwater-rich water seen in winter 2014 are likely to be representative of winter in other years.

We acknowledge several caveats to these results. First, we only have one year of seal-tag data in front of PIIS. One year is not enough to capture the long-term mean wintertime meltwater distribution nor its interannual variability in response to the large-scale forcing from, for example, El Niño–Southern Oscillation and the Southern Annular Mode, which may affect the meltwater distribution as the ocean state in front of PIIS is changed (*Dutrieux et al.*, 2014, *Nakayama et al.*, 2018). More data in winter are required. Second, the value of calculated meltwater content is sensitive to the choice of endpoints (see Methods section 2.5). Meltwater-poor profiles were identified in front of PIIS in summer 2009 and 1994 (*Jacobs et al.*, 2011). However, a meltwater calculation using the 2009 and 1994 data with the same endpoints as our study cannot reproduce the same summertime meltwater-poor feature. The values of end-points of 2014 summertime WW are determined based on the WW formed in the previous winter (i.e. 2013 winter). WW properties are likely to vary interannually, but we assume here that the WW has been fully replenished in 2014.

If rising meltwater-rich water penetrates through the WW layer with less intense mixing, it can rise to near surface nearly unmodified. Wintertime meltwater-rich water is significantly more concentrated near surface than at depth, which may maintain more iron in the euphotic zone (i.e. upper 200 m) to boost productivity in the following spring (*St-Laurent et al.*, 2019). The heat transported by the meltwater-rich water can increase the temperature of the near-surface layer up to about 1 °C above freezing (Figure 2.1). Previous studies have pointed out that the residual meltwater near surface could maintain polynyas (*Bindschadler et al.*, 2011, *Le Brocq et al.*, 2013, *Mankoff et al.*, 2012). We therefore argue that the heat from meltwater-rich water that we observe is likely to prevent sea ice formation, allow melting of sea ice and thus increase the spatial extent of local polynyas in front of ice shelves. The strong offshore wind near the ice-shelf front may also transport warm near-surface water further away from PIIS and expand the meltwater-influenced region. The enlarged polynyas can then lead to enhanced air-sea fluxes and have further impacts on iceberg calving (*Heywood et al.*, 2014, *Mankoff et al.*, 2012, *Silvano et al.*, 2018) and ice-shelf melting (*Fogwill et al.*, 2015, *Silvano et al.*, 2018). The rising of meltwater-rich water might even reinforce the water mass exchanges and local ventilation near the ice shelf, as well as the reported overturning circulation (*Jourdain et al.*, 2017, *Naveira Garabato et al.*, 2017, *Webber et al.*, 2019) to bring more warm water into the ice cavity to melt the ice shelf (*Webber et al.*, 2019). Because meltwater is critical to local ventilation (*Jourdain et al.*, 2017, *Nakayama et al.*, 2013, *Naveira Garabato et al.*, 2017, *Webber et al.*, 2019) and sea ice conditions (*Bindschadler et al.*, 2011, *Mankoff et al.*, 2012, *Silvano et al.*, 2018), representation of meltwater in climate models as uniform layers at specific depths without seasonality could lead to significant biases in the representation of ocean circulation, ocean-ice-shelf interaction, and surface heat exchanges.

2.5 Methods

2.5.1 Ship-based datasets

We used conductivity-temperature-depth (CTD) profiles, vertical-microstructure profiler (VMP-2000) temperature and salinity yoyo profiles, and noble gas measurements obtained during expedition JR294/295 (*Heywood et al.*, 2014), which took place on the RRS James Clark Ross under the Ocean2ice project of the UK's Ice Sheet Stability programme (iSTAR, `http://www.istar.ac.uk`). The CTD was a Sea-Bird SBE 911 with two sensor pairs of conductivity and temperature. Temperature was calibrated using a Sea-Bird SBE 35 deep thermometer while salinity was calibrated using a Guildline Autosal salinometer. CTD data were averaged into 2-dbar pressure bins. We follow the Thermodynamic Equations of Seawater-10 standard (*McDougall and Barker*,

2011) for all hydrographic data. Full details of ship-based measurements can be found in the JR294/295 cruise report at `https://www.bodc.ac.uk/resources/inventories/cruise_inventory/reports/jr294.pdf`.

Nine CTD stations were occupied along PIIS calving front (see diamonds in the pink rectangle in Figure 2.1, the median and mean distances from PIIS to the locations of CTD stations were both 0.5 km) on 11 February 2014 and seven additional CTD stations were occupied perpendicular to PIIS towards to northwest from 9 to 20 February 2014.

Fifty-eight VMP profiles of temperature and salinity were obtained along PIIS calving front (thick black line in the pink rectangle in Figure 2.1, the median and mean distances from PIIS to the locations of VMP stations were about 1 and 1.5 km, respectively) deployed on 12 and 13 February 2014. Salinity data collected from VMP were calibrated against the calibrated salinity data from CTD. VMP data were averaged into 0.25-dbar pressure bins.

Seventy-one noble gas samples were collected at the CTD stations along PIIS calving front in copper tubes and sealed by crimping at both ends (*Loose et al.*, 2016). Noble gas samples were analysed in the Isotope Geochemistry Facility at Woods Hole Oceanographic Institution. Dissolved gas extracted from the water is captured into aluminosilicate glass bulbs that are maintained at a liquid nitrogen bath at 196 C. Then the bulbs are attached to a dual mass spectrometric system and analysed for He, Ne, Ar, Kr and Xe (*Stanley et al.*, 2009). The noble gas are isolated on two cryogenic traps and selectively warmed to sequentially release each gas into the Hiden Quadrupole Mass Spectrometer for measurement by peak height manometry (*Lott et al.*, 2001). The reproducibility from $N = 6$ duplicate samples for noble gas is between 0.1 and 1.8 % and the analytical precision for noble gas is about 0.5–1 % (*Stanley et al.*, 2009). Noble gas are reported in micromoles per kilogram. We only use neon, argon, krypton and xenon in this study as the helium content can be influenced by mantle sources (*Loose et al.*, 2018).

2.5.2 Seal-tag hydrographic dataset

Seven southern elephant seals (Mirounga leonina) and seven Weddell seals (Leptonychotes weddellii) were captured and tagged with CTD-Satellite Relayed Data Loggers (*Boehme et al.*, 2009) during the same cruise under the same project (iSTAR) around the Amundsen Sea in February 2014. Three tagged seals occupied Pine Island Bay while the tags kept measuring and transmitting data during winter. For our study, we defined four seal-tag CTD sections: Section 1 is oriented along the PIIS calving front (pink rectangle in Figure 2.1), Section 2 extends from the southeastern end of the ice-shelf front towards the northwest (green rectangle in Figure 2.1), Section 3 extends from the southeastern end of the PIIS calving front towards the west along the coast downstream with the PIB gyre circulation (blue rectangle in Figure 2.1), and Section 4 extends from the northeastern end of the PIIS calving front towards the northwest upstream opposing the PIB gyre circulation (orange rectangle in Figure 2.1). All measurements included in these four sections were collected by the same female southern elephant seal (# EF838). The median and mean distances from PIIS to the locations of seal-tag CTD measurements are about 1.5 and 2 km, respectively.

We bin-average the seal-tag profiles along each section using a horizontal bin size of 200 m. Most bins contain only one profile (Section 1 has 41 bins, including 6 bins that contain two profiles and the 35 bins that contain one profile; Section 2 has 12 bins, including 1 bin that contains two profiles and 11 bins that contain one profile; Section 3 has 30 bins, including 2 bins that contain two profiles and 28 bins that contain one profile; Section 3 has 30 bins, including 3 bins that contain three profiles, 4 bins that contain two profiles and 23 bins that contain one profile). All profiles used to produce transect plots are collected between 1 July 2014 and 10 September 2014 (Figure 2.14), when there is no solar radiation and when sufficient cooling, combined with wind mixing, leads to a consistent mixed layer of cold WW with no summer stratification and warm near-surface water remaining. The sampling biases of temperature measurements and related meltwater content are negligible, compared to the meltwater-induced variability.

The seals' tags sample the temperature, salinity and pressure every 2 seconds then apply a 5-second median filter on the time series (*Boehme et al.*, 2009). To reduce data transmission time, tags only select 18 depths to be transmitted to the Argos satellite system (*Boehme et al.*, 2009, *Photopoulou et al.*, 2015). Each CTD profile was programmed to include measurements at 2 dbar, the depth maximum, the temperature minimum and the deep (over 100 dbar) temperature maximum to ensure data from near surface, centre of WW and CDW are included in the dataset. In addition to these four measurements, the other 14 measurements were chosen at equally spaced depths between the sea surface and the maximum depth. Tags measure only when seals ascend from their dives as seals tend to ascend nearly vertically. Only the deepest cast in every 4 h is transmitted (*Boehme et al.*, 2009, *Fedak et al.*, 2002, 2004). We accessed fully-quality-controlled linearly interpolated data from Marine Mammals Exploring the Oceans Pole to Pole (*Roquet et al.*, 2013, 2014) (`http://www.meop.net/`; MEOP). We further remove two data points with abnormally high salinity values collected on 8 August 2014. Estimated accuracy is ±0.03 °C for temperature and ±0.05 g kg^{-1} for salinity. Full details can be found at `http://www.meop.net/meop-portal/ctd-data.html`.

2.5.3 Calculation of meltwater content from hydrographic data

We use the composite-tracer method (*Jenkins*, 1999) for meltwater fraction calculation. The water masses used in this calculation are mCDW, WW and glacial meltwater. Tracers are conservative temperature (Θ) and absolute salinity (S_A) for all hydrographic data and are assumed to be conservative. In temperature-salinity space (Figure 2.2b, 2.2c), two lines connect the core characteristics of mCDW, WW and glacial meltwater: the mCDW-WW mixing line, where the mixture of mCDW and WW lies and mCDW-meltwater mixing line (i.e. Gade line (*Gade*, 1979)), where the mixture of mCDW and meltwater lies. The mixture of CDW, WW and meltwater lies between these two lines. The fractions of water masses at a data point are then determined by the distance that the point lies from the lines, derived from CTD measurements:

$$\varphi_{meltwater} = \frac{\Theta_{observed} - \Theta_{mCDW} - \frac{(S_{A_{observed}} - S_{A_{mCDW}}) \times (\Theta_{WW} - \Theta_{mCDW})}{(S_{A_{WW}} - S_{A_{mCDW}})}}{\Theta_{meltwater} - \Theta_{mCDW} - \frac{(S_{A_{meltwater}} - S_{A_{mCDW}}) \times (\Theta_{WW} - \Theta_{mCDW})}{(S_{A_{WW}} - S_{A_{mCDW}})}} \tag{2.5.1}$$

where $\varphi_{meltwater}$ is the meltwater fraction and Θ and S_A with subscripts are the observed values or the characteristic properties (i.e. end-points) of water masses.

We chose the end-points following previously published research, where adjustments were made to the WW endpoints to ensure the optimal alignment between the meltwater content derived from temperature, salinity, and oxygen alone, and the meltwater content derived from noble gases (*Biddle et al.*, 2019). The values of WW end-points (-1.86 °C of Θ_{WW} and 34.32 g kg^{-1} of $S_{A_{WW}}$) were derived by Biddle et al. ("pure WW" of *Biddle et al.*, 2019) and do not vary seasonally. When we define the end-points for the meltwater, we consider it as an ice cube rather than a water parcel–as the meltwater comes from the interaction between the mCDW and the ice shelf. The $\Theta_{meltwater}$ is calculated from the heat required to bring the far-field ice temperature (between -20 and -15 °C) to the melting temperature and the latent heat of fusion (*Gade*, 1979). The end-points for the meltwater used in this study are therefore -90.8 °C for $\Theta_{meltwater}$ and 0 g kg^{-1} for $S_{A_{meltwater}}$ and do not vary seasonally (*Biddle et al.*, 2017). The values of mCDW end-points (1.15 °C of Θ_{mCDW} and 34.87g kg^{-1} of S_A) come from hydrographic data collected in PIB in summer (*Biddle et al.*, 2017). Our seal-tag data from PIB reveal the Θ_{mCDW} to be about 0.03 °C higher in summer (1.15 °C) than in winter (1.12 °C) while $S_{A_{mCDW}}$ is almost unchanged seasonally (Figure 2.15). To estimate the uncertainty induced by the seasonal change in the mCDW endpoint, we re-calculated the meltwater content in our four wintertime sections using the wintertime endpoint. The meltwater content calculated with the wintertime endpoint values is slightly higher than the value calculated with summertime endpoint values (mean and median values increase, respectively, of 5.1% and 2.2% for Sections 1, 4.8% and 5.2% for Sections 2, 2.7% and 1.5% for Section 3, and 3.7% and 1.7% for Section 4) but the pattern of meltwater distribution remains the same. The comparison between the calculations using summertime and wintertime end-points is shown in Figure 2.16–2.19.

To estimate the uncertainty induced by the limited accuracy of the seal-tag hydrographic data, we run a Monte Carlo simulation on a set of 200 randomly generated hydrographic measurements. We perturb each simulated measurement 5000 times with normally distributed perturbations varying up to the largest uncertainty of seal-tag data (±0.03 °C for temperature and ±0.05 g kg^{-1} for salinity, Figure 2.20). We find these uncertainties in seal-tag hydrographic data can cause an uncertainty of ±2.87 g kg^{-1} in the calculated meltwater content (Supplementary Figure 2.21), which is about 30% of the averaged wintertime near-surface meltwater content. Nonetheless, we have confidence in the spatial distribution of hydrographic features in our study because all profiles we used in our four seal-tag sections were collected by a single Elephant Seal.

These uncertainty estimates suggest some sensitivity of the absolute values of meltwater content to the accuracy of chosen end-points and observational measurements. However, we do not expect a qualitative change to the pattern of meltwater content.

2.5.4 Quantifying the effect of wintertime surface cooling on derived meltwater values

In front of PIIS, the net heat flux calculated from ERA5 reanalysis data (*ERA5*, 2017) from 2014 winter (July–September) is on the order of 3×10^7 J m^{-2} day^{-1} and the 10-year climatology (2004–2013) net salt flux in winter produced by *Tamura et al.* (2011) is on the order of 1 kg m^{-2} day^{-1}. Note that, the datasets of surface fluxes we use here may contain substantial uncertainties in front of PIIS. If we assume that the surface cooling and brine rejection can only affect the mixed layer and the mixed-layer depth is 400 m, the heat and salt fluxes can cause a temperature decrease on the order of 0.02 °C day^{-1} and a salinity increase on the order of 3×10^{-3} g kg^{1} day^{-1} , which would be approximately equivalent to an apparent 2 g kg^{-1} day^{-1} decrease (equivalent to about 20% of the averaged wintertime near-surface meltwater content) in derived meltwater in front of PIIS.

2.5.5 Calculation of meltwater content from noble gas datasets

The water masses used in this calculation are mCDW, air equilibrated water (AEW) and glacial meltwater. AEW is directly affected by the atmosphere and represents surface saturation values of the NG (*Loose et al.*, 2014). The end-points used for mCDW, AEW and meltwater chosen following previous research are: 8.12×10^{-3} , 8.43×10^{-3} and 91.6×10^{-3} μmol kg^{-1} for Ne; 16.42, 17.52 and 44.46 μmol kg^{-1} for Ar; 4.01×10^{-3} , 4.43×10^{-3} and 5.84×10^{-3} μmol kg^{-1} for Kr; 0.604×10^{-3} , 0.660×10^{-3} and 0.414×10^{-3} μmol kg^{-1} for Xe.

As the number of NG-tracer constraints plus mass conservation are more than the number of water masses to be identified in this calculation, we use Optimum Multiparameter Analysis to calculate the water mass fractions (*Biddle et al.*, 2017, *Loose et al.*, 2014). This calculation uses a least-squares regression with a nonnegativity constraint for our overdetermined equation:

$$\begin{pmatrix} Ne_{mCDW} & Ne_{AEW} & Ne_{meltwater} \\ Ar_{mCDW} & Ar_{AEW} & Ar_{meltwater} \\ Kr_{mCDW} & Kr_{AEW} & Kr_{meltwater} \\ Xe_{mCDW} & Xe_{AEW} & Xe_{meltwater} \\ 1 & 1 & 1 \end{pmatrix} \begin{pmatrix} \varphi_{mCDW} \\ \varphi_{AEW} \\ \varphi_{meltwater} \end{pmatrix} = \begin{pmatrix} Ne_{obs} \\ Ar_{obs} \\ Kr_{obs} \\ Xe_{obs} \\ 1 \end{pmatrix} \tag{2.5.2}$$

where the φ is the fractions of water masses and names of noble gas with water masses subscripts are the observed values or the characteristic properties of water masses. The reliability of meltwater content calculated from noble gas data is estimated by *Biddle et al.* (2019) to be ± 0.5 g kg^{-1}.

2.6 Supplementary information

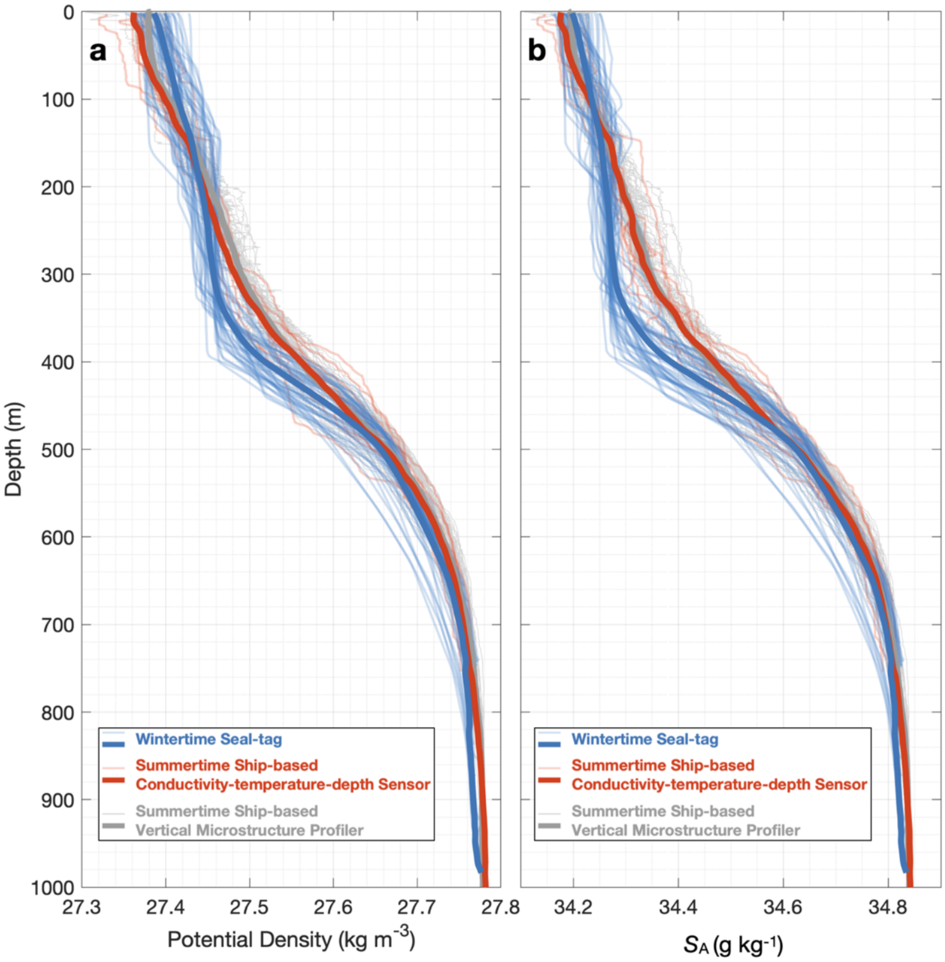

Figure 2.8: **Potential density and absolute salinity (S_A) in front of PIIS.** **a** The observed values (thin lines and dots) and the depth-mean values (thick lines) passed through a 10-m moving-average filter of potential density in section 1 (pink rectangle in Figure 2.1) profiles collected by seals (blue) in winter 2014 and ship-based hydrographic data collected by conductivity-temperature-depth sensor (red) and vertical microstructure profiler (grey) in summer 2014. **b** same as **a** but for absolute salinity.

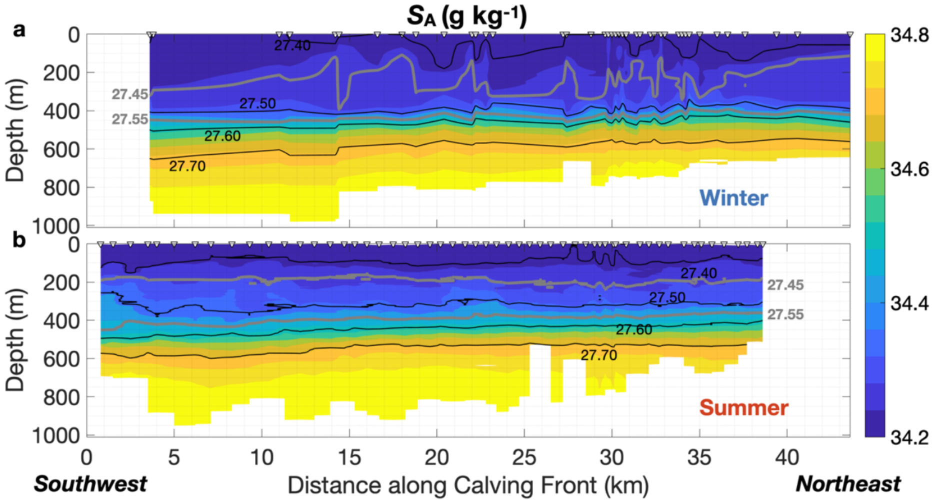

Figure 2.9: **Absolute salinity (S_A) of section 1, along the PIIS calving front, from southwest to northeast.** **a** Absolute salinity (S_A, yellow-blue colour scale)) and potential-density isopycnals (in kg m^{-3}) contours from section 1 (pink rectangle in Figure 2.1) collected by seals in austral winter (Jul–Sep) 2014, with positions of profiles marked as triangles at the top of the panel. **b** Same as **a**, but for data from hydrographic profiles collected by ship-based vertical microstructure profiler in February 2014.

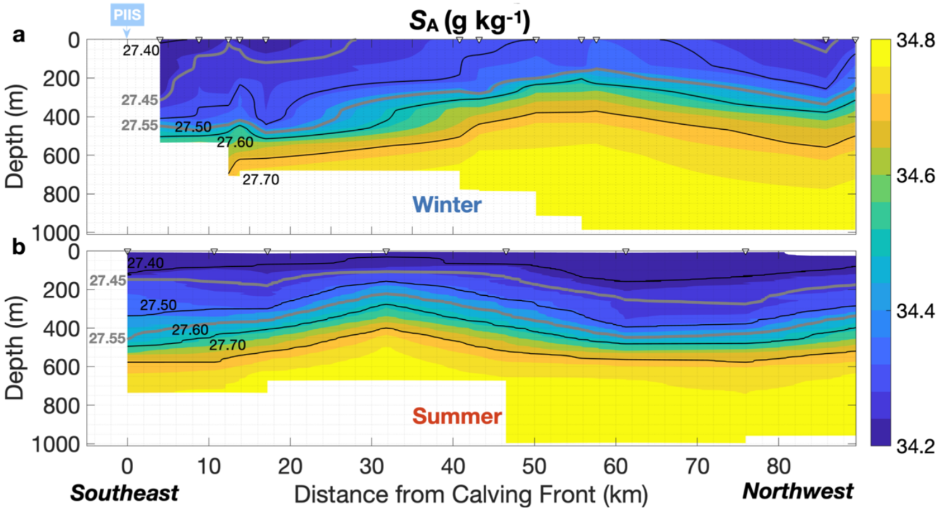

Figure 2.10: **Absolute salinity (S_A) of section 2, from the southwestern end of the PIIS calving front towards the northwest.** **a** Absolute salinity (S_A, yellow-blue colour scale) and potential-density isopycnals (in kg m^{-3}) contours from section 2 (green rectangle in Figure 2.1) collected by seals in winter 2014, with positions of profiles marked as triangles at the top of the panel. **b** Same as **a**, but for data from ship-based hydrographic profiles collected by conductivity-temperature-depth sensor in February 2014.

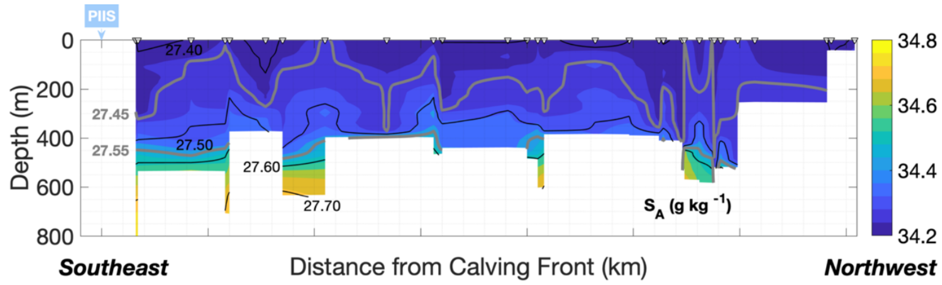

Figure 2.11: **Absolute salinity (S_A) of section 3, starts from the southeastern end of PIIS calving front and oriented following to the PIB gyre direction.** Absolute salinity (S_A, yellow-blue colour scale) and potential-density isopycnals (in kg m^{-3}) contours from section 3 (blue rectangle in Figure 2.1) collected by seals in winter 2014, with positions of the profiles marked as triangles at the top of the panel.

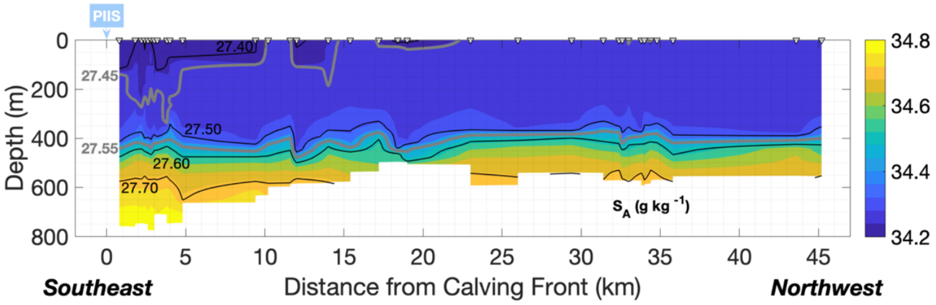

Figure 2.12: **Absolute salinity (S_A) of section 4, starts from the northwestern end of PIIS calving front and oriented opposite to the PIB gyre direction.** Absolute salinity (S_A, yellow-blue colour scale) and potential-density isopycnals (in kg m^{-3}) contours from section 4 (orange rectangle in Figure 2.1) collected by seals in winter 2014, with positions of the profiles marked as triangles at the top of the panel.

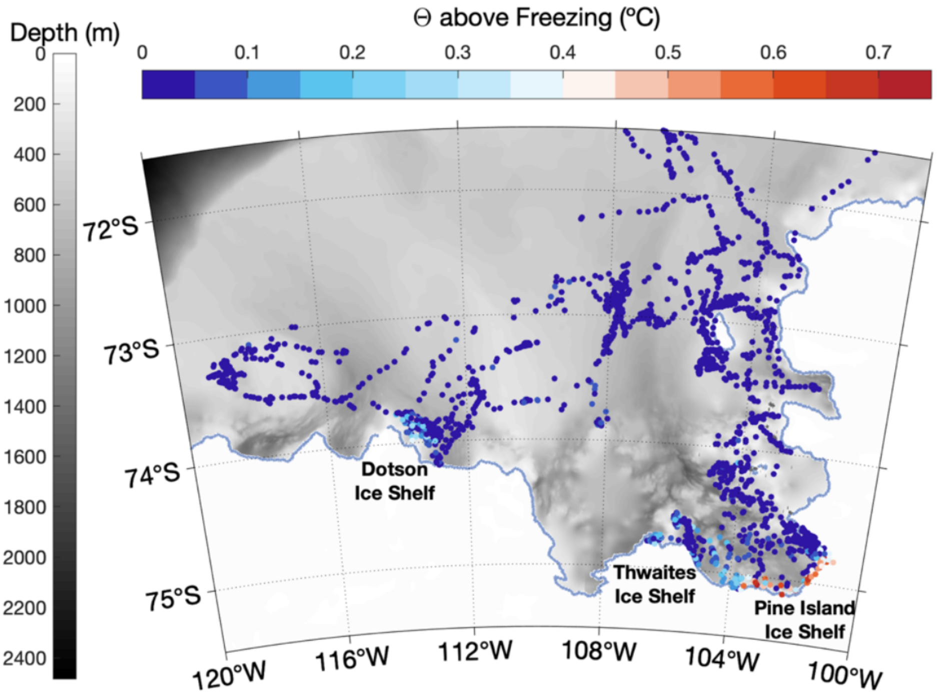
Depth (m)
0
200
400
600
800
1000
1200
1400
1600
1800
2000
2200
2400
Θ above Freezing (°C)
0
0.1
0.2
0.3
0.4
0.5
0.6
0.7
72°S
73°S
74°S
75°S
120°W
116°W
112°W
108°W
104°W
100°W
Dotson Ice Shelf
Thwaites Ice Shelf
Pine Island Ice Shelf

Figure 2.13: **Map of the whole Amundsen Sea.** Dots indicating the positions of the seal-tag hydrographic profiles collected in winter (July to September) 2014 are coloured by the conservative temperature, Θ, above freezing at 2 dbar. The relatively warm water is identified along the coastline near PIB and the east of Dotson Ice Shelf.

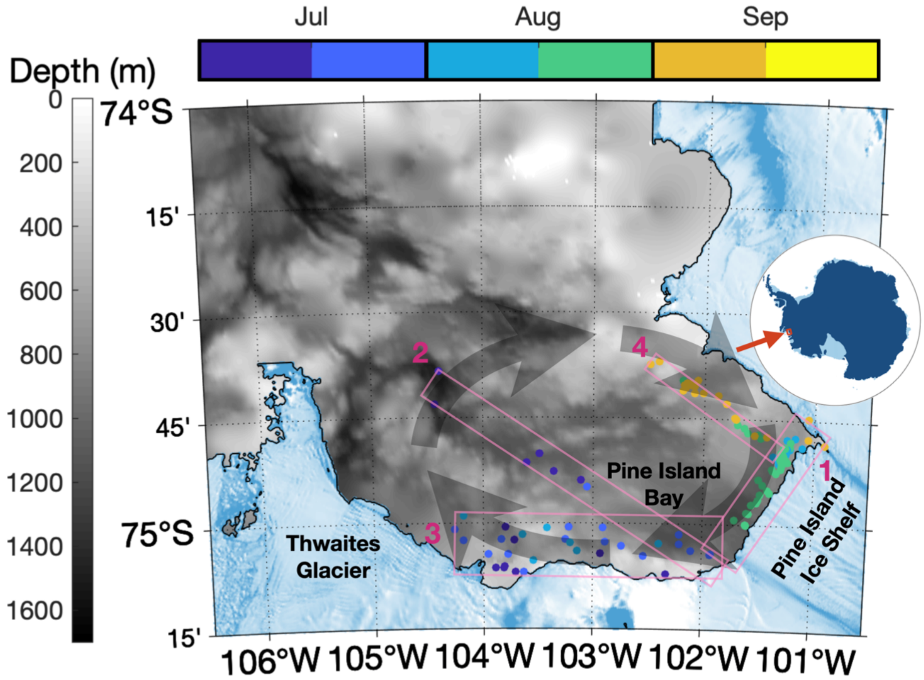
Jul
Aug
Sep
Depth (m)
0
200
400
600
800
1000
1200
1400
1600
74°S
15'
30'
45'
75°S
15'
106°W
105°W
104°W
103°W
102°W
101°W
1
2
3
4
Pine Island Bay
Thwaites Glacier
Pine Island Ice Shelf

Figure 2.14: **The months when seal-tag profiles were collected.** Dots indicating the positions of the seal-tag hydrographic profiles collected in each section in winter (July to September) 2014 are coloured by the months when data were collected.

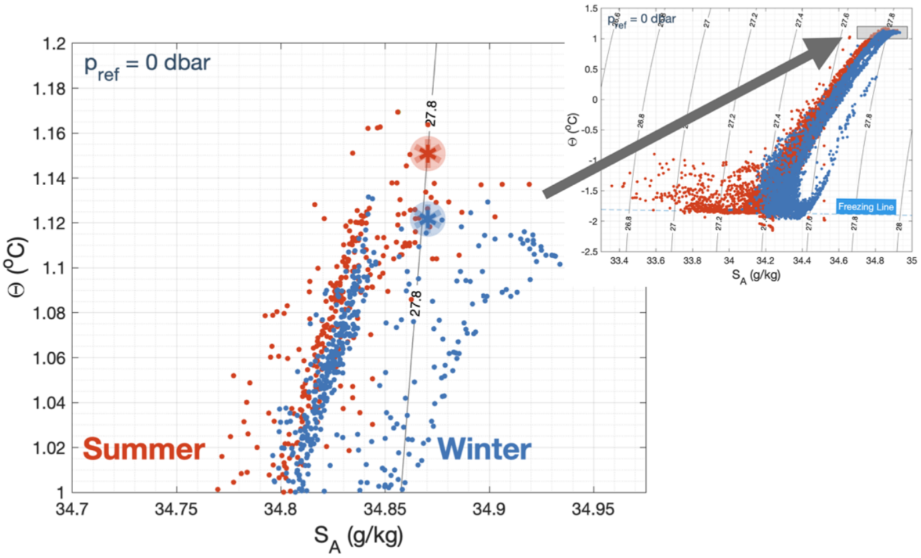

Figure 2.15: **The Θ–S_A diagram zoomed in for mCDW in PIB.** The dots in blue and red indicate the data collected in winter and summer, respectively. The stars in blue and red indicate the mCDW endpoints in winter and summer separately. Inset shows the Θ–S_A, diagram of all data collected in PIB in 2014.

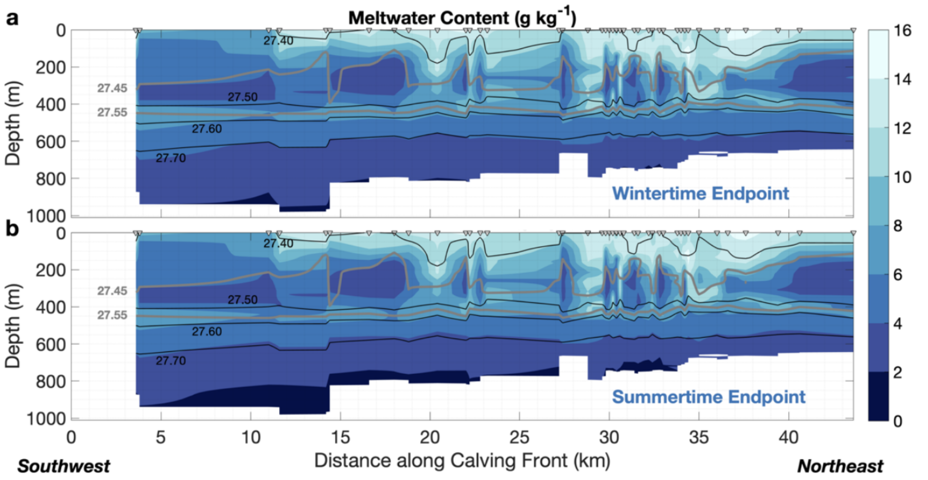

Figure 2.16: **The meltwater content of section 1, along the PIIS, from southwest to northeast.** The meltwater content is calculated using **a** wintertime endpoint values and **b** summertime endpoint values. The positions of the profiles are marked as triangles at the top of the panel.

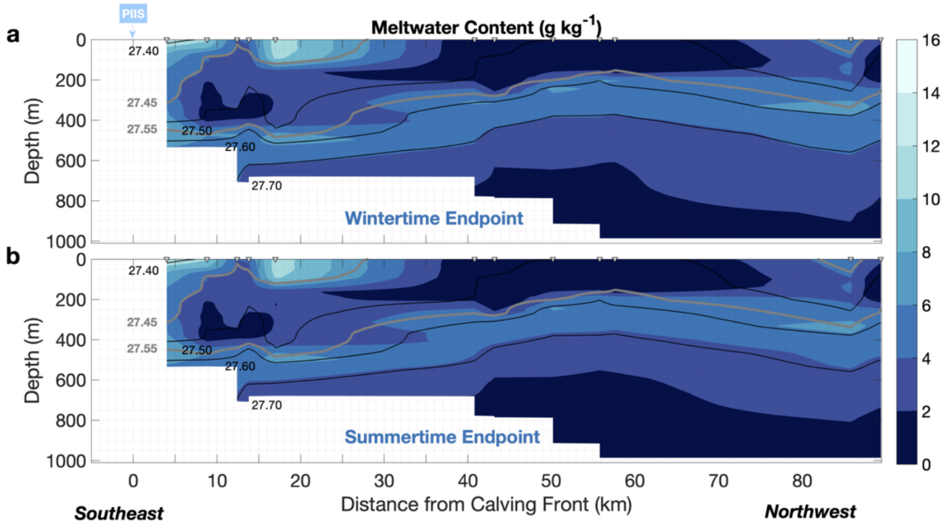

Figure 2.17: **The meltwater content of section 2, from the southwestern end of the PIIS calving front towards the northwest.** The meltwater content is calculated using **a** wintertime endpoint values and **b** summertime endpoint values. The positions of the profiles are marked as triangles at the top of the panel.

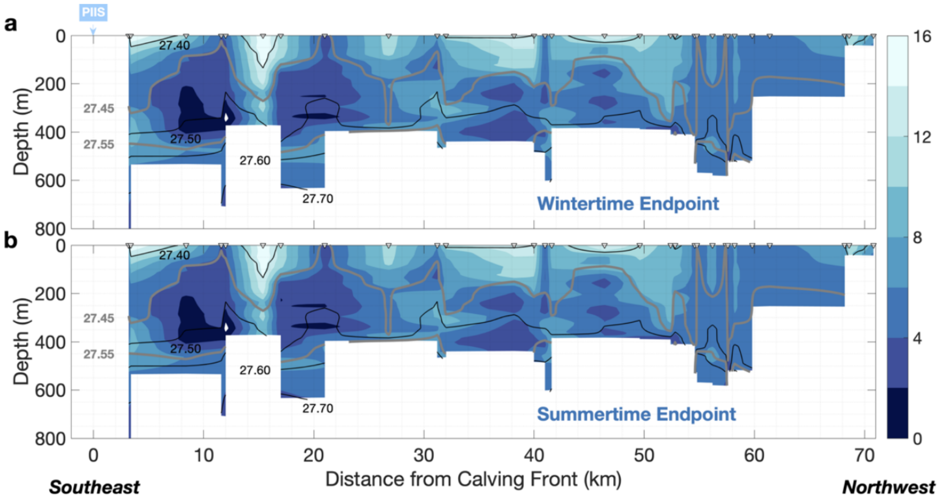

Figure 2.18: **The meltwater content of section 3, starts from the southeastern end of PIIS calving front and oriented following to the PIB gyre direction.** The meltwater content is calculated using **a** wintertime endpoint values and **b** summertime endpoint values. The positions of the profiles are marked as triangles at the top of the panel.

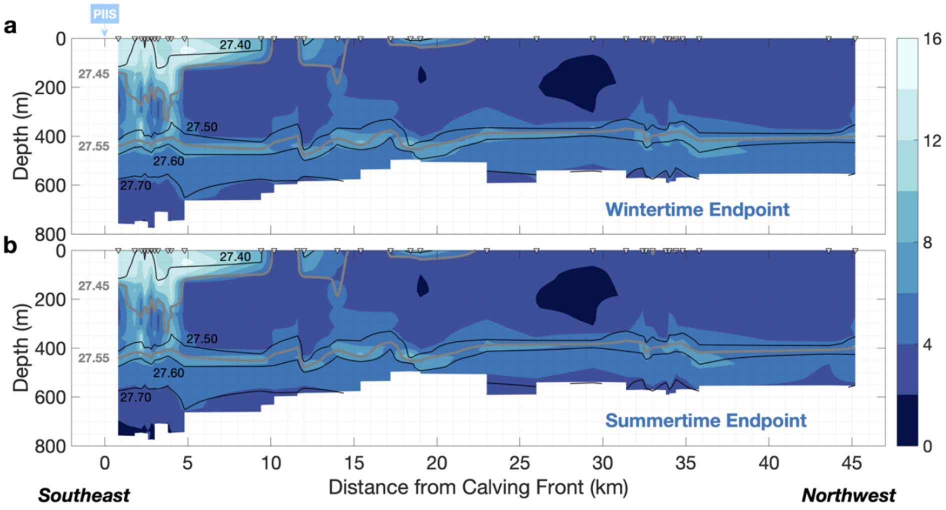

Figure 2.19: **The meltwater content of section 4, starts from the northwestern end of PIIS calving front and oriented opposite to the PIB gyre direction.** The meltwater content is calculated using **a** wintertime endpoint values and **b** summertime endpoint values. The positions of the profiles are marked as triangles at the top of the panel.

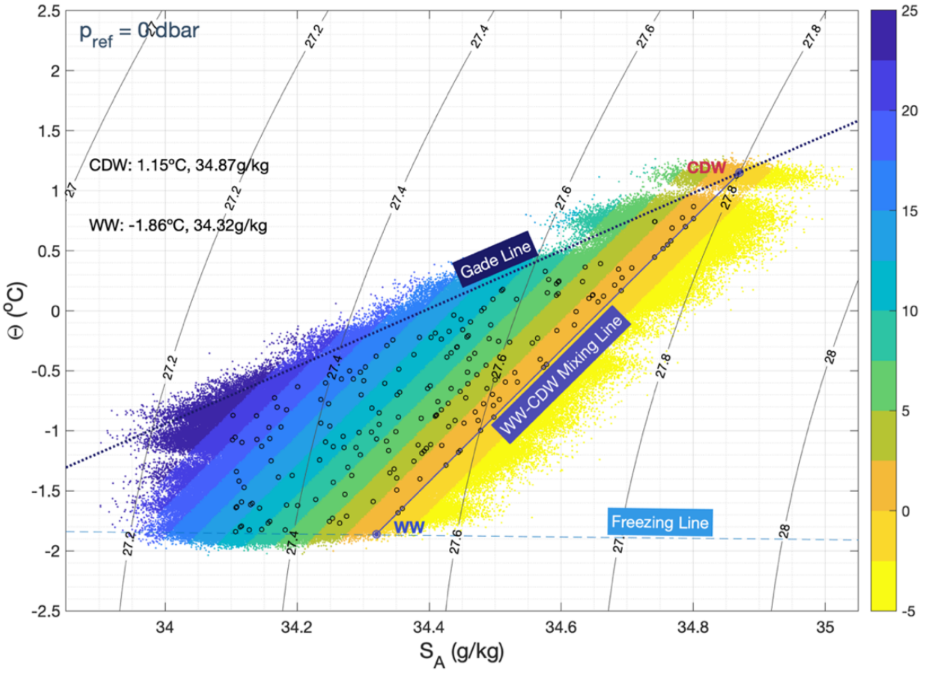

Figure 2.20: **The Θ–S_A diagram of all data generated for Monte-Carlo simulation.** The black circles represent the two-hundred randomly-generated hydrographic measurements. The dots shaded by the meltwater content represent the 10,000 perturbed observations. WW and mCDW endpoints are marked by dots near "WW" and "mCDW" texts. Isopycnals are indicated by solid black lines with labels.

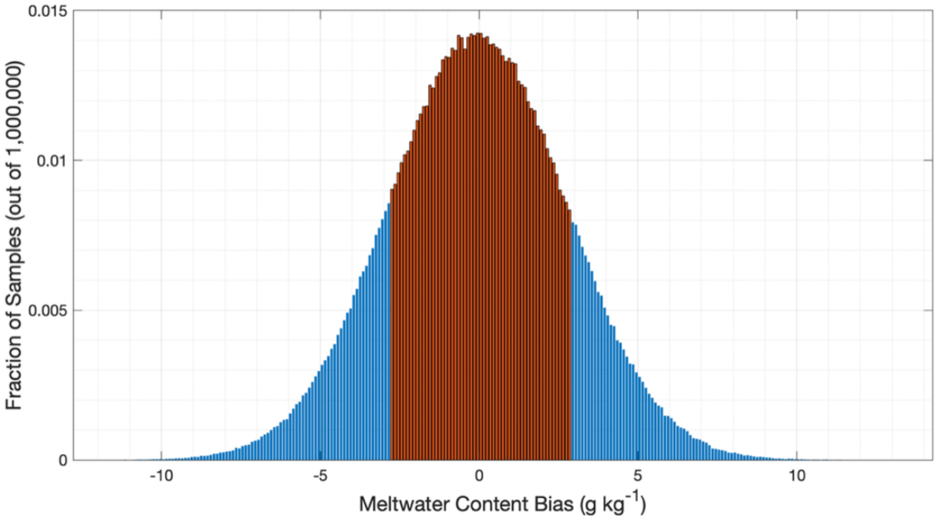

Figure 2.21: **Histograms showing the meltwater content bias induced by seal-tag data accuracy using Monte Carlo simulations.** Bias within one standard deviation are highlighted in orange.

3

Reversal of ocean gyres near ice shelves in the Amundsen Sea caused by the interaction of sea ice and wind

3.1 Abstract

Floating ice shelves buttress the Antarctic Ice Sheet, which is losing mass rapidly mainly due to ocean-driven melting and the associated disruption to glacial dynamics. The local ocean circulation near ice shelves is therefore important for the prediction of future ice mass loss and related sea-level rise as it determines the water mass exchange, heat transport under the ice shelf and resultant melting. However, the dynamics controlling the near-coastal circulation are not fully understood. A cyclonic (i.e. clockwise) gyre circulation (27 km radius) in front of the Pine Island Ice Shelf has previously been identified in both numerical models and velocity observations. Mooring data further revealed a potential reversal of this gyre during an abnormally cold period. Here we present ship-based observations from 2019 to the west of Thwaites Ice Shelf, revealing another gyre (13 km radius) for the first time in this habitually ice-covered region, rotating in the opposite (anticyclonic, anticlockwise) direction to the gyre near Pine Island Ice Shelf, despite similar wind forcing. We use an idealised configuration of MITgcm, with idealised forcing based on ERA5 climatological wind fields and a range of idealised sea ice conditions typical for the region, to reproduce key features of the observed gyres near Pine Island Ice Shelf and Thwaites Ice Shelf. The model driven solely by wind forcing in the presence of ice can reproduce the horizontal structure and direction of both gyres. We show that the modelled gyre direction depends upon the spatial difference in the ocean surface stress, which can be affected by the applied wind stress curl field, the percentage of wind stress transferred through the ice, and the angle between the wind direction and the sea ice edge. The presence of ice, either it is fast ice/ice shelves blocking the effect of wind or mobile sea ice enhancing the effect of wind, has the potential to reverse the gyre direction relative to ice-free conditions.

3.2 Introduction

Antarctic ice shelves are thinning rapidly due primarily to basal melting, allowing the ice sheets to accelerate and lose mass (e.g. *Pritchard et al.*, 2012) to significantly contribute to the future sea-level rise (e.g. *Bamber et al.*, 2019, *DeConto et al.*, 2021, *Golledge et al.*, 2019). The highest thinning rate has been observed among those ice shelves draining towards the Amundsen Sea (e.g. *Paolo et al.*, 2015, *Rignot et al.*, 2019), where relatively warm modified Circumpolar Deep Water (mCDW) intrudes onto the Amundsen Sea continental shelf via bathymetric troughs, allowing it to come into direct contact with the base of ice shelves (e.g. *Heywood et al.*, 2016, *Rignot et al.*, 2019). The flux of the mCDW entering the ice shelf cavity determines the rate of ice shelf melting (e.g. *Dutrieux et al.*, 2014, *Jacobs et al.*, 2011). Therefore, understanding the local circulation that determines the flow of mCDW and its associated heat transport toward the ice shelves is crucial for a better prediction of ice shelf melting, future sea level and climate.

Models and observations have revealed the presence of a cyclonic gyre in the centre of Pine Island Bay (PIB; hereafter PIB gyre for this gyre). The gyre is well defined between the sea surface and about 700 m depth, in front of Pine Island Ice Shelf (*Heywood et al.*, 2016, *Thurnherr et al.*, 2014). Gyres play an important role in local ocean circulation, distributing heat and enhancing water mass exchange in the Amundsen Sea (*Schodlok et al.*, 2012, *Zheng et al.*, 2021). *Schodlok et al.* (2012) use a high-resolution model to infer that the strength of this small PIB gyre can be the main determinant of heat transport toward the ice shelf and the associated glacial melt rate (*Schodlok et al.*, 2012). *Zheng et al.* (2021), *Mankoff et al.* (2012) and *Tortell* (2012) also suggest that the PIB gyre entrains water as it exits the ice cavity, contributing to the spreading of glacial meltwater and its associated heat, nutrients and freshwater. *Yoon et al.* (2022) further mention that the PIB gyre can modulate heat delivery to Pine Island Ice Shelf.

Despite the importance of gyres near ice shelves, they are poorly observed and modelled as polar oceans are often ice-covered and their bathymetry largely unknown, which limits the regular observations and high-resolution models that resolve small gyres. The formation of the PIB gyre has been attributed to the wind forcing and the meltwater outflow in the southeastern Amundsen Sea (e.g. *Thurnherr et al.*, 2014). Model results from *Heimbach and Losch* (2012) show that the PIB gyre would be weaker by more than two-thirds if wind forcing were absent. From October 2011 to May 2013, moored current meters in PIB revealed a reversal of the ocean current velocity (*Webber et al.*, 2017), potentially indicating a change of PIB gyre direction from cyclonic to anticyclonic. However, the driver of any reversal is still uncertain as the limited available observations do not show a change in the sign of the wind stress curl field or in meltwater outflow locations.

Sea ice may play a role in circulation in polar oceans by regulating the heat and momentum exchange between the ocean and the atmosphere (e.g. *Meneghello et al.*, 2018). *Meneghello et al.* (2018) suggest that the interplay among sea ice, wind and ocean can affect the wind-driven Beaufort Gyre dynamics through the influence of sea ice on dampening ocean surface currents, the so-called ice–ocean stress governor. This mechanism focuses mainly on mobile ice and the processes occurring under ice cover (e.g. *Elvidge et al.*, 2016, *Meneghello et al.*, 2018). Mobile ice may drag the ocean and increase the wind stress field felt by the ocean through sea ice (i.e. ocean surface stress, hereafter OSS), while fixed ice, including fast ice and ice shelves, will reduce or entirely block OSS below ice. Nevertheless, relatively little attention has been paid to fixed ice and processes near the boundary of ice coverage in the context of wind-driven polar gyres.

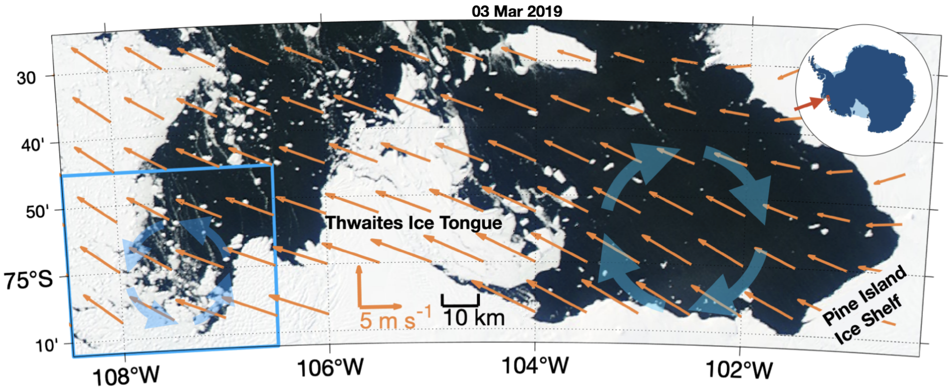

Figure 3.1: **Map of the southeastern Amundsen Sea.** Schematics of Pine Island Bay and Thwaites gyres are shown by thick blue arrows in front of Pine Island Ice Shelf and to the west of Thwaites Ice Tongue, respectively. The ice imagery is from Worldview Aqua/MODIS corrected reflectance (true colour) on 3 March 2019. The climatological 10 m wind velocity from 2009–2019 ERA5 reanalysis (*Hersbach et al.*, 2018) data (0.25° × 0.25° resolution; wind velocity data are interpolated to 0.25° × 0.125° resolution. Only every other arrow in the zonal direction is plotted for clarity) is denoted by orange arrows (see orange scale vectors). The blue box covers the region of Thwaites gyres that is used for Figure 3.2 and 3.4. The inset map shows our study region.

The sparse spatial coverage of observations in these often-ice-covered regions limits our understanding of the mechanisms regulating these gyres, which motivates this study. In Section 3.3, we present a set of new observations of another gyre near Thwaites Ice Shelf (hereafter Thwaites gyre; Figure 3.1). Similar to the PIB gyre, Thwaites gyre is influenced by a climatologically cyclonic wind field (which favours cyclonic gyres); however, it is anticyclonic, raising the intriguing question of what mechanism(s) controls the direction of these gyres. We note the different sea ice coverage over the Thwaites and PIB gyres and hence hypothesise that sea ice can influence the OSS to alter the gyre direction. Considering the sparse observations in the Amundsen Sea, we adopt a new approach to this complex question. In Section 3.4, we introduce an idealised model designed to explore the roles of wind and sea ice in determining the gyre features. Section 3.5 presents the results of the idealised model when different ice conditions and wind stress fields are applied. We discuss the limitations and applications of the results and summarise the results in Section 3.6.

3.3 Observations of gyres in the west of Thwaites Ice Tongue

From 25 February to 4 March 2019, the RV *Nathaniel B. Palmer* collected the first hydrographic dataset to the west of Thwaites Ice Tongue as part of the International Thwaites Glacier Collaboration: Thwaites-Amundsen Regional Survey and Network (ITGC: TARSAN) project. Temperature and salinity profiles were obtained using a Sea-Bird SBE 911C CTD (conductivity, temperature, depth) profiler with two pairs of conductivity and temperature sensors and then vertically averaged into 1 dbar bins. Ocean current velocities over the upper 980m of the water column were obtained using a 75 kHz ocean surveyor (OS75) and a 38 kHz ocean surveyor (OS38) shipboard acoustic Doppler current profiler (sADCP). The amount of good-quality data reduced significantly, if not completely, below a depth depending on the sADCP frequency, rolling of the ship, water turbidity and bubbles passing below the sADCP. During this campaign in the Thwaites gyre region, these depths are 400 m for OS75 and 760 m for OS38. Velocity measurements taken below these depths are removed. All velocity measurements are then horizontally averaged into 2 km × 2 km bins. No de-tiding has been applied to the velocity measurements presented in this study because the moored current meters and models in the region suggest that tidal currents are less than 2 cm s^{-1} (*Jourdain et al.*, 2019), and bathymetry is so poorly known in this region that uncertainties in predicted tidal model currents are of a similar magnitude.

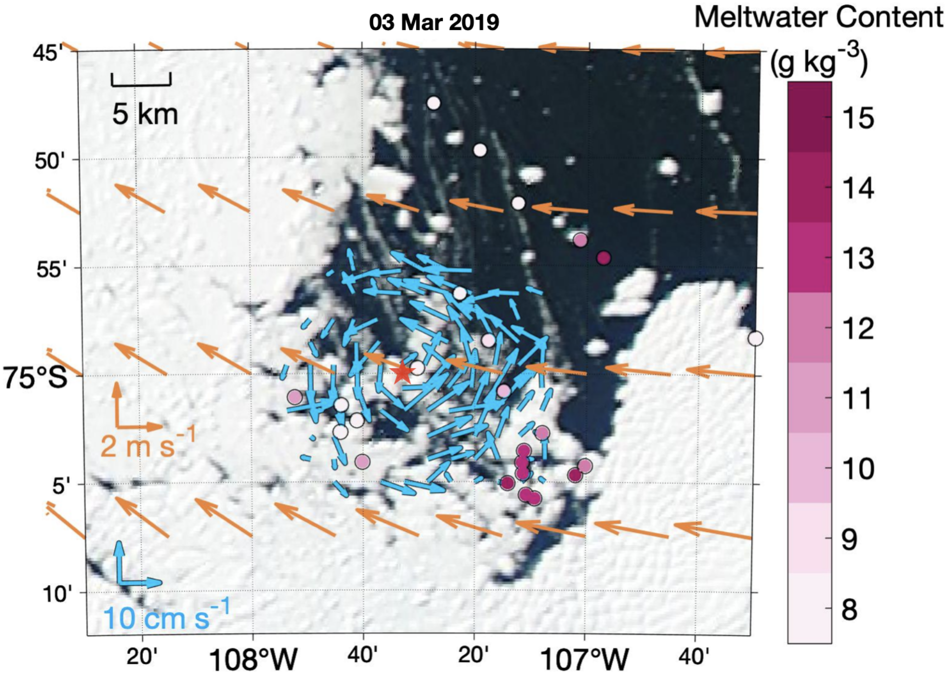

Figure 3.2: **Map of the Thwaites gyre region.** The blue arrows indicate the depth-averaged (30–430 m) current velocity from sADCP measurements (observations are averaged to 2 km × 2 km bins; see blue scale vectors). The red star indicates the gyre centre. The orange arrows indicate the 2009–2019 climatological wind from the ERA5 reanalysis (*Hersbach et al.*, 2018) (0.25°×0.25° resolution; for clarity, velocity data are interpolated to 0.25° × 0.125° resolution; see orange scale vectors). The pink shaded dots show the full-depth-averaged meltwater content calculated from ship-based CTD data (see colour bar).

This region is habitually covered by sea ice year-round and has only opened twice since 2000 (Worldview Aqua/MODIS corrected reflectance). The newly obtained velocity dataset reveals the previously unreported Thwaites gyre (blue arrows in Figure 3.2). Based on the observations, we identify the centre of Thwaites gyre at 75 °S, 107.55 °W. We then calculate the tangential components of ocean current around concentric circles centred on Thwaites gyre and average them into 1 km radius bins (Figure 3.3a). Thwaites gyre has an approximate radius of 13 km and can be well identified in the 30 to 430 m depth range covered by the sADCP (Figure 3.3a), recirculating about 0.2 Sv (i.e. 10^6 m^3 s^{-1}) of water. The ship CTD survey reveals a detectable density gradient across the gyre (Figure 3.3b, c, d). The tangential velocity increases with depth from the near surface to about 130 m, where it reaches its highest speed (about 10 cm s^{-1}, Figure 3.3a) and then decreases with depth to zero at about 620 m. We calculate the average vertical shear of the tangential velocities between 3–7 km from the gyre centre to quantify the baroclinicity of the gyre, defined as the vertical gradient of the tangential velocity between the velocity maximum (130 m) and minimum (620 m). The gyre velocity decreases with depth at a relatively constant rate between these depths. The calculated averaged vertical shear is $2{\times}10^4$ s^{-1}, i.e. a change of 0.1 m s^{-1} over 490 m. Note that Thwaites gyre is anticyclonic, despite the local cyclonic wind stress curl, evident in both the climatology (Figure 3.1) and contemporaneous observations (Figure 3.4), favouring cyclonic gyres.

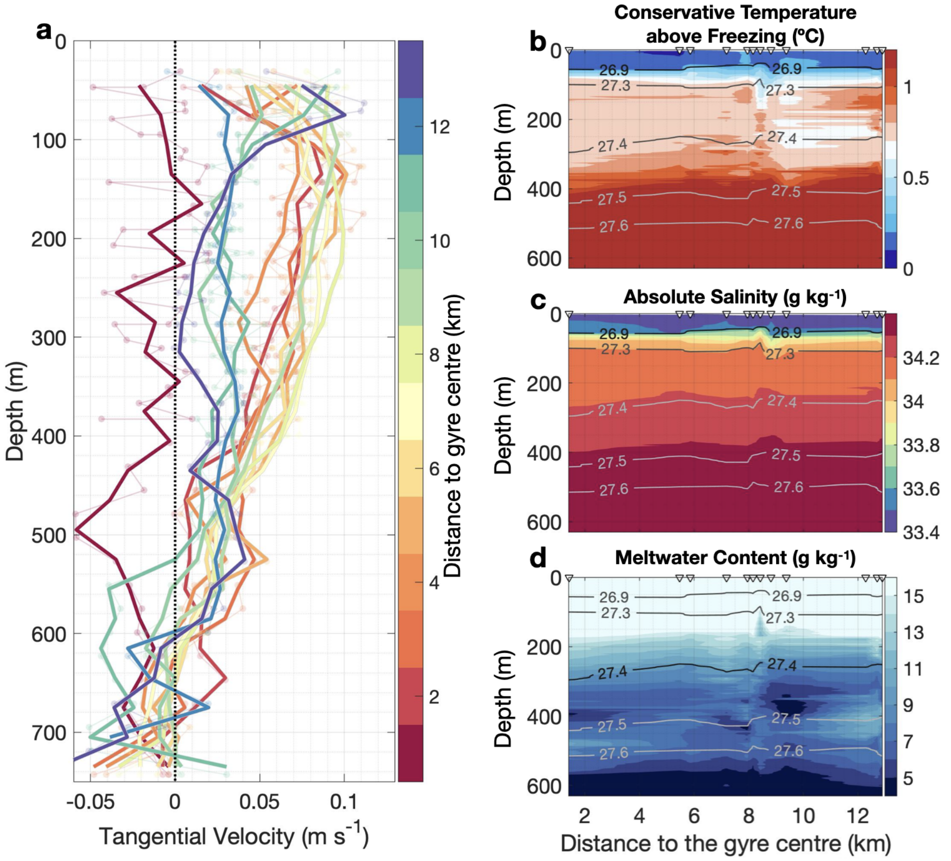

Figure 3.3: **Vertical structure of the Thwaites gyre. a** Tangential velocity of the Thwaites gyre with distance to the gyre centre (colours). All velocity profiles are horizontally averaged into 1 km radius bins (pale dots and lines) and then vertically averaged into 30m bins (thick lines). **b–d** Section plots of CTD measurements collected in the Thwaites gyre region, with distance to the gyre centre. Potential-density isopycnals (in kg m^{-3}) are denoted by grey contours. Positions of profiles are marked as triangles at the top of the panel. Below 650 m, the water column is occupied by modified Circumpolar Deep Water and is very stable so is not presented here. Conservative temperature above freezing is presented in **b**. Absolute salinity is presented in **c**. Meltwater content is presented in **d**.

To identify the role of the gyre in transporting meltwater, and test if meltwater outflow can help to explain the gyre rotation, we calculate meltwater content from temperature and salinity profiles in the gyre region using the composite-tracer method (*Jenkins*, 1999) (Pink dots in Figure 3.2). In this calculation, we use three water masses including mCDW, Winter Water and glacial meltwater, and the two tracers conservative temperature (Θ) and absolute salinity (S_A), defined following the Thermodynamic Equations of Seawater-10 standard (*McDougall and*

Barker, 2011). Both tracers are assumed to be conservative for all observations. We chose the endpoints following previously published research. The endpoints of mCDW ($\Theta = 1.044°\text{C}$ and $S_A = 34.8795$ g kg^{-1}) are consistent with *Wåhlin et al.* (2021), and the endpoints of Winter Water ($\Theta = -1.86°\text{C}$ and $S_A = 34.32$ g kg^{-1}) and glacial meltwater ($\Theta = -90.8°\text{C}$ and $S_A = 0$g kg^{-1}) are the same as used by *Zheng et al.* (2021) and *Biddle et al.* (2019). The fraction of meltwater can be derived from observations with the equation below:

$$\varphi_{meltwater} = \frac{\Theta_{observed} - \Theta_{mCDW} - \frac{(S_{A_{observed}} - S_{A_{mCDW}}) \times (\Theta_{WW} - \Theta_{mCDW})}{(S_{A_{WW}} - S_{A_{mCDW}})}}{\Theta_{meltwater} - \Theta_{mCDW} - \frac{(S_{A_{meltwater}} - S_{A_{mCDW}}) \times (\Theta_{WW} - \Theta_{mCDW})}{(S_{A_{WW}} - S_{A_{mCDW}})}} \tag{3.3.1}$$

where $\varphi_{meltwater}$ is the meltwater fraction and Θ and S_A with subscripts define the conservative temperature and absolute salinity endpoints of each water mass.

The highest meltwater content is detected in the southeast of the Thwaites gyre (Figure 3.2). This is consistent with observations collected by an autonomous underwater vehicle presented in *Wåhlin et al.* (2021) that suggest a north-westward meltwater-rich outflow emanating from the cavity beneath Thwaites Ice Tongue. The Thwaites gyre may entrain this meltwater plume and thus play a role in circulating meltwater near Thwaites Ice Shelf and boost water-mass mixing.

Although a previous study suggests that the buoyancy of glacial meltwater at depth may facilitate gyres (*Mathiot et al.*, 2017), Thwaites gyre is not likely to be meltwater-driven. As glacial meltwater plumes coming out from the base of glacier are more buoyant than the ambient water, they rise and turn left due to Coriolis force, as seen in Pine Island Bay (e.g. *Thurnherr et al.*, 2014, *Zheng et al.*, 2021). Glacial meltwater coming out from Thwaites Ice Tongue to the southwest of the Thwaites gyre will therefore impede the anticyclonic gyre, rather than accelerate it. Hence, neither the cyclonic wind stress curl shown in Figure 3.2 nor the meltwater discharge can directly generate an anticyclonic gyre. Therefore, we explore other factors that might explain this apparent contradiction.

Sea ice coverage is often remarkably different between the PIB and Thwaites gyre regions (Figure 3.1). Satellite imagery shows that the PIB gyre region was generally open during the whole summer of 2009 (Worldview Aqua/MODIS corrected reflectance), when the PIB gyre was firstly observed (*Thurnherr et al.*, 2014). At the same time, fast ice covered most of the Thwaites gyre region, and the sea ice did not open until late January 2019 (Figure 3.4a), about a month before the sADCP survey revealed the gyre (in late February to early March 2019). During February, ice coverage in the Thwaites gyre region changed from covering the western part of the Thwaites gyre (1 February 2019, Figure 3.4b) to completely open (12 February 2019, Figure 3.4c). Sea ice covered the western part of the Thwaites gyre again (23 February 2019, Figure 3.4d) 2 d before the start of the sADCP data collection.

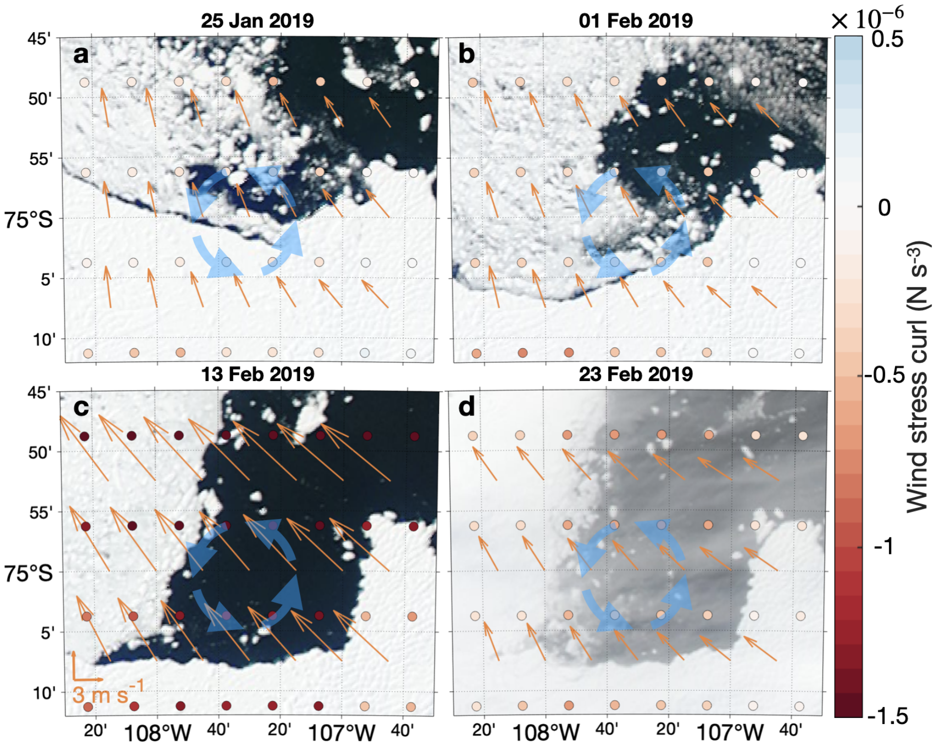

Figure 3.4: **The ice conditions in the Thwaites gyre region.** The orange arrows denote daily-averaged wind speed from the ERA5 reanalysis (*Hersbach et al.*, 2018) (0.25°× 0.25°resolution; for clarity, velocity data are meridionally interpolated to 0.25°× 0.125°resolution). Dots are coloured by the wind stress curl calculated from the interpolated 0.25°× 0.125°resolution daily-averaged wind speed from the ERA5 reanalysis (*Hersbach et al.*, 2018). Thick blue arrows indicate the Thwaites gyre. Ice imagery is from **a** 25 January, **b** 1 February, **c** 13 February and **d** 23 February 2019, respectively, as stated above each panel.

The presence of sea ice alters OSS (e.g. *Elvidge et al.*, 2016, *Meneghello et al.*, 2018). Thus, we hypothesise that the sea ice coverage may mediate the OSS and the resulting surface stress curl felt by the ocean (i.e. ocean surface stress curl, hereafter OSSC) sufficiently to reverse a gyre, leading to the different PIB and Thwaites gyre directions. To test this hypothesis, we use an idealised model to reproduce wind-driven gyres and run a set of conceptual experiments to simulate the response of wind-driven gyres to different sea ice coverages.

3.4 Model experimental design

3.4.1 Model set-up

We employ the MIT general circulation model (MITgcm; Marshall et al., 1997) with an idealised barotropic set-up. The model has an ocean domain with a size of 60 km × 60 km and a horizontal grid spacing of 1 km (Figure 3.5; for comparison, the baroclinic Rossby radius in this region is about 5 km, following the calculation described by *Chelton et al.* (1998)). It has one 1 km thick vertical layer with a free surface. The size of the model domain is comparable to the PIB gyre region. The bottom boundary is free-slip with no drag, and the lateral boundaries are no-slip.We set the Coriolis parameter f to be -1.4083×10^{-4} s^{-1}, appropriate for 75°S, with a meridional gradient β of 1×10^{-11} s^{-1} m^{-1}. The time step is 120 s. The southern boundary is envisaged to be the ice shelf (Figure 3.5).

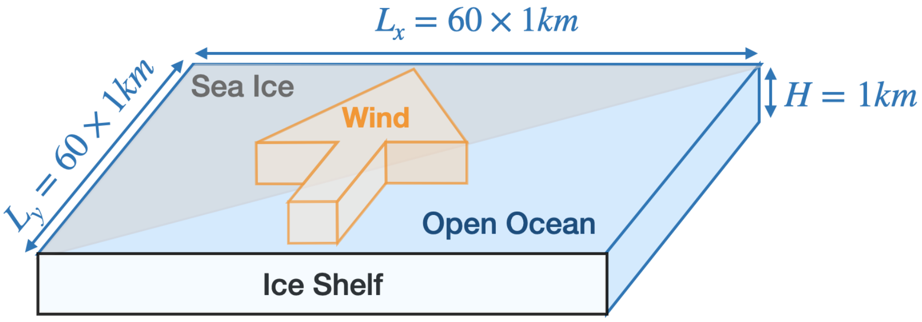

Figure 3.5: **Model schematic.** Sea ice is indicated by the pale grey patch covering the northwestern half of the gyre domain. The orange arrow indicates the wind direction, perpendicular to the ice shelf front.

We run all simulations for 6 model months, which allows all of them to spin up to be sufficiently close to a steady state. The spin-up time of the simulations varies from 51 to 91 d, assessed as the time at which the daily change of the total kinetic energy of the ocean is less than 0.1 % of the total kinetic energy of the ocean at the final model day of the 6 model months.

3.4.2 Wind forcing

The wind field is the only external forcing applied to the model ocean. We generate a simplified wind forcing field (Figure 3.6a) based on the key features of the climatological wind in the southeastern Amundsen Sea to include the ice conditions for both Pine Island Bay and around the Thwaites Ice Tongue (Figure 3.1). The ERA5 climatological 10 m wind (*Hersbach et al.*, 2018) above the PIB and Thwaites gyres blows from the ice shelves to the ocean, with a speed decreasing from the southwest to the northeast. As mentioned in Section 3.4.1, we rotate the domain relative to true north such that these offshore winds are purely meridional in the model, with zero zonal wind (Figure 3.5). The maximum wind speed (10 m s^{-1}) occurs in the southwestern corner of the model domain (Figure 3.6a). The meridional gradient of wind speed (-1.667×10^{-6} s^{-1}) is one-fifth of the zonal gradient of wind speed (-8.333×10^{-6} s^{-1}). The meridional wind stress is given by

$$\tau_y = C_D \rho_{air} |v| v, \tag{3.4.1}$$

where $C_D = 1 \times 10^{-3}$ is the drag coefficient, $\rho_{air} = 1.275$ kg m^{-3} is the air density and v is the wind speed. The wind forcing field applied in our study can be downloaded from the link in the Data availability section.

We vary the strength and sign of the wind stress curl to generate four wind forcing fields: strong or weak and cyclonic or anticyclonic wind stress curl (Figure 3.6a–d). The simplified wind field representing the climatological conditions in the southeastern Amundsen Sea is shown in Figure 3.6a. The same strength of wind stress curl, but anticyclonic, is shown in Figure 3.6c. The two remaining wind fields have wind stress curls weaker by 50 % (Figure 3.6b, d). The average wind speed over the whole ocean model domain is kept the same for all four wind fields.

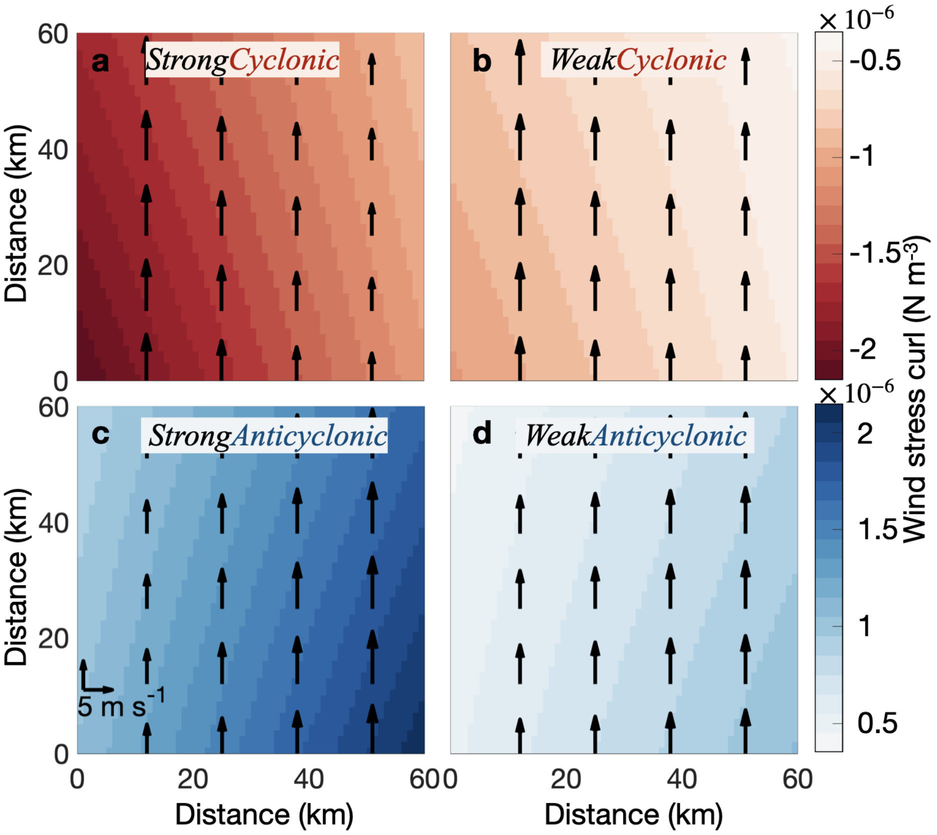

Figure 3.6: **Wind fields applied in this study.** **a** The wind field representing simplified climatological conditions in the southeastern Amundsen Sea. **b** Same as **a**, but with wind stress curl reduced by 50 %. **c** Same as **a**, but anticyclonic. **d** Same as **c**, but with wind stress curl reduced by 50 %. The arrows show wind stress (only every 13th arrow is plotted for clarity), with the scale on the southwestern corner of **c**. Shading shows wind stress curl, red for cyclonic and blue for anticyclonic.

3.4.3 Sea ice coverage

We do not include a sea ice model in our study, but we change the strength of OSS to simulate the influence of sea ice in the ice-covered area. Fast ice and ice shelves are unable to move significantly and so are expected to completely block the wind stress, but other types of ice coverage may have different impacts on the OSS. Previous research has found a generally higher momentum transfer over ice-covered regions than open water due to ice drift dragging the ocean (e.g. *Martin et al.*, 2014, *Meneghello et al.*, 2018). The magnitude of this additional stress on the ocean surface from ice drift may change due to the different types and concentrations of ice coverage. We vary the magnitude of OSS in the ice-covered half of the model domain from 0 % to 200 % of wind stress to sample a range of possible OSS modification by ice in steps of 20 %. For all simulations, OSS remains unaltered in the ice-free half.

In addition, we vary the angle between the sea ice edge and wind direction from $\pi/4$ to $3\pi/4$ (Figure 3.7a) to generate five different ice coverages as shown in Figure 3.7b–f. For all ice coverages applied in this study, the ice covers exactly half the model domain, with the sea ice edges always intersecting the centre of the domain.

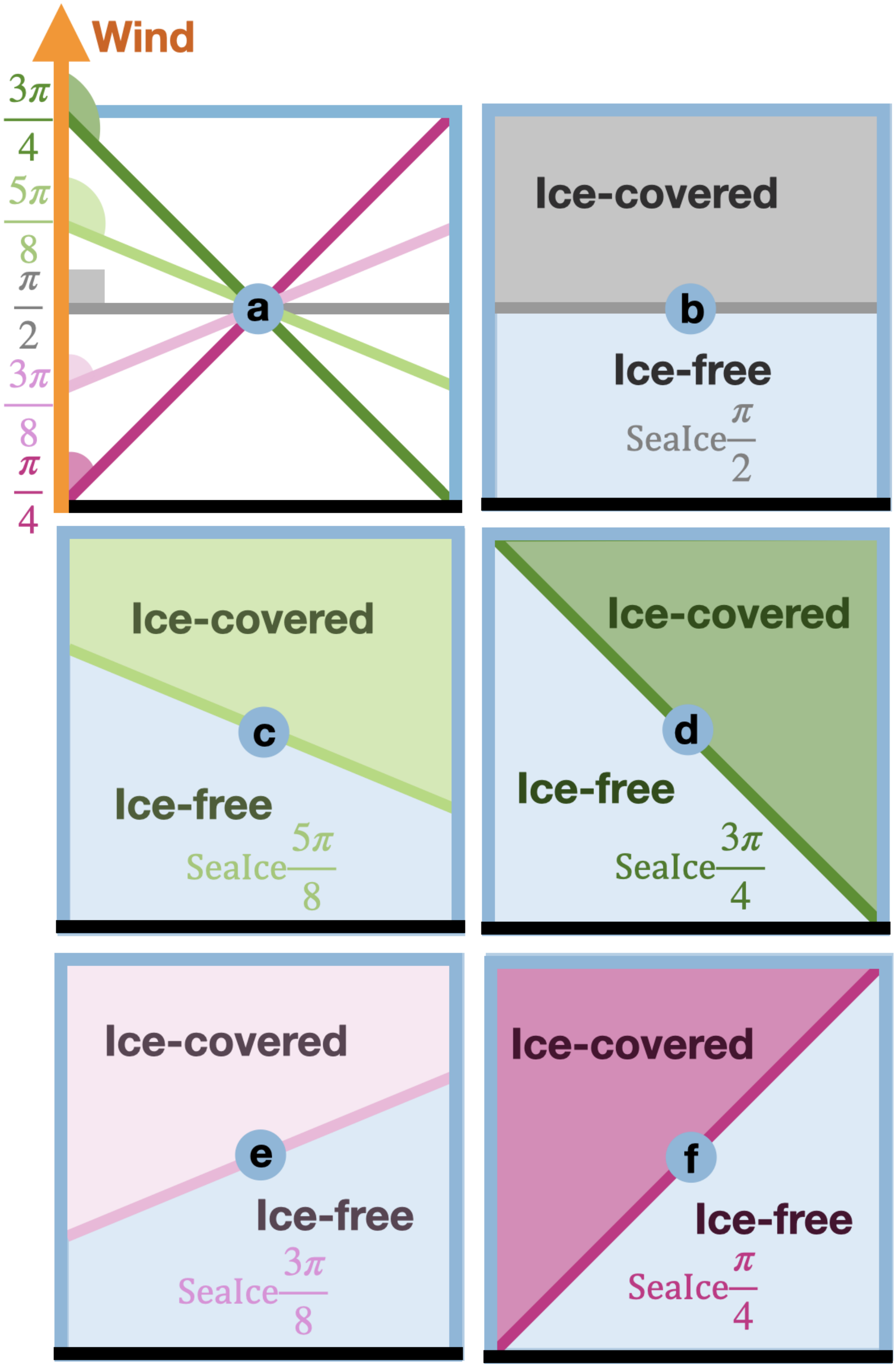
Wind
3π/4
5π/8
π/2
3π/8
π/4
a
b
Ice-covered
Ice-free
SeaIce π/2
c
Ice-covered
Ice-free
SeaIce 5π/8
d
Ice-covered
Ice-free
SeaIce 3π/4
e
Ice-covered
Ice-free
SeaIce 3π/8
f
Ice-covered
Ice-free
SeaIce π/4

Figure 3.7: **Ice coverages applied in this study.** **a** Comparison of all ice coverages. Angles are between the ice edges (thick coloured lines) and wind direction (thick orange line). The thick black line denotes the ice shelf front. **b–f** Schematics of sea ice coverage (shaded patches) and sea ice edge (thick coloured lines), with the same colour scheme as shown in **a**. Ice-free regions are shaded in pale blue.

3.5 Model results

3.5.1 Effect of wind stress on simulated gyres

We first consider results from simulations with no sea ice coverage. Here the strength and direction of gyres solely depend on the wind field. Cyclonic wind stress curl fields (Figure 3.6a, b) generate cyclonic gyres (Figure 3.8a, b), stronger wind stress curl fields (Figure 3.6a, c) generate stronger gyres (Figure 3.8a, c), and vice versa, as expected.

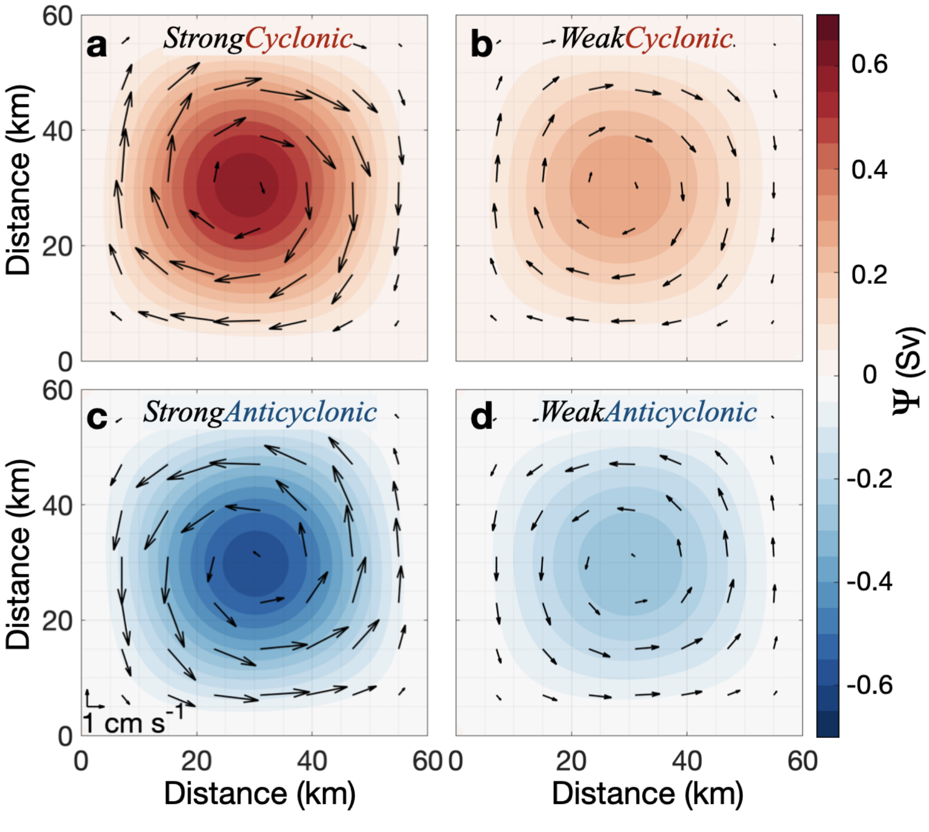

Figure 3.8: **Simulated steady-state gyre streamfunction (Ψ) and current velocity, when sea ice is absent.** Shading indicates streamfunction while arrows indicate current velocity (only every eighth arrow is plotted for clarity). The wind forcing for each of panels **a–d** is shown in Figure 3.6a–d.

For both the StrongCyclonic and StrongAnticyclonic wind fields, the simulated gyres have a maximum streamfunction of 0.58 Sv and a maximum current speed of 3.2 cm s^{-1}. Compared with the PIB gyre surveyed in 2009 (1.5 Sv, 30 cm

s^{-1}, Thurnherr et al., 2014), which is also located in an ice-free area, the simulated gyres are weaker with a slower current speed. The different strength between simulated gyres and PIB gyre might be due to the lack of surface intensification of the currents and the lack of meltwater injection in our barotropic model. Nevertheless, our idealised model captures the characteristics of the gyre sufficiently to be a useful tool to explore the effects of different forcing fields and sea ice coverage on gyre strength, shape and direction.

3.5.2 Effect of sea ice on simulated gyres

3.5.2.1. An example of simulated gyre similar to Thwaites gyre

As an example of the sea ice influencing OSSC, we first discuss the simulation that generates an anticyclonic gyre similar to the observations of the Thwaites gyre discussed in Section 3.3. As mentioned in Section 3.3, in early March 2019, sea ice covered the western part of the Thwaites gyre (Figure 3.2), at an angle to the wind stress similar to the SeaIce$\frac{\pi}{4}$ ice coverage (Figure 3.7f). The ERA5 wind (*Hersbach et al.*, 2018) stress curl was about -5 to -7.5 $\times 10^{-7}$ N m^{-3}, similar to theWeakCyclonic wind field (Figure 3.6d). We therefore consider the WeakCyclonic wind field and the SeaIce$\frac{\pi}{4}$ and 0 % τ ice coverage to mimic (in an idealised way) the response of the ocean to the wind and ice conditions in the Thwaites gyre region in March 2019 (Figure 3.9).

The OSSC is zero over the ice-covered domain (northwestern half of Figure 3.9a) and negative (i.e. cyclonic in the Southern Hemisphere) over the ice-free domain (southeastern half of Figure 3.9a). Due to the different OSS between ice-covered and ice-free domains, positive OSSC (i.e. anticyclonic in the Southern Hemisphere) occurs along the sea ice edge, with a magnitude about 10 times larger than the negative values occurring in the ice-free domain (Figure 3.9a). The magnitude of the OSSC along the sea ice edge decreases from the southwest to the northeast, due to the negative meridional and zonal gradients in wind stress (Figure 3.9a).

This asymmetric positive OSSC along the sea ice edge then results in an asymmetric anticyclonic gyre with its centre located slightly left of the centre of the model domain (Figure 3.9b). The anticyclonic gyre has a maximum Ψ of -0.56 Sv and a maximum current speed of 3.0 cm s^{-1} at steady state. Thwaites gyre in reality has a higher maximum speed (10 cm s^{-1}, Figure 3.3a) but circulates less water (0.2 Sv) than the simulated gyre. This is partly because the thickness of the water column influenced by the Thwaites gyre is only about 400 m, while it is 1000m in our simulation presented here. We tested the same model set-up with a 400m depth and compare the results with the 1000m depth model results. The simulated gyre from the 400m deep model set-up has a faster speed, but the streamfunction and gyre features remain very similar to the gyre from the 1000m depth simulation, e.g. 7.6 cm s^{-1} and 0.58 Sv when sea ice is not present (similar to conditions for the PIB gyre) and 7.1 cm s^{-1} and -0.55 Sv when SeaIce$\frac{\pi}{4}$, 0 % τ and WeakCyclonic are applied (similar to conditions for the Thwaites gyre). Overall, this experiment demonstrates that, even with an idealised barotropic model, the presence of sea ice can enable a cyclonic wind field to generate an anticyclonic gyre, similar to that observed in 2019.

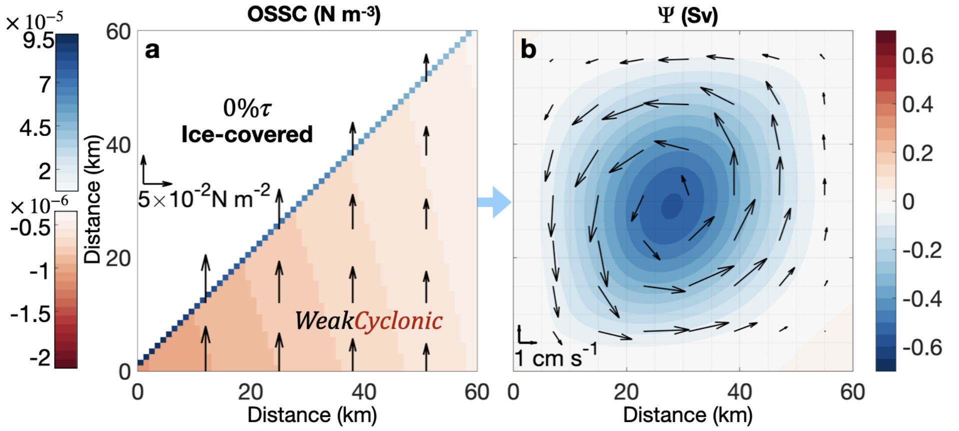

Figure 3.9: **Ocean surface stress curl (OSSC) and simulated gyre streamfunction (Ψ) for simulation with the WeakCyclonic wind field and the SeaIce$\frac{\pi}{4}$ and 0 % τ ice coverage.** **a** Shading indicates OSSC, and arrows indicate wind stress (only every 13th arrow is plotted for clarity). **b** Shading indicates simulated gyre Ψ, and arrows indicate current velocity (only every eighth arrow is plotted for clarity).

3.5.2.2 Overview of the effect of sea ice coverage on simulated gyres

The example discussed above illustrates the influence of a single configuration of ice coverage (SeaIce$\frac{\pi}{4}$, 0 % τ) on the simulated gyre. To make our results more generally applicable, we run our model while varying the ice edge angle and the percentage of wind stress transferred through the sea ice. Figure 3.10 and 3.11 illustrate that wind-driven gyres can reverse despite an unchanged wind field for a range of parameters. Here we use Figure 3.10 and 3.11 to present an overview of the simulated gyre features being affected by both the angle between the wind and sea ice edge, and the amount of stress transferred to the ocean. In the following Section 3.5.2.3 and 3.5.2.4, we discuss the mechanisms underlying these processes in more detail.

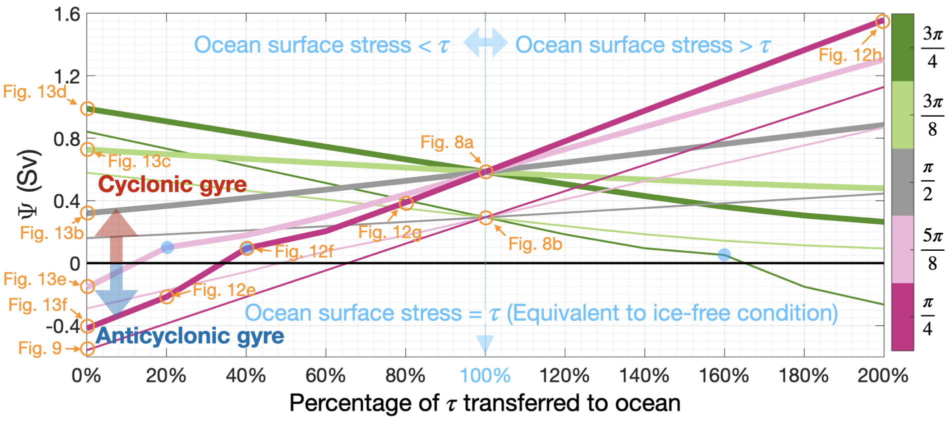

Figure 3.10: **Simulated maximum gyre streamfunction (Ψ) for cyclonic wind stress curl experiments.** Positive streamfunction values are cyclonic and negative values are anticyclonic. The line colours indicate the angle between the wind direction and the sea ice edge, as shown in Figure 3.7. Thick lines denote the simulations with strong wind stress curl (i.e. StrongCyclonic; Figure 3.6a) while thin lines denote the simulations with weak wind stress curl (i.e.WeakCyclonic; Figure 3.6b). Blue dots mark the turning points where the lines of simulated 9 have a discontinuity in gradient caused by the occurrence of dipoles or tripoles. Orange circles with texts mark the simulations shown in Figure 3.8, 3.9, 3.12, 3.13.

We use the ocean model streamfunction to diagnose the strength and direction of the simulated gyre – the maximum magnitude of streamfunction reflects the gyre strength, and its sign reflects gyre direction. Some of our simulations generate two or three connected gyres with different strengths and directions (i.e. dipoles or tripoles). In the analysis we discuss only the gyre with the greatest magnitude of streamfunction (i.e. dominant gyre) in such simulations, unless otherwise stated.

Figure 3.10 shows that strong wind stress curl fields (i.e. StrongCyclonic, thick lines) lead to stronger gyre strength (i.e. higher magnitude of streamfunction) than those from weak wind stress curl fields (i.e. WeakCyclonic, thin lines). Note that Figure 3.10 only contains the simulations with cyclonic wind fields (i.e. StrongCyclonic andWeakCyclonic). Results from simulations with anticyclonic wind fields (i.e. StrongAnticyclonic and WeakAnticyclonic) are mirror images of those from simulations with cyclonic wind fields about the 0 Sv line.

For all simulations, the simulated gyre transport is always quasi-linearly related to the percentage of stress transferred through the ice to the ocean (Figure 3.10). For cyclonic forcing with the increase in the percentage of wind stress felt by the ocean, if the angle between the sea ice edge and wind direction is less than $\frac{\pi}{2}$ (i.e. sea ice in the top left, denoted by dark and pale pink lines in Figure 3.10), the simulated Ψ increases monotonically, i.e. enhances the cyclonic gyre and opposes the anticyclonic gyre. In contrast, if the angle between the sea ice edge and wind direction is greater than $\frac{\pi}{2}$ (i.e. sea ice in the top right, denoted by dark and pale green lines in Figure 3.10), the simulated Ψ decreases monotonically, i.e. enhances the anticyclonic gyre and opposes the cyclonic gyre.

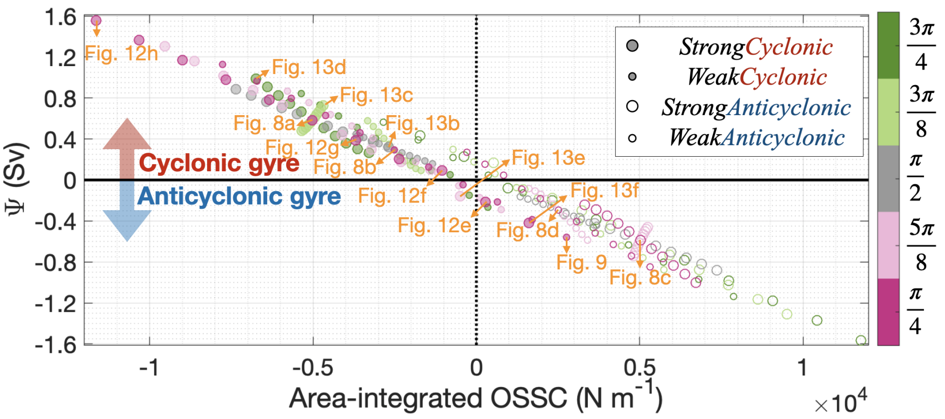

Figure 3.11: **Simulated maximum streamfunction (Ψ) changes with area-integrated OSSC over model domain.** There are 11 filled or open circles for each combination of different sizes and colours, indicating simulations with 11 percentages of wind stress transferred to the ocean. Positive streamfunctions are cyclonic (in the Southern Hemisphere) and negative streamfunctions are anticyclonic (in the Southern Hemisphere), while the opposite is true for OSSC. The colours of circles indicate the angle between sea ice edge and ice shelf front, as shown in Figure 3.7. Filled circles denote the simulations with cyclonic wind stress curl forcings while open circles denote the simulations with anticyclonic wind stress curl forcings. Large circles denote the simulations with strong wind stress curl forcings while small circles denote the simulations with weak wind stress curl forcings. Orange circles with texts mark the simulations shown in Figure 3.8, 3.9, 3.12, 3.13.

The lines of the simulated streamfunction sometimes have a discontinuity in gradient (blue dots in Figure 3.10). Those turning points occur when the model simulates a dipole of two gyres, or a tripole of three gyres, as mentioned in this Section. We discuss examples of this in more detail in the following Section

3.5.2.3 and Figure 3.12e, f. At the turning points indicated in Figure 3.10, the weaker gyre(s) of the dipole or tripole do follow the quasi-linear relationship, but the dominant gyre (which is captured as blue dots in Figure 3.10) does not.

We use Figure 3.11 to illustrate how the change in area-integrated OSSC depends on the angle between the wind direction and the ice edge. It is well-established that the strength of gyres is closely related to the OSSC integrated over the wind-influenced area (*Stommel*, 1948). In agreement with this, we find that negative area-integrated OSSCs tend to generate cyclonic gyres while positive area-integrated OSSCs tend to generate anticyclonic gyres (Figure 3.11). The simulated maximum streamfunction and the area-integrated OSSC are approximately linearly correlated (Figure 3.11), such that stronger OSSC leads to stronger gyres. Although this relationship is very strong, demonstrating the dominant influence of the magnitude of the area-integrated OSSC, the location and distribution of the OSSC do have a secondary influence that accounts for deviations from a perfect correlation.

Because the imposed zonal gradient of wind stress is greater than the meridional gradient in our experiments, the difference between the OSS of ice-covered and ice-free domains is greater when the ice edges are more meridional. Hence, the integrated OSSC along ice edges that are more meridional is higher than along those that are more zonal. Therefore, SeaIce$\frac{3\pi}{4}$ and SeaIce$\frac{\pi}{4}$ (Figure 3.7f, d) can lead to a higher area-integrated OSSC along the ice edge than SeaIce$\frac{5\pi}{8}$ and SeaIce$\frac{3\pi}{8}$ (Figure 3.7c, e). Accordingly, the streamfunction responds more sensitively to the percentage of wind stress transferred to the ocean when orientation of the ice edge is more meridional (i.e. diagonal ice edge, denoted by dark pink and dark green lines in Figure 3.10).

3.5.2.3. Effect of the percentage of τ transferred to the ocean

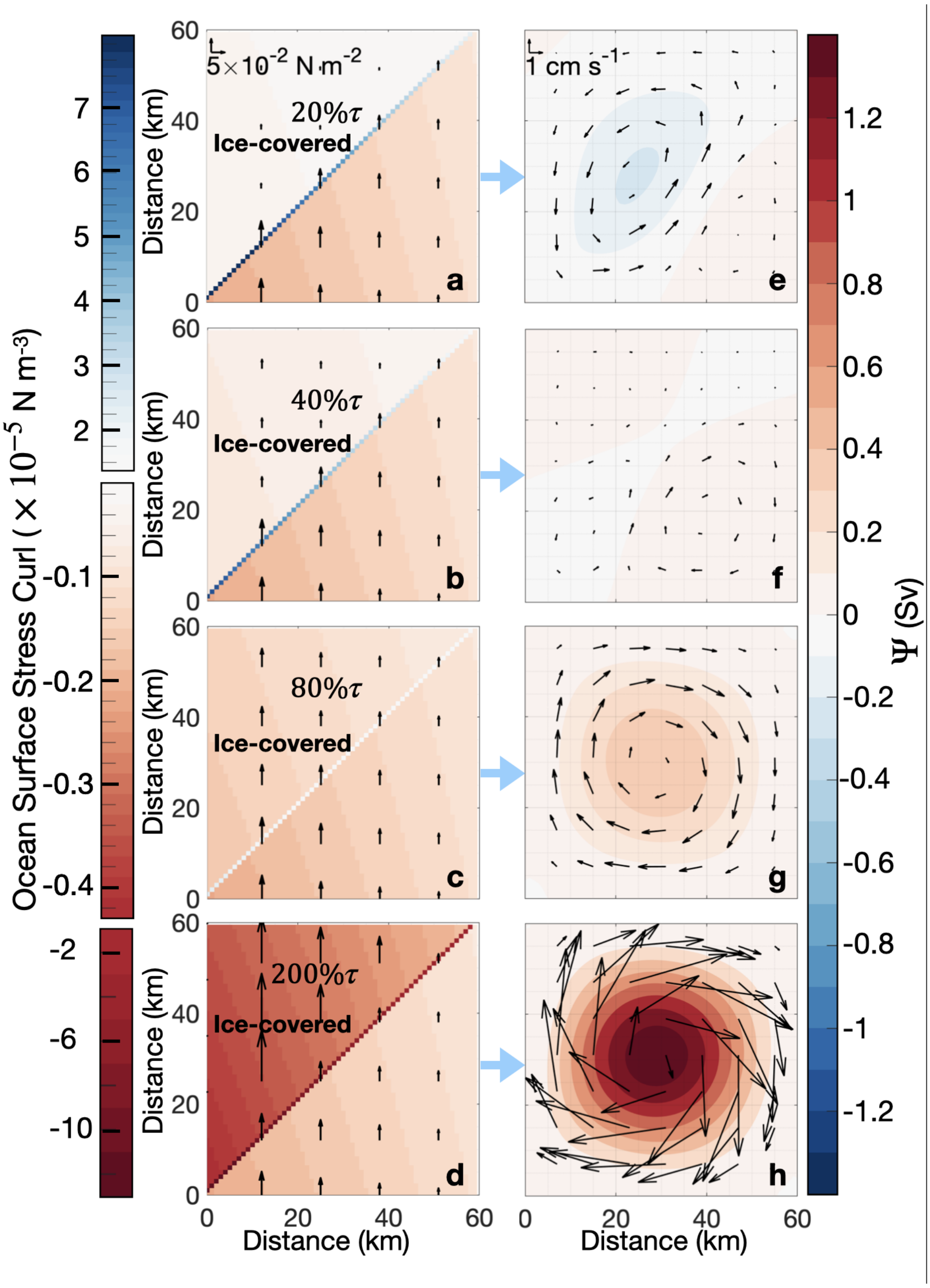

Figure 3.12: **a**–**d** Ocean surface stress (arrows; only every 13th arrow is plotted for clarity) and ocean surface stress curl (shading) for **a** 20 % τ; **b** 40 % τ; **c** 80 % $\tau$and **d** 200 % τ transferred to the ocean. Sea ice covers the northwestern half of the gyre domain (i.e. SeaIce$\frac{\pi}{4}$)$andtheStrongCyclonicwindfieldisapplied.$**e** $-$ $-$**h**$Simulatedstreamfunction$(Ψ; shading) and ocean current velocity (arrows; only every eighth arrow is plotted for clarity) resulting from the forcing in panels **a**–**d** respectively.

Applying the StrongCyclonic wind field and SeaIce 4 ice coverage, we gradually change the percentage of wind stress transferred to the ocean (% τ) to isolate its influence on the gyre features. The spatial distribution of the OSSC and the circulation pattern are shown in Figure 3.12.

As in the 0 % τ simulation discussed in Section 3.5.2.1 and 3.5.2.2, the 20 % τ simulation has negative OSSC over the entire model domain except along the sea ice edge where it has positive OSSC (Figure 3.12a). However, the OSS over the ice-covered domain is higher in the 20 % τ simulation (Figure 3.12a) than in the 0 % τ simulation (Figure 3.10), which reduces the difference in OSS between ice-covered and ice-free regions, resulting in a decrease in the positive OSSC along the sea ice edge. Therefore, the 20 % τ simulation generates an anticyclonic gyre centred in the model domain (Figure 3.12e), in the same location as the 0 % τ simulation (Figure 3.10b) but slightly weaker. In addition, a second very weak cyclonic gyre is generated in the ice-free domain (southeastern corner in Figure 3.12e).

Likewise, for the 40 % τ simulation the decreased OSS over the ice-covered domain leads to a decreased magnitude of positive OSSC along the sea ice edge (Figure 3.12b). The anticyclonic gyre found in the 20 % τ simulation almost vanishes in the 40 % τ simulation, and only a very weak and small anticyclonic gyre is identified in the southwest corner of Figure 3.12f. In the ice-free domain, the very weak cyclonic gyre previously found in 20 % τ becomes stronger (southeastern corner in Figure 3.12f). A weaker cyclonic gyre is also formed in the ice-covered domain (northwestern corner in Figure 3.12f), generating a tripole. As mentioned above in Section 3.5.2.2, this simulation shows an example of one of the turning points in Figure 3.10.

In the 80 % τ simulation, the OSS in the ice-covered domain is only 20 % τ smaller than that felt in the ice-free domain, making the OSSC along the sea ice edge very weak (Figure 3.12c). The anticyclonic gyre found in the previous simulations near the ice edge has now completely vanished, so the other two weak cyclonic gyres identified in Figure 3.12g have merged into a single, stronger cyclonic gyre dominating the whole gyre domain (Figure 3.12g), similar to the equivalent ice-free simulation (Figure 3.8b).

Finally, the 200 % τ simulation has negative OSSC all over the domain (Figure 3.12d), forming a very strong cyclonic gyre (Figure 3.12h). Despite the asymmetry of the forcing, with the strongest OSSC in the northwest sector and along the diagonal, the gyre is nearly symmetric and centred on the middle of the domain. As discussed previously (Figure 3.10 and 3.11), between 80 % τ and 200 % τ there is a steady increase in the cyclonic gyre strength.

Overall, changing the percentage of the wind stress transferred through ice to the ocean in this configuration has a dramatic impact on the gyre. With increasing transfer of wind stress through the ice, the simulated gyre starts from anticyclonic rotation when there is no transfer, develops to dipole and tripole, and finally reverses to cyclonic. This demonstrates that the percentage of wind stress transferred through sea ice to the ocean alone can regulate the gyre strength, and even change the gyre direction.

3.5.2.4. Effect of the angle between the wind and sea ice edge

Now we consider how the gyre responds to changing the angle of the sea ice edge when the wind field is StrongCyclonic and sea ice completely blocks the wind (i.e. 0 % τ). In these experiments, the OSSC over the ice-covered domain is zero, and the OSSC over the ice-free domain is always negative. The OSSC along the sea ice edge is the same sign as over the ice-free domain (cyclonic) when the angle between wind and sea ice edge is greater than $\frac{\pi}{2}$ but the opposite sign (anticyclonic) when the direction between wind and sea ice edge is less than $\frac{\pi}{2}$. When the angle is exactly $\frac{\pi}{2}$ there is zero OSSC along the sea ice edge, resulting in a cyclonic gyre forced by cyclonic OSSC in the ice-free domain (Figure 3.13b). Both SeaIce$\frac{5\pi}{8}$ and SeaIce$\frac{3\pi}{4}$ generate cyclonic gyres (Figure 3.13c, d), as the OSSC is cyclonic over the whole model domain. For both SeaIce$\frac{3\pi}{8}$ and SeaIce$\frac{\pi}{4}$, the area-integrated OSSC is anticyclonic (Figure 3.11), demonstrating that the anticyclonic OSSC along the ice edge dominates relative to the cyclonic OSSC over the ice-covered domain in these simulations. Anticyclonic gyres are thus generated in both SeaIce$\frac{3\pi}{8}$ and SeaIce$\frac{\pi}{4}$ (Figure 3.13e, f). As discussed in Section 3.5.2.2, simulations with more "meridional" ice edges (i.e. SeaIce$\frac{3\pi}{4}$ and SeaIce$\frac{\pi}{4}$) have greater impacts on the OSSC and so generate stronger gyres (Figure 3.13d, f). Overall, these experiments demonstrate how the ice edge orientation relative to the wind forcing can determine the gyre strength and direction.

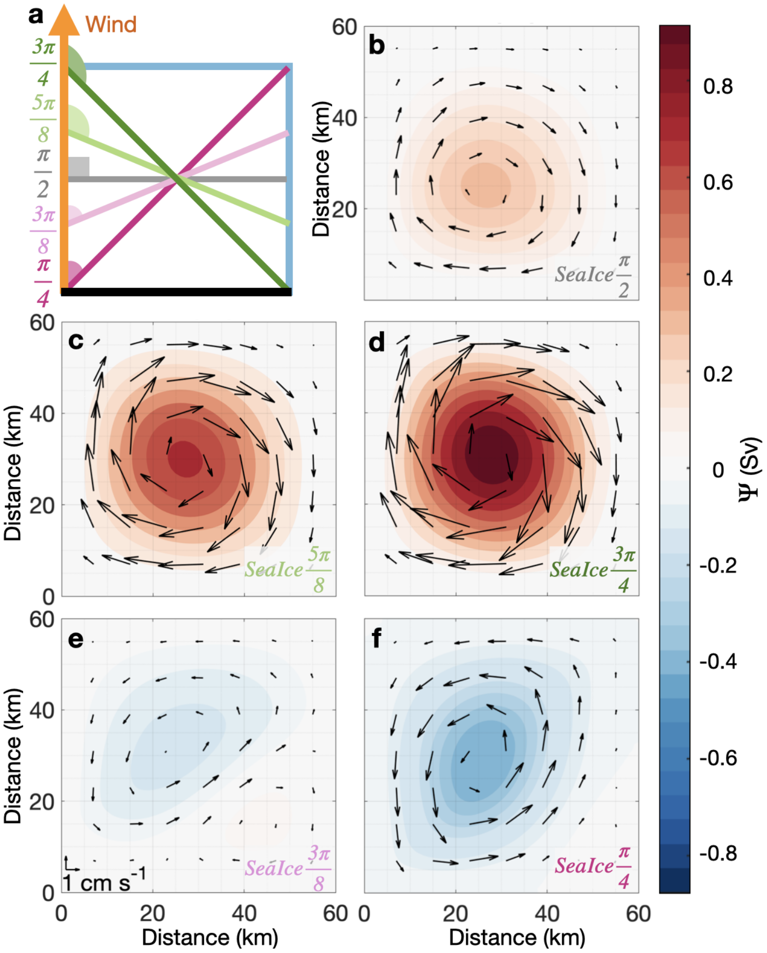

Figure 3.13: **Simulated gyre streamfunction (Ψ) when wind field is StrongCyclonic and sea ice completely blocks the wind (i.e. 0 % τ).** Arrows indicate the current speed (only every eighth arrow is plotted for clarity). Sea ice coverage information for panels **b–f** is shown in Figure 3.7b–f.

3.5.2.5. Fast ice combined with mobile ice

As described in Section 3.5.2.1, the simulation with wind field and ice conditions similar to those experienced in the Thwaites gyre region in March 2019 (WeakCyclonic wind field, SeaIce$\frac{\pi}{4}$ and 0 % τ ice condition, Figure 3.9a) generates an anticyclonic gyre (Figure 3.9b) similar to the ADCP observations (Figure 3.2). Here we explore a very different ice configuration that may also generate an anticyclonic gyre and is similar to sea ice conditions observed in the Thwaites gyre region in previous seasons (negative streamfunction; lines falling below the 0 Sv horizontal black line in Figure 3.10).

Suppose that the southwestern half of the domain is covered in fast ice transferring 0 % of τ to the ocean, and the northeastern half of the domain is covered in mobile sea ice transferring 200 % of τ to the ocean, as shown in Figure 3.14a. The steady-state solution for this scenario is an anticyclonic gyre centred near the middle of the model domain (Figure 3.14b). Due to the strong OSSC along the sea ice edge (Figure 3.14a), this anticyclonic gyre is stronger (-1.11 Sv) than all gyres simulated from the original model set-up (Figure 3.10).

This scenario is reminiscent of the sea ice conditions in late January 2019 (Figure 3.4a), when fast ice covered the southern part of the Thwaites gyre region while loose sea ice covered the northern part of the Thwaites gyre region. Hence, the sea ice coverage that occurred in January 2019 might generate or facilitate the Thwaites gyre observed in March. To generate gyres, all that is required is a spatial difference in the amount of wind stress transferred to the ocean, whether that is through fast ice blocking the effect of the wind or mobile ice enhancing the effect of the wind.

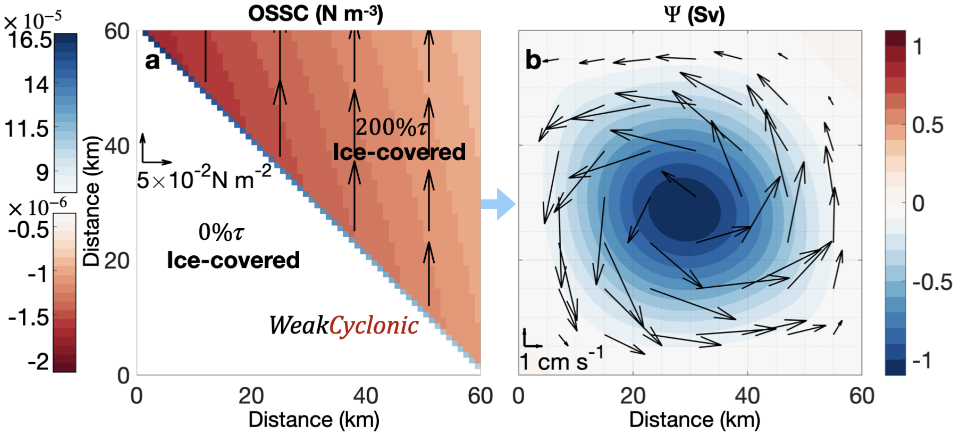

Figure 3.14: **Ocean surface stress curl (OSSC) and simulated gyre streamfunction (Ψ) for the simulation with the WeakCyclonic wind field.** Sea ice covers the whole model domain. Sea ice in the northeast has 200 % of τ transferred to the ocean (representing mobile ice) while sea ice in the southwest has 0 % of τ transferred to the ocean (representing fast ice). **a** The shading indicates the OSSC and the arrows indicate the wind stress. **b** The shading indicates the simulated gyre Ψ and the arrows indicate the current velocity.

3.6 Discussion

Regional circulation models have often been used to study ocean gyres (e.g. *Meneghello et al.*, 2021, *Regan et al.*, 2020). However, to comprehensively explore the impact of the ice coverage on the gyre formation through its modification of the stress imparted to the ocean, we need to isolate the individual forcings and conduct a very large number of experiments to examine how they interact. We therefore invoke an idealised model that represents the surface forcing in a simple manner, excluding other features of the real ocean such as baroclinicity, ice-shelf processes and topography. Some biases may occur due to the lack of those mechanisms. For example, the meltwater injection that is thought to facilitate gyres (*Mathiot et al.*, 2017) is not included, which may explain the differences in the magnitude of Ψ between the simulated gyres (0.58 Sv for PIB and -0.42 Sv for Thwaites) and gyre observations (about 1.5 Sv for PIB, *Thurnherr et al.* (2014), and -0.27 Sv for Thwaites). Our argument is not to dispute the effect of meltwater, but rather to highlight the role of wind forcing and the sea ice conditions.

Since our model has much lower computational costs than other regional models, we can run our model hundreds of times to test the gyre response in different wind-ice combinations and apply the results in different polar oceans under varying conditions. All of our simulated gyres reached steady state within 2 months and respond to changed surface conditions on a similar timescale. We also tested a 1.5-layer reduced-gravity model as a comparison for the barotropic case presented here, with all forcings and model design remaining the same. Although the baroclinic model produced gyres with more intensified surface currents and a slightly longer spin-up time, the gyres in baroclinic and barotropic model cases have the same direction and similar sizes and transports. To explore the sensitivity of the model results to the width of this marginal ice zone, we created two new ice conditions with the smaller gradients (not shown) in surface stress and weaker OSSC over three grid points (3 km) and four grid points (4 km). The simulated gyres have almost the same strengths (both about -0.41 Sv) and same shapes as the simulated gyre from simulations without a wider marginal ice zone. This indicates that the width of the marginal ice zone is not important for gyre generation. Hence, our model reproduces the observed gyre direction and response to ice coverage well.

The influence of mobile ice on changing OSS has been well studied (e.g. *Meneghello et al.*, 2018) while little progress has been made towards fixed ice. We have considered both the increase and decrease in OSS, which included scenarios caused by both mobile ice and fixed ice altering OSS. Nonetheless, we acknowledge that, while in this study we assume that the ocean has no motion below the fixed ice so fixed ice will lead to zero OSS, in cases where the ocean current speed is non-zero, there exists a relative speed between the ocean and the fixed ice, hence resulting in a non-zero OSS beneath the fixed ice as well. On the other hand, when the mobile ice is drifting at the same speed and direction as the surface currents, there is no relative motion between the mobile ice and the ocean, leading to zero OSS. We recommend that in individual cases, careful consideration should be given to the relative speed between sea ice and the ocean to ascertain whether the ice has experienced an increase or decrease in OSS. We further discussed the significant effects of the associated OSSC along the ice boundary on gyre formation and gyre features. Our results are especially useful in Antarctic continental shelf seas where climatological winds often blow offshore from the ice shelves/fast ice to the ocean, which allows the gyres near fixed ice to fully develop.

In Antarctic continental shelf seas, gyres near ice shelves contribute significantly to the spreading of glacial meltwater and its associated heat and nutrients (*Mankoff et al.*, 2012, *Zheng et al.*, 2021). Meltwater can impede sea ice formation, causing polynyas, or alter the locations and timing of hotspots of marine productivity (*Mankoff et al.*, 2012, *Mathis et al.*, 2007, *Zheng et al.*, 2021). Gyres may transport heat, which is carried by warm water entrained into the gyre, towards ice shelf cavities (*Schodlok et al.*, 2012). The existence of gyres can cause isopycnal displacement. For cyclonic gyres, isopycnals shoal in the gyre centre, as regularly observed in Pine Island Bay (e.g. *Dutrieux et al.*, 2014, *Heywood et al.*, 2016, *Thurnherr et al.*, 2014, *Zheng et al.*, 2021); for anticyclonic gyres, isopycnals deepen in the gyre centre. Below warm-cavity ice shelves, the water is stratified with a fresh meltwater-rich upper layer and a warm yet salty mCDW lower layer. This isopycnal displacement may allow warmer mCDW to enter the ice cavity and melt ice shelves (*Yoon et al.*, 2022). The intrusion of warm water into the base of warm-cavity ice shelves is via the dense lower layer, the so-called "salt wedge" (*Robel et al.*, 2022). The water mass exchanges due to gyres may impact the stratification in front of the ice shelve and hence affect this salt wedge and the related intrusions of warm water to ice shelves. Similarly, gyres formed near the sea ice edge can circulate ambient water masses. The redistribution of water masses and the heat and freshwater might feed back onto sea ice formation to affect the ice formation and regeneration of ice cover in the next winter. By changing both the ocean stratification and the sea ice cover, gyres will affect heat fluxes in the vicinity of ice shelves, which may in turn influence the heat available for basal melting (e.g. *St-Laurent et al.*, 2015, *Webber et al.*, 2017). Therefore, it is important to understand the conditions that can generate or modify such gyres.

Due to the importance of gyres for the regional ocean environment, more observations and simulations are required to better understand the relationship between surface conditions and gyre strength and direction. We highlight the importance of wind-ice-ocean interactions, especially the wind stress curl at the ice edge, to polar ocean gyres. These interactions occur at small scales (of the order of tens of kilometres) that will be poorly resolved by global coupled models. Simulating these processes is also dependent on accurate sea ice conditions including the representation of fast ice and polynyas. Atmospheric models also show that the sea ice concentration, as well as the geometry of sea ice edge and the sharpness of the marginal ice zone, have a substantial impact on the development and evolution of the atmospheric boundary-layer structure, wind velocity, clouds and the air-sea exchanges (*Liu et al.*, 2006, *Spensberger & Spengler*, 2021). These findings further suggest that improved sea ice monitoring is important for getting a comprehensive understanding of the complex interactions the polar regions. Gyres in typically ice-covered regions (such as Thwaites gyre) present extreme challenges for repeat ship-based surveys. We show that the sea ice coverage can change rapidly (Figure 3.4) and has a large influence on the ocean surface stress (Figure 3.10 – 3.13); however, it is yet difficult to monitor. The PIB gyre changes its location interannually and seasonally (*Heywood et al.*, 2016, *Zheng et al.*, 2021), further demonstrating the need for long-term continuous monitoring. Such continuous gyre observations would also be useful for model evaluation and could be obtained with high-resolution sea ice motion from satellites, which can clearly show the surface current through sea ice movement. We urge that further effort is needed for improving the quality of sea ice satellite products, especially the data coverage, operating frequency and spatial resolution. Future work should also include quantifying the effect of different types of sea ice on enhancing or reducing the ocean surface stress, which may be made by the combination of ice-tethered profilers providing under-ice current velocity and autonomous surface vehicles providing the near-surface wind speed and heat fluxes.

Despite the important role that gyres play, small wind-driven gyres have received limited attention in the Antarctic continental shelf seas. There are a few other gyres documented in the Antarctic continental shelf seas, such as the Prydz Bay Gyre (*Smith et al.*, 1984), and the cyclonic gyre in front of Filchner Ice Shelf (*Foldvik et al.*, 1985), but none of them are primarily driven by local wind, so they are not discussed here. Model representations of ocean currents show the existence of some small gyres with a radius of about 15 – 30 km, including PIB gyre, in Antarctic continental shelf seas (e.g. Figure 4c, d in *Nakayama et al.*, 2019). However, except for the PIB gyre, which has been observed in several different years, little attention has been paid to such gyres and their formation mechanisms. This is partly because polar observations often cover either too short a time period or too small an area to provide in situ verification for the gyres found in models. Our study provides a possible mechanism to explain the formation of the gyres formed near the ice-ocean boundary that might be explored for other small gyres shown in high-resolution ocean model results in Antarctic continental shelf seas.

3.7 Conclusion

This study uses new observations to identify the Thwaites gyre for the first time, located in a habitually ice-covered region of the southeastern Amundsen Sea. This gyre rotates anticyclonically, despite the climatological cyclonic wind forcing that implies the gyre should rotate cyclonically, as is the case for the only other gyre reported in the eastern Amundsen Sea, PIB gyre (e.g. *Heywood et al.*, 2016, *Thurnherr et al.*, 2014). To investigate this apparent discrepancy, we use a barotropic model with idealised sea ice and wind forcing only to simulate gyres similar to those observed in the vicinity of ice shelves. Our model suggests that sea ice plays a key role in mediating the wind stress transferred to the ocean and hence determines the direction and strength of the gyre rotation. The percentage of wind stress transferred to the ocean, and the angle between the wind direction and sea ice edge, can alter the OSSC over ice-covered regions and along sea ice edges sufficiently to reverse gyres. Although the simulated gyres are slower than those observed, we demonstrate the potential of sea ice to control gyre direction and intensity. We suggest that these processes may explain gyre formation and reversal in polar oceans, for example, the PIB gyre reversal hypothesised by *Webber et al.* (2017). We further suggest that this wind-ice-ocean interaction may contribute to the development of gyre features throughout the polar oceans.

3.8 Data availability

Processed SADCP data are freely available at `https://doi.org/10.5281/zenodo.6757570` (*Zheng et al.*, 2022b) and CTD data are freely available at `https://doi.org/10.5285/e338af5d-8622-05de-e053-6c86abc0648` (*Queste and Wåhlin*, 2022).

3.9 Code availability

Model code and code for generating wind forcings used in this study are freely available at `https://doi.org/10.5281/zenodo.6757626` (*Zheng et al.*, 2022c).

4

Intense upper-ocean cooling and salinification in the Amundsen Sea Polynya in austral autumn

4.1 Abstract

The Amundsen Sea mixed layer is vital for the local climate system as it determines the exchange of properties and energy between the ocean and atmosphere. However, its processes are poorly understood, as they are controlled by complex interactions between the ocean, sea ice, and atmosphere, yet largely under-sampled, especially in non-summer seasons. Here we present a two-month, high vertical resolution, full-depth hydrographic dataset at the eastern side of the Amundsen Sea Polynya in austral autumn (mid-February to mid-April 2014) collected by a recovered seal tag. This novel data set quantifies the changes in upper ocean temperature and salinity stratification in a previously unobserved season. Our seal-tag measurements reveal that the Amundsen Sea Polynya mixed layer experiences intense cooling, deepening, and salinification. A mixed layer salt budget suggests a sea ice formation rate of 3 cm per day. We use a 1-D mixed layer model to quantify how different forcings affect mixed-layer evolution and how sea ice coverage influences the cooling, salinification and deepening of the mixed layer. The results show that buoyancy forcing dominates over wind forcing, and a sea-ice-reduced heat loss to the atmosphere will lead to

a much warmer, fresher and shallower mixed layer. We therefore speculate that sea ice coverage will cause a large regional difference in mixed-layer features.

4.2 Introduction

The Amundsen Sea Polynya (ASP) is located on the western side of Bear Ridge (Figure 4.1), where the water depth can be as shallow as 250 m (RTOPO, not shown). When icebergs calving in Pine Island Bay drift to Bear Ridge, some of them are trapped and grounded in this shallow region, increasing the iceberg density (*Mazur et al.*, 2017). The high density of icebergs along Bear Ridge forms a "barrier" that stops the sea ice from being transported by the winds northwestwards in autumn/winter (Figure 4.1) (*Bett et al.*, 2020, *St-Laurent et al.*, 2017), resulting in the formation of the ASP.

The water column in the ASP generally consists of three water masses. The modified Circumpolar Deep Water (mCDW), which has the highest temperature (about 0.6 °C) and lies below about 400 m (*Jacobs et al.*, 2012, *Randall-Goodwin et al.*, 2015, *Yang et al.*, 2022). Above the mCDW, it lies the Winter Water, which formed in winter by the wind stirring and surface cooling. Winter Water is at the freezing point and is fresher than mCDW. Antarctic Surface Water, which is essentially WW that has been modified in summer, has a temperature much warmer than Winter Water due to solar warming, and a salinity much lower than Winter Water due to sea ice melt and glacial surface runoff. Except for these three water masses, glacial meltwater spreads at a level where it reaches a neutral density, but it mixes widely to all levels in stratified water (*Naveira Garabato et al.*, 2017) and has been observed throughout the top $\sim$ 450 m (*Randall-Goodwin et al.*, 2015).

The ASP is the most productive polynya in coastal Antarctica (*Arrigo and van Dijken*, 2003) and plays an important role in the local ecosystem and carbon sink (*Arrigo et al.*, 2008a). A large portion of the Southern Ocean is occupied by high nutrient, low chlorophyll water (*Arrigo et al.*, 2008b). However, the ASP has an average chlorophyll concentration that reaches 7 mg m^-3 at its peak phytoplankton bloom (January), which is about two or three times higher than any other polynyas in Antarctica (*Arrigo et al.*, 2012). The high productivity of the ASP has been attributed to the iron supply from the glacial meltwater (e.g. *Coale et al.*, 2005) and the sediment-rich modified Circumpolar Deep Water (below $\sim$ 450 m) in the Amundsen Sea (e.g. *Poulton and Raiswell*, 2005). The Amundsen Sea is surrounded by the most rapidly melting glaciers in the world (e.g. *Rignot et al.*, 2019), including Thwaites Glacier and Pine Island Glacier, leading to a high supply of meltwater and associated nutrients to the euphotic zone of the ASP.

However, *Naveira Garabato et al.* (2017) suggest that summertime solar radiation generates a seasonal pycnocline that enhances the lateral mixing of glacial meltwater, instead of diapycnal mixing, which allows meltwater to be entrained into the euphotic zone. After summer, the solar radiation weakens and the intensities of the wind stirring and the surface cooling increase, resulting in a weakly stratified upper ocean. Winter observations reveal that an upper ocean with a weak stratification and high density allows more meltwater to rise to the near-surface in the Amundsen Sea (*Zheng et al.*, 2021). ASP features a deep winter mixed layer (*Randall-Goodwin et al.*, 2015), partially due to eddies (e.g. *St-Laurent et al.*, 2019) and/or tides (e.g. *Robertson*, 2013). Hence, ASP meltwater is more likely to reach the near surface in winter than in summer. The deep winter mixed layer might play an important role transporting the meltwater to the euphotic zone of the ASP, contributing to the ASP's high production. Nonetheless, although the ASP has been repeatedly sampled in different years (e.g. *Randall-Goodwin et al.*, 2015), these observations are biased toward summertime processes, leaving the non-summer season largely overlooked. The lack of observations in the Amundsen Sea have severly limited our understanding of the transition of the upper ocean from summer to winter in the ASP.

Upper ocean processes in polynyas are complex. In non-summer seasons, the dominant control of the buoyancy budget in sea-ice regions is brine rejection, while in the open ocean, it is the heat loss through air-sea heat flux (*Pellichero et al.*, 2017). However, in polynyas, sea ice is constantly formed and producing brine locally, yet is constantly transported away from the formation site by winds and surface currents, and does not substantially affect the heat loss from the ocean to the atmosphere. Both the salt gain from sea ice formation and the heat loss from the ocean to the atmosphere, cause an intense buoyancy loss and induce vertical convection. Both ice-tethered profilers and autonomous surface vehicles (e.g. *Zhao et al.*, 2014) have shown their potential in monitoring upper-ocean processes in polynyas, but their measurements often lack continuity vertically (i.e. only a few levels in a water column) and/or temporally (i.e. only a few snapshots in each mission). Although moorings have been deployed near the Dotson Ice Shelf and their hydrographic measurements investigated (*Yang et al.*, 2022), to avoid the icebergs, they do not have sensors above 200 m, so are not able to resolve the upper-ocean polynya processes. The deployment of seal tags largely increases the amount of non-summer-season observations and allows us to study the transition from summer to winter (e.g. *Biddle et al.*, 2017, *Meredith et al.*, 2011). However, we cannot choose where seals go so that we rarely obtain time series from seal tags.

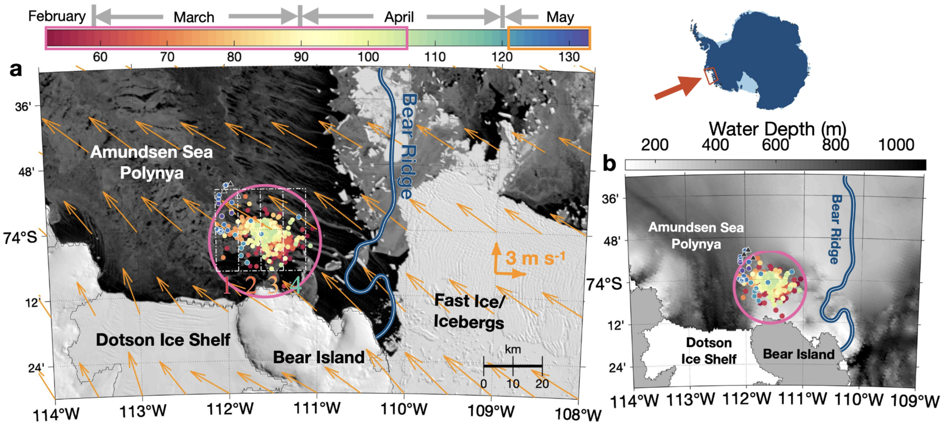
February
March
April
May
60
70
80
90
100
110
120
130
a
36'
48'
74°S
12'
24'
Amundsen Sea Polynya
Bear Ridge
Fast Ice/ Icebergs
Dotson Ice Shelf
Bear Island
3 m s-1
1 2 3 4
km
0 10 20
114°W
113°W
112°W
111°W
110°W
109°W
108°W
Water Depth (m)
200 400 600 800 1000
b
Amundsen Sea Polynya
Bear Ridge
Dotson Ice Shelf
Bear Island
114°W 113°W 112°W 111°W 110°W 109°W

Figure 4.1: **Map of the southeastern Amundsen Sea. a.** Ice photography (MODIS Terra on 14 March 2014) overlaid by locations of *EM959* seal tag profiles, coloured by year day of data collection. Profiles used to analyse temporal variation in Figs. 4 and 5 are indicated by solid dots encircled by the pink circle in the map, with their data-collection year day marked by pink rectangle in the colour bar. Dots with white edges indicate supplementary profiles collected from 1-13 May 2014 (from MEOP), with their data-collection year day marked by the orange rectangle in the colour bar. Black triangles with white edges indicate the profiles collected on 1 September 2014 (from MEOP). The curvy white-blue line is the schematic of the shape of Bear Ridge (modified from *Bett et al.* (2020)). The orange arrows show the averaged wind speed and direction during the *EM959* measuring period. The dashed white box marks the four ERA5 gridpoints we use to area-average the ERA5 reanalysis. **b.** Same as **a**, but for the bathymetry. Location of the study region in Antarctica is shown in the inset.

4.3 Data and Method

4.3.1 Hydrographic observations from the southeastern Amundsen Sea Polynya

4.3.1.1 High-resolution profiles from a recovered seal tag, *EM959*

Seal tags typically include a small Conductivity-Temperature-Depth (CTD) sensor recording in-situ measurements every second. In the Antarctic, they are usually deployed on seal species that tend to dive to the sea bed to feed (e.g. Southern Elephant seals or Weddell seals). Seals typically ascend nearly vertically after feeding, so seal tags will record one upward profile from every dive. However, to reduce data transmission and to extend the battery life of the tag, different algorithms are applied to select a range of about eighteen depths in the deepest dives in every 4-6 hours. Only the measurements from those selected depths and dives are transmitted to the data centre via the Argos satellite system (*Boehme et al.*, 2009, *Fedak et al.*, 2002, 2004, *Photopoulou et al.*, 2015). The one-second resolution time series are stored on the tag but not usually recovered, since tags fall off during the seals' spring/summer moult. In 2014, *EM959* only transmitted 89 profiles via the Argos satellite system, with 18 depths in each profile. However, from the recovered tag, 513 profiles with up to 2079 depths per profile were obtained. This fortuitous tag recovery provides an unprecedented dataset revealing the ocean conditions at extremely high vertical and temporal resolution including the rarely observed near-surface polar winter ocean.

EM959 was initially deployed on the Edwards Islands in Pine Island Bay (*Heywood et al.*, 2014). The instrumented seal then moved west along the edge of the fast ice and grounded icebergs. This seal stayed in the southeastern corner of the ASP from mid-February to late-April, before returning to the land (Figure 4.1). Thus, *EM959* measured the upper-ocean properties of the ASP continually for nearly two months during austral autumn.

We calibrate *EM959* data against proximal (i.e. observations obtained by seals were collected within less than 10 km and less than 5 days from CTD casts, in total 7 profiles) ship-based CTD profiles obtained on the same iSTAR/Ocean2Ice cruise in the Amundsen Sea in February 2014 (*Heywood et al.*, 2016). A median conductivity scaling factor of 1.0018 is applied to all seal profiles (Figure 4.2). We chose only profiles with temperature $>$ 0 °C and not in pycnocline (depth $>$ 800, as pycnoclines moves up and down due to eddies frequently here). For all data used in this study, we follow the Thermodynamic Equations of Seawater-10 standard (*McDougall and Barker*, 2011). Outliers are removed from the seal tag hydrographic profiles following visual inspection. All seal tag profiles discussed in this paper are at their full resolution (i.e. not binned spatially or temporally) unless otherwise stated.

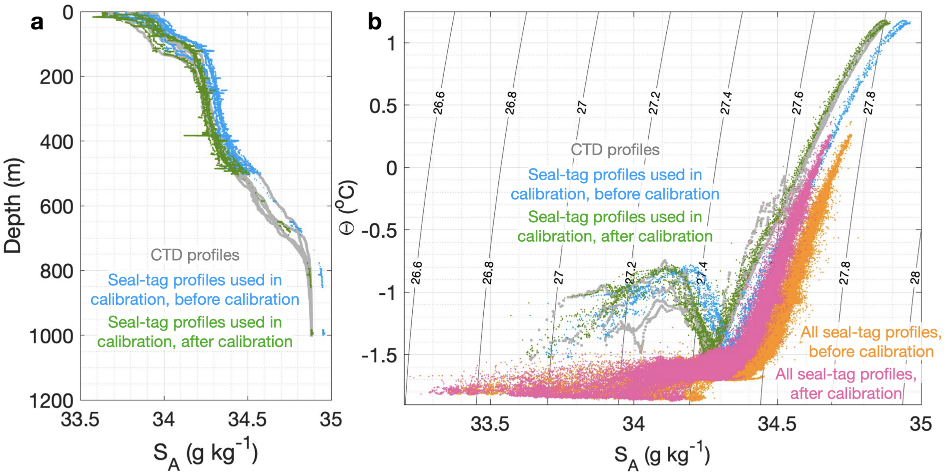

Figure 4.2: **The overview of calibration. a.** The salinity profiles from EM959 and CTD used for calibration. b. Temperature-salinity diagram showing the EM959 and CTD profiles used for calibration.

In the following analysis, we only consider profiles collected when the instrumented seal lingered at the southeastern corner of ASP (dots within the pink circle in Figure 4.1). The median distance from the locations of profiles to the centre of our data collection region (centre of the pink circle in Figure 4.1; 74.017 °S, 111.569 °W) is 5.2 km. For reference, the Rossby radius here is about 5 km, following the calculation described by*Chelton et al.* (1998). Here we assume that the upper ocean is spatially uniform within this relatively small region, and the spatial variation is negligible in our dataset. The dataset collected is thus equivalent to a virtual mooring (*Meredith et al.*, 2011).

4.3.1.2 Data collected from other sea tags in the same year

To extend the temporal coverage of the EM959 dataset, we include 25 profiles from the same general location, but later in the same year, from three further seal tags deployed during the same field campaign (Figure 4.1. 1, dots and triangles with white edges). 22 profiles of them were obtained on 01-13 May 2014 (by a Southern Elephant Seal, *Mirounga leonina* and a Weddell Seal, *Leptonychotes weddellii*) and other 3 profiles were obtained on 01 September 2014 (by another Southern Elephant Seal), and were later processed by Marine

Mammals Exploring the Oceans Pole to Pole (*Roquet et al.*, 2013, 2014) (`http://www.meop.net`; MEOP). All MEOP profiles we use have measurements of salinity and temperature at eighteen depths. The depths include near-surface (2 dbar), temperature minimum (WW core), deep (> 100m) temperature maximum (mCDW core) and the maximum depth reached at the dive, plus fourteen other depths equally spaced between the sea surface and the maximum depth.

4.3.2 Estimation of the accumulated sea ice formation from observations

We make two thickness estimates of accumulated sea ice formation by considering the top-200-m salt and heat budgets separately and independently. *EM959* profiles used in both estimations are vertically averaged into 2-m bins. Profiles that have more than 5 absent bins (either because the dives are too shallow and do not reach 200 m, or because they do not have available measurements near surface) are omitted. Single absent bins are filled by linear interpolation, or extrapolation of the uppermost value to the surface.

Both the salt and heat budget estimations are made within the top 200 m. This depth range covers the observed mixed layer, which is influenced by surface processes. Warm water that sometimes rises from deeper water through upwelling or horizontal advection from the deeper region has little effect above 200 m. Our observations below this depth do not show any clear trend, indicating that the air-sea-ice interactions does not cause a significant temporal variation below this depth.

4.3.2.1 Sea ice formation calculated from salt budget

Here we assume that brine rejection caused by sea ice formation is the only significant process affecting the upper 200 m salt content, neglecting evaporation, precipitation, lateral advection and vertical mixing/exchange between the top 200 m and deeper layers. Following *Charrassin et al.* (2008), the salt budget is described as,

$$\rho_o V_o S_{A_o} = \rho_f V_f S_{A_f} + \rho_{ice} V_{ice} S_{A_{ice}}, \tag{4.3.1}$$

where ρ is the *in-situ* density, V is the volume and S_A is the absolute salinity, with the subscript "*o*" for the original water properties, "*f*" for the final water properties, and "*ice*" for sea ice properties. Sea ice properties are assumed constant and chosen to be $S_{A_{ice}} = 7$ g kg^{-1} (*Biddle et al.*, 2019) and $\rho_{ice} = 920$ kg m^{-3} (*Martin and Kauffmann*, 1981). Given that this calculation is performed for a fixed depth, the total volume does not change, so $V_f = V_o - V_{ice}$. By substituting $V_f = V_o - V_{ice}$ into Equation4.3.1, we can obtain the accumulated sea ice formation as,

$$V_{ice} = \frac{V_o(S_{A_f}\rho_f - S_{A_o}\rho_o)}{S_{A_f}\rho_f - S_{A_{ice}}\rho_{ice}}. \tag{4.3.2}$$

4.3.2.2 Sea ice formation rate calculated from heat budget

OHC_{200m} is calculated using the following equation,

$$OHC_{200m} = \int_{z=200m}^{z=0m} C_p \rho_z (\Theta_z - \Theta_{freezing}) dz, \tag{4.3.3}$$

where $C_p = 4000$J kg^{-1} °C^{-1} is the heat capacity of seawater, ρ_z and Θ_z are the *in situ* water density and conservative temperature of the water at depth z, and the $\Theta_{freezing}$ is the *in situ* freezing point calculated using *in situ* salinity with the TEOS-10 toolbox. We use the heat content above freezing for plotting and comparison with previous studies, but since we use the rate of change of heat content in the budget calculation we would expect the same results using the total heat content.

We assume that all heat loss from the ocean to the atmosphere is either used to cool the upper ocean, or used to form sea ice (i.e. neglecting lateral advection and vertical exchange between the upper and deep ocean). This assumption gives the relationship between the rate of change of the top-200-m ocean heat content OHC_{200m}, hereafter $Q_{OHC_{200m}}$, and the heat flux used in sea ice formation $Q_{IceFormation}$

$$Q_{IceFormation} = Q_{net} - Q_{OHC_{200m}}. \tag{4.3.4}$$

Q_{net} is the net heat flux is given by,

$$Q_{net} = -(Q_{longwave} + Q_{sensible} + Q_{latent}) + Q_{shortwave}, \tag{4.3.5}$$

where $Q_{longwave}$ is the net longwave radiative flux. As upward longwave radiation is sensitive to sea surface temperature, we calculate $Q_{longwave}$ with modelled sea surface temperature at each time step using the equation below,

$$Q_{longwave} = \epsilon_{longwave}\sigma \times (SST + 273.15)^4 - \epsilon_{longwave}Q^{downwards}_{longwave}. \tag{4.3.6}$$

$\sigma = 5.67 \times 10^{-8}$ is the Stefan Boltzmann constant, SST is the modelled sea surface temperature, $\epsilon_{longwave} = 0.97$ is the longwave emissivity of water (the absorptivity is assumed to have the same value), and $Q^{downwards}_{longwave}$ is the downward longwave heat flux from ERA5. $Q_{shortwave}$ is defined positive downwards while other terms are defined as positive upwards. The sea surface temperature used in this estimation is the average temperature of the top 3 m in *EM959* measurements. Q_{latent} is the latent heat flux given by

$$Q_{latent} = (\rho_{air}L_vC_d)U_{10}(q_{sat} - q), \tag{4.3.7}$$

where $\rho_{air} = 1.275$ kg m^{-3} is the air density, $L_v = 2.501 \times 10^6$ J kg^{-1} is the latent heat of vaporisation, $C_d = 1 \times 10^{-3}$ is the drag cofficient between the ocean and atmosphere. U_{10} and q are the 10-m wind speed and the humidity we extract from ERA5, and q_{sat} is the saturation humidity calculated from

$$q_{sat} = \frac{\epsilon_r e_w}{P_{atm} - (0.378 e_w)}, \tag{4.3.8}$$

with the ratio of molecular weight of water rand dry air $\epsilon_r = 0.662$ and the saturated vapour partial pressure $e_w = 6.11e^{\frac{17.62SST}{243.12+SST}} \times 100$ (WMO, 1996; *Gill*, 1982). $Q_{sensible}$ is the sensible heat flux given by

$$Q_{sensible} = \rho_{air} C_{air} C_d U_{10}(SST - T_{2m}), \tag{4.3.9}$$

where $C_{air} = 1005$ J kg^{-1} °C^{-1} is the heat capacity of dry air and T_{2m} is the 2 m air temperature from ERA5.

Hence, we calculate the time series of $Q_{IceFormation}$, which is used to calculate the volume of the formed sea ice following,

$$\frac{dV_{ice}}{dt} = \frac{Q_{IceFormation}}{L_f \rho_{ice}}, \tag{4.3.10}$$

where $L_f = 3.55 \times 10^5$ J kg^{-1} is the latent heat of fusion and t is the time.

The accumulated sea ice formation is then derived, using the time integral of $\frac{dV_{ice}}{dt}$. The integral is calculated over every three hours.

4.3.3 Sea ice condition in the Amundsen Sea

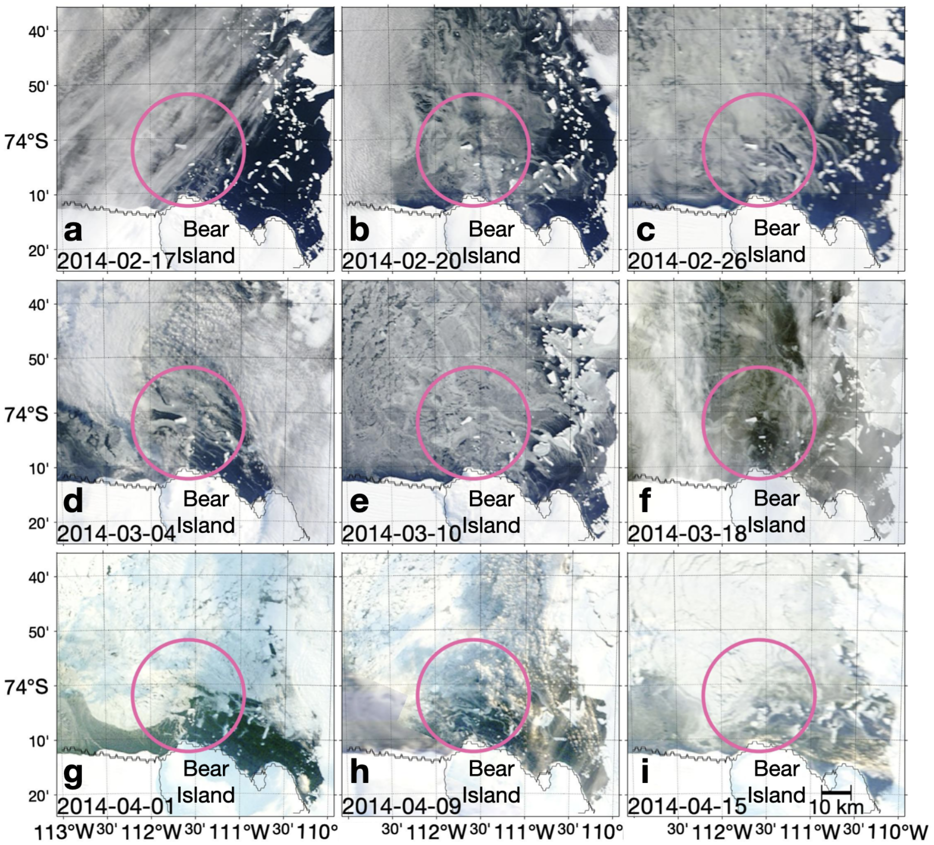
40'
50'
74°S
10'
20'
a
Bear Island
2014-02-17
b
Bear Island
2014-02-20
c
Bear Island
2014-02-26
d
Bear Island
2014-03-04
e
Bear Island
2014-03-10
f
Bear Island
2014-03-18
g
Bear Island
2014-04-01
h
Bear Island
2014-04-09
i
Bear Island
2014-04-15
10 km
113°W 30' 112°W 30' 111°W 30' 110°
30' 112°W 30' 111°W 30' 110°
30' 112°W 30' 111°W 30' 110°W

Figure 4.3: **Examples of the MODIS Terra visible images.** To best represent the sea ice condition in each month, we only use satellite images with minimum cloud covers. Pink circles indicate the *EM959* observational site. Dates when ice imageries were taken are shown in the bottom left of each panel. Scale of the map is shown in panel **i**.

We assess the sea ice condition using Terra MODIS (Moderate Resolution Imaging Spectroradiometer) visible images (Figure 4.3). The images present in Figure 4.3 have a resolution of 250 m per pixel. The dark grey streaks (more likely to be ice) interwoven with streaks of black filaments (more likely to be ocean) to west of fast ice/icebergs in Figure 4.1 and Figure 4.3 are streaks of frazil ice (*Wadhams et al.*, 2018). Due to frequent storms in the study site that might create similar streaky features in the brightness temperature images from satellites, we are unable to use brightness temperature to assist the sea ice identification. We acknowledge that there are sometimes difficulties distinguishing clouds and ice, however, the available satellite images suggest that our study region is mainly open or covered by frazil ice for the most of time during the *EM959* measuring period.

4.3.4 One-dimensional mixed layer model

4.3.4.1 Model description

We use a modified version of the Price-Weller-Pinkel model (PWP; *Price et al.*, 1986). We use the code adapted by *Lazarevich and Stoermer* (2001) to include vertical diffusion (*Lazarevich et al.*, 2004) and subsequently developed by *Biddle et al.* (2017) by adding a sea ice module and a turbulent kinetic energy parameterisation.

To provide the initial conditions for the model, we average all profiles of temperature and salinity collected by *EM959* in the first three days of the measuring period (year day 51-53) and run a vertical running-mean filter with a 5-m window to avoid any density inversion. For consistency with the model code, the initial hydrographic profiles follow EOS-80 (UNESCO, 1983) standard, but model outputs are then converted to TEOS-10 (*McDougall and Barker*, 2011) for plotting figures and comparison with observations.

The model is set up with 609 vertical layers with a constant thickness of 1 m. We run all simulations with a 1-min time step for 54 model days, covering the whole *EM959* measuring period. The model outputs are stored every three hours.

4.3.4.2 Modification of the sea ice concentration in the model

Following *Biddle et al.* (2017), we assume that the presence of sea ice can reduce the air-sea heat flux in the model domain by the same percentage as the sea ice concentration. As described by *Biddle et al.* (2017), the model forms sea ice when the mixed layer has a temperature lower than the surface freezing point. The heat required to warm the mixed layer back to the freezing point is converted to sea ice formation using the latent heat of freezing. As the model is 1-D, sea ice is assumed to accumulate at the same location, melting and refreezing when the mixed-layer temperature changes (i.e., the model does not account for sea ice transport).

We introduce a pseudo sea ice concentration (hereafter *pSIC*) that will reduce the air-sea heat and freshwater fluxes, as done by *Biddle et al.* (2017), by the same percentage of the *pSIC*. Unlike the model of *Biddle et al.* (2017), *pSIC* is a constant, independent of the modelled sea-ice formation processes as the sea ice formed is assumed to be blown away instantaneously in a constant rate. The *pSIC* does not affect the brine rejection and heat release induced by sea ice formation, but only the air-sea fluxes. We run model experiments in which we set *pSIC* to be from 0% to 100% in steps of 25%.

4.3.5 Atmosphere reanalyses from ERA5

We use three-hourly ERA5 reanalysis time series (*Hersbach et al.*, 2020), including 2-m air temperature, 10-m wind stress, downward longwave radiation, downward shortwave radiation, precipitation (Figure 4.4a-d) and specific humidity (not shown) to force our model and to estimate air-sea fluxes. The reanalysis meteorological variables are area-averaged over four ERA5 gridpoints centred along 74°S, at 111.25°W, 111.5°W, 111.75°W and 112°W (i.e. covering 111.125°W to 112.125°W and 73.875°S to 74.125°S, white boxes in Figure 4.1), covering about 852 km^2, over the most of *EM959* observational site. For reference, the ERA5 reanalysis is produced using a spectral model with approximately 31 km resolution and provided on a 0.25° spatial grid (*Hersbach et al.*, 2020), so the grids we choose include the most representative region of the *EM959* observational site. We acknowledge the potential for biased values in the ERA5 reanalyses near the fast ice east of Bear Island, as certain grid cells from the open-ocean region may be mistakenly identified as ice-covered, leading to different surface characteristics. In order to assess the inclusion of these "ice-covered grids," we conducted model simulations using ERA5 reanalysis data from each of the four mentioned ERA5 grid points separately. The model results revealed maximum differences in the top-200-meter heat content were negligible

(Figure 4.4e), i.e., there was not sensitivity to the exact choice of grid point.

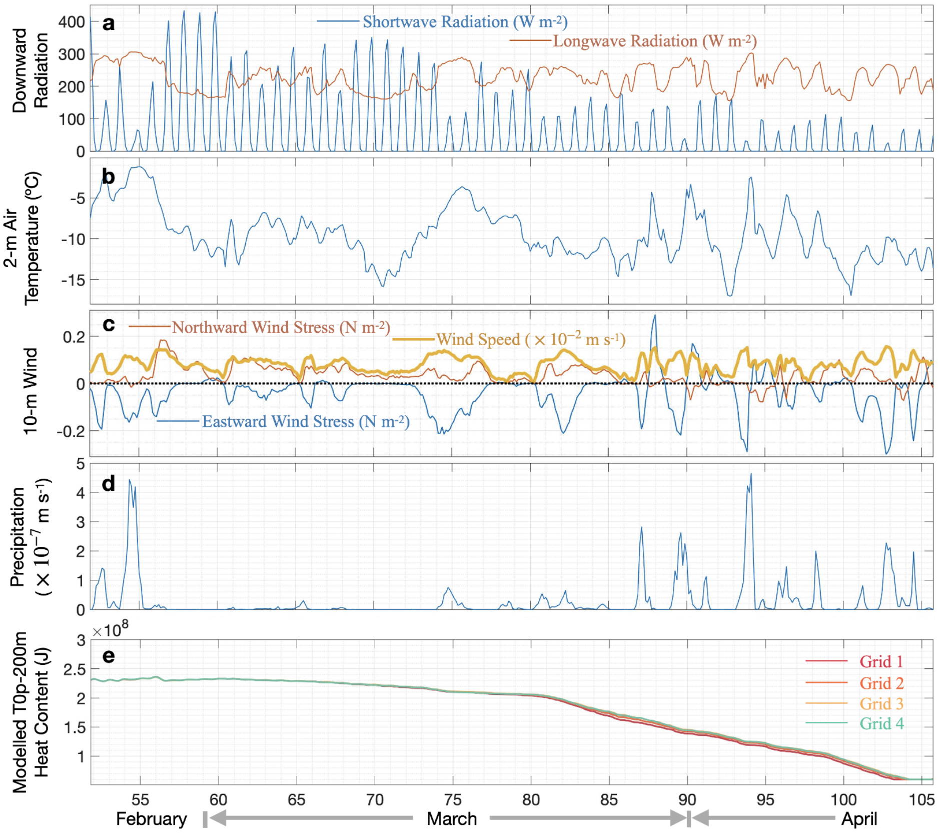

Figure 4.4: Time series of ERA5 reanalyses used as atmospheric forcing and for air-sea fluxes estimation. **a.** Downward radiation. **b.** 2-m air temperature. **c.** 10-m wind stress. **d.** Precipitation **e.** Comparison among modelled top-200-m heat content forced by reanalysis at four different grids.

4.3.6 Definition of the mixed-layer depth for observation and model results

We define the observed mixed-layer depth as the depth where the buoyancy frequency, whose value represents the ocean stratification, is the greatest. The observations sometimes contain small-scale perturbations that can cause abnormally strong stratification, that are even stronger than the stratification at the base of the mixed layer, at very deep or shallow depths. To avoid including those perturbations when determining the mixed-layer depth, we bin-average the temperature and salinity measurements into 5-m bins before calculating the buoyancy frequency. For reference, the resultant mixed-layer depth is not sensitive to the choice of the bin size, but a 5-m bin size effectively eliminates the effect of these erroneous small-scale perturbations.

The modelled mixed-layer depth is defined in the model run in each model step. The model will mix the water column until the water column is statically stable and the vertical shear is not enough to break the stratification. The critical gradient Richardson number and the critical bulk Richardson number are set to 0.25 and 0.65 respectively.

The resultant mixed-layer depths, for both observations and model results, are very close to the mixed-layer depths we would choose by visual inspection (see Figure 4.6, 4.7).

4.4 Observed intense cooling, salinification and mixed layer deepening

We analyse the changing ocean properties during non-summer seasons using a combination of profiles from *EM959* during Feb to Apr and later, lower-resolution profiles from MEOP during May and Sep (Figure 4.5). The mixed-layer temperature is always close to the freezing point (<-1.6°C), while the salinity and density generally increase over time (Figure 4.5a,b). As a result, the upper-ocean water gradually transitions from Antarctic Surface Water to WW (Figure 4.5). Below around 200 m, the hydrographic properties do not show any clear trend (Figure 4.5a), indicating negligible seasonal cycle. The MEOP seal-tag dataset shows that the mixed-layer salinification continues through May (blue circles in Figure 4.5b); and in September (dark grey dots and lines in Figure 4.5b), the surface properties match the WW definition and the whole water column has a similar density, suggesting that the stratification has eroded almost completely.

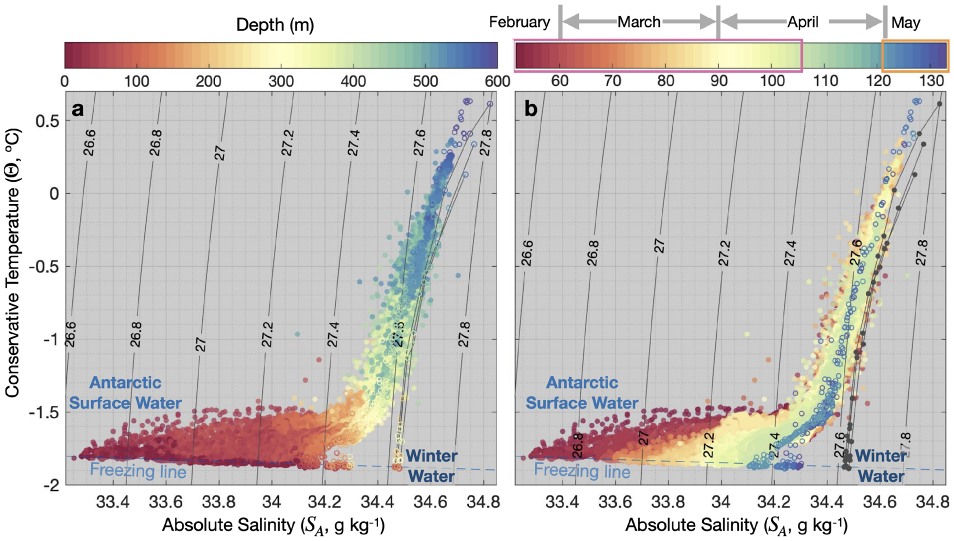

Figure 4.5: Conservative temperature - absolute salinity (Θ–S_A) diagrams, coloured by **a** depth and **b** year day of measurement. Filled dots show the recovered *EM959*, with year day indicated by the pink rectangle in the colour bar above panel **b**. Open circles show MEOP measurements from 01-13 May 2014, with year day indicated by the orange rectangle. Circles that are connected by grey lines are measurements from 01 Sep 2014; they are coloured in dark grey in panel **b**. Observations obtained in later dates overlay observations obtained in earlier dates.

The highest temperature observed in this region is about 0.6 °C, which is similar to the mCDW temperature historically observed in this region (*Jacobs et al.*, 2012, *Yang et al.*, 2022). However, the permanent pycnocline lies between the mCDW and the Winter Water is not distinct here (Figure 4.5), possibly because the water depth here is too shallow to reach the permanent pycnocline, or the shallow bathymetry is causing a vigorous mixing.

Those short-term events may also be responsible for the non-monotonic mixed-layer change before mid-March, i.e., the mixed-layer deepening often before mid-March. To investigate the occurrence and frequency of the short-term events, we conduct a spectrum analysis using *EM959* temperature and salinity measurements. Nonetheless, it does not reveal any dominant short-term frequency. We also do not see a significant diurnal cycle. This may be because the solar radiation is weak in austral autumn so that it is largely overwhelmed by the continuously high heat loss from the ocean to atmosphere.

The near-freezing mixed layer experiences an intense salinification, from about 33.3 g kg^{-1} to 34.1 g kg^{-1}, due to sea ice formation and brine rejection (Figure 4.6b). The estimated sea ice formation rate is about 3 cm per day. This sea ice formation rate is comparable to the reported sea ice formation rate in high-sea-ice-concentration region (about 3 cm per day on average, e.g. *Charrassin et al.*, 2008) but much higher than in low-sea-ice-concentration region (about 1 cm per day on average, e.g. *Meredith et al.*, 2011) in austral Autumn. With the increase of salinity and the decrease in temperature, the potential density of the mixed layer increases significantly from about 1027 kg m^{-3} to about 1027.4 kg m^{-3}, resulting in vertical convection that contributes to the deepening of the mixed layer over time, from about 25 m to 125 m (white lines with black edges in Figure 4.3). The seasonal pycnocline is apparent at the bottom of the mixed layer. This seasonal pycnocline erodes gradually in autumn, as evidenced by the reducing stratification at and immediately below the base of the mixed layer (Figure 4.3c).

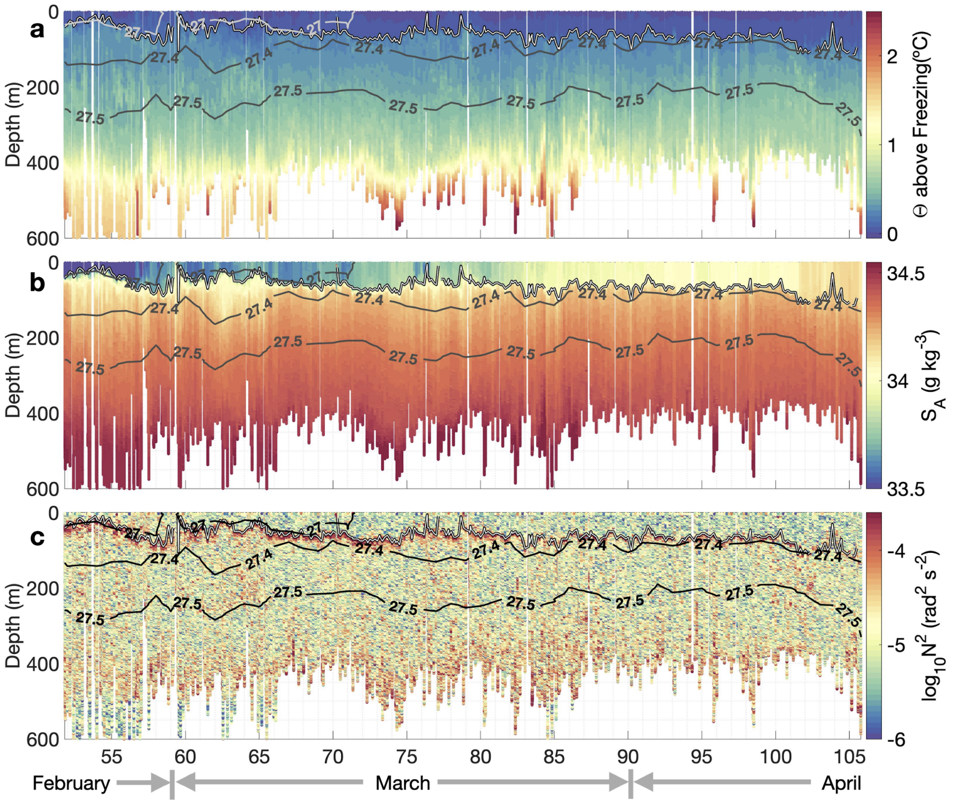

Figure 4.6: **Time series of conservative temperature (Θ) above freezing, absolute salinity (S_A), and water stratification ($log_{10}N^2$).** This figure includes all measurement points collected by *EM959* during year day 51-106 (pink circle in the map in Figure 4.1 and the pink rectangle in the colour bar in Figure 4.1). The thick grey/black lines denote potential density that has been vertically bin-averaged into 5-m bins. The thin white lines with black edges are the bottom of the mixed layer.

4.5 The effect of sea ice blocking air-sea fluxes on the upper-ocean processes

4.5.1 The modelled upper-ocean processes forced with different $pSIC$ values

As mentioned in section 4.3.4 we use pSIC to represent the effect of sea ice on the air-sea heat and freshwater fluxes. We do not consider the effect of sea ice on the air-sea momentum flux as sea ice may enhance or reduce the air-sea momentum flux depending on the mobility of sea ice (e.g. *Meneghello et al.*, 2018, *Zheng et al.*, 2022). We investigate the effect of momentum flux as a sensitivity experiment of the model by applying atmospheric forcings with the wind stress value altered to 0%, 25%, 50% and 75% of its original value, while keeping the rest of the atmospheric variable untouched. The model results with modified-wind-stress forcings applied suggest that the effect of momentum flux on the upper-ocean is negligible – the maximum difference among the modelled mixed-layer depths forced by different wind stress values is 3 m. This implies that buoyancy forcing dominates over wind forcing in the water column's vertical processes in this regime, we therefore focus on the impact of sea ice on buoyancy forcing in the following investigation.

Similarly, to further estimate the effect of precipitation minus evaporation (i.e. non-sea-ice related air-sea freshwater flux) on the upper-ocean processes independently, we re-run the model with the precipitation and evaporation remaining unmodified with the heat flux reduced to zero. Compared with the simulation where heat flux, precipitation and evaporation are all reduced to zero, the difference in modelled mixed layer depth is less than 3 m. This demonstrates that the effect of precipitation minus evaporation on the upper-ocean processes is insignificant and the upper-ocean salt content change is dominated by the sea ice formation processes and advection.

Our model reproduces mixed layers that experience gradual cooling and salinification over time (Figure 4.6). As the $pSIC$ reduces the air-sea buoyancy flux, the lower pSIC is, the higher the heat loss is. Consequently, the mixed-layer salinification and deepening are the strongest in $0\% - pSIC$ and the weakest in $100\% - pSIC$ (Figure 4.6), as expected.

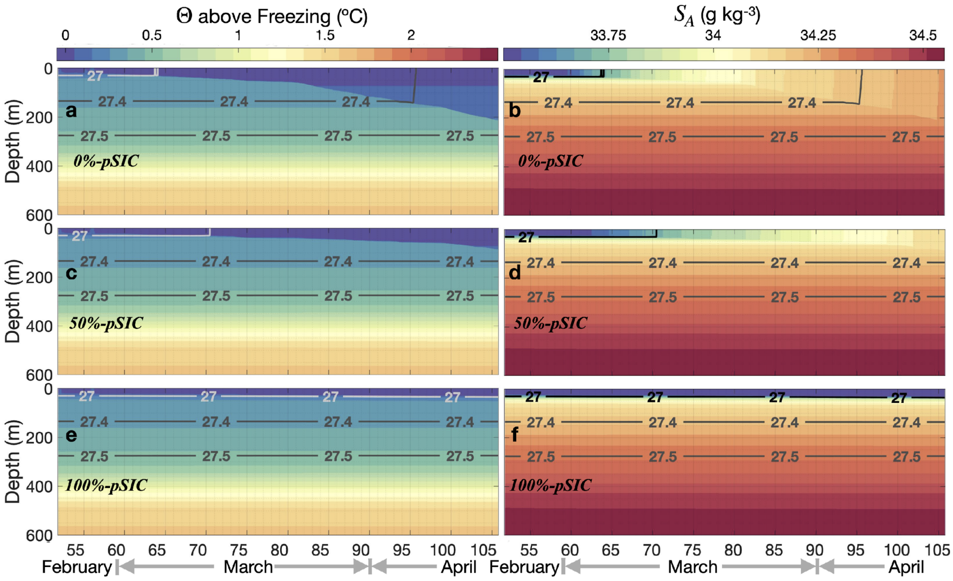

Figure 4.7: **Examples of time series of modelled temperature and salinity.** **a** and **b** are for 0 %-*pSIC*, c and d are for 50 %-*pSIC*, and **e** and **f** are for 100 %-*pSIC*. Contours indicate potential density. The colour schemes are the same as in Figure 4.6.

We further compare the observations with all model simulations in Figure 4.8, focusing on the top-200 m heat content, accumulated sea ice formation and mixed-layer depth. Note, the modelled mixed-layer depth shoals to around 5 m, for about six hours in simulations 0%-*pSIC* and 25%-*pSIC* near day 79, due to a warming event in the ERA5 reanalysis that combines relatively warm air temperature, relatively strong solar radiation and weak wind stress (Figure 4.4).

The satellite images showing the highly streaky appearance near Bear Ridge indicates the presence of frazil ice (*Wadhams et al.*, 2018). Figure 4.1 and Figure 4.3 show the appearance of the frazil ice starting from 20/Feb/2014 at the earliest, one day earlier than our *EM959* measuring period, and was almost always present during the *EM959* measuring period. Instead of accumulating locally to form thick sea ice, the newly formed frazil sea ice continues to be blown away from the sea-ice-formation sites by the prevailing winds. The frazil sea ice in the sampling region is assumed to have little effect on the air-sea interactions because it is too thin and mobile to block the air-sea fluxes. Therefore, the pSIC that best fits reality is anticipated to be 0%-*pSIC*.

Our 0%-*pSIC* reproduces trends of upper-ocean cooling and mixed-layer deepening over time similar to the observations (Figure 4.7a). However, without sea ice present these trends are too strong compared with the observations (Figure 4.8a,c). Instead, the observed trends of upper-ocean features are most similar to simulation 50%-*pSIC*, especially after late March. 50%-*pSIC* has a lower buoyancy loss from the ocean to the atmosphere than 0%-*pSIC*. Hence, this similarity between 50%-*pSIC* and the observations indicate that there is extra heat and/or freshwater input that is not considered in model simulation, e.g. relatively warm and/or fresh advection. We discuss this possibility of lateral advection transporting heat and/or freshwater into the study region in Section 4.5.2.

There are some short-term variations in the upper-ocean heat content and mixed-layer depth in the observations (e.g. in February, Figure 4.8a,b), which might be caused by eddies passing by, that will not be reproduced by the model.

The accumulated sea ice formation generally increases over time in both the model and observations, i.e. sea ice grows nearly constantly. The sea ice formation rate is higher in observation-derived budgets than all model results. As the salinity difference between the mixed layer and the water below it is very large, the salt-budget-derived sea ice formation rate is sensitive to deep-water entrainment/upwelling. Hence, the fluctuations in the salt-budget-derived line in February are likely artefacts caused by the entrainment/upwelling of the deeper saltier waters (Figure 4.8b). In March, the salt-budget-derived sea ice formation rate agrees with that derived from the heat-budget fairly well. Although they have different values because neither the salt budget nor the heat budget is perfectly closed in the calculation, the similarity between their values gives us confidence that our calculations are valid in the ASP. The salt-budget-derived sea ice formation rate is lower than the heat-budget-derived sea ice formation rate in April (again give numbers - how much lower), which, again, may suggest the existence of extra freshwater and/or heat input that is not considered in the budget estimations.

4.5.2 Effect of advection on the upper ocean processes

The sea ice east of Bear Ridge is fast ice, which is distinct from the observed frazil-ice-dominated conditions in the ASP (Worldview). The fast ice to the east of Bear Ridge may reduce air-sea fluxes. Over the period of our study this water would therefore be insulated from surface fluxes and experience minimal salt input from sea ice formation, thus we expect the water properties to be similar to those of the initial conditions, with a relatively warm and fresh feature. We suspect that this water mass can be advected westward following the coastal current, bringing heat and freshwater to the study site, affecting our sea ice formation calculation. To assess the impact of lateral advection that may transport heat and freshwater from outside of our observational site, we incorporated an additional relaxation module into our 0%-*pSIC* simulation (referred to as 0%-*pSIC*+Advection). The following experiments are not supposed to be realistic, but instead to determine if it is possible to find an idealised rate of relaxation such that the model simulations match the observed and calculated trends in heat content, mixed layer depth and sea ice formation.

In this experiment, the entire water column's temperature and salinity are relaxed to the initial profiles (i.e. observed measurements in Feb) using the following equations:

$$T_{n_{relaxed}} = T_n + RelaxationRate_T \times (T_n - T_{initial}),$$

$$S_{n_{relaxed}} = S_n + RelaxationRate_S \times (S_n - S_{initial}),$$

where T_n and S_n are the modelled temperature and salinity profiles at time step n, $T_{initial}$ and $S_{initial}$ are the initial profiles, $T_{n_{relaxed}}$ and $S_{n_{relaxed}}$ are the relaxed modelled profile at time step n, and $RelaxationRate_T$ and $RelaxationRate_S$ are the relaxation rates for temperature and salinity respectively. We test a range of order $RelaxationRate_T$ and $RelaxationRate_S$, varying from the order -10^{-7} to -10^{-4} (not shown) and find that the $RelaxationRate_T = RelaxationRate_S = 2 \times 10^{-5}$ provides the best agreement with the observations (Figure 4.8 dark green line).

The 0%-*pSIC*+Advection simulation indicates that the advection of fresher and warmer water slows down upper-ocean heat-content reduction (Figure 4.8a, dark green line) and stabilises the mixed-layer depth (Figure 4.8c, dark green line). With a shallower mixed-layer depth, less heat is entrained into the mixed layer from the deeper ocean. Since the mixed layer is already at the freezing point, this results in an increase in sea ice formation, with the increased release of latent heat compensating for the reduced heat supply from below (Figure 4.8b, dark green line). This advection module reduces the discrepancies between 0%-pSIC simulation and the observation. This suggests that our observational estimates of sea ice formation rates are likely to be underestimated and are the lower bound of the actual sea ice formation rate.

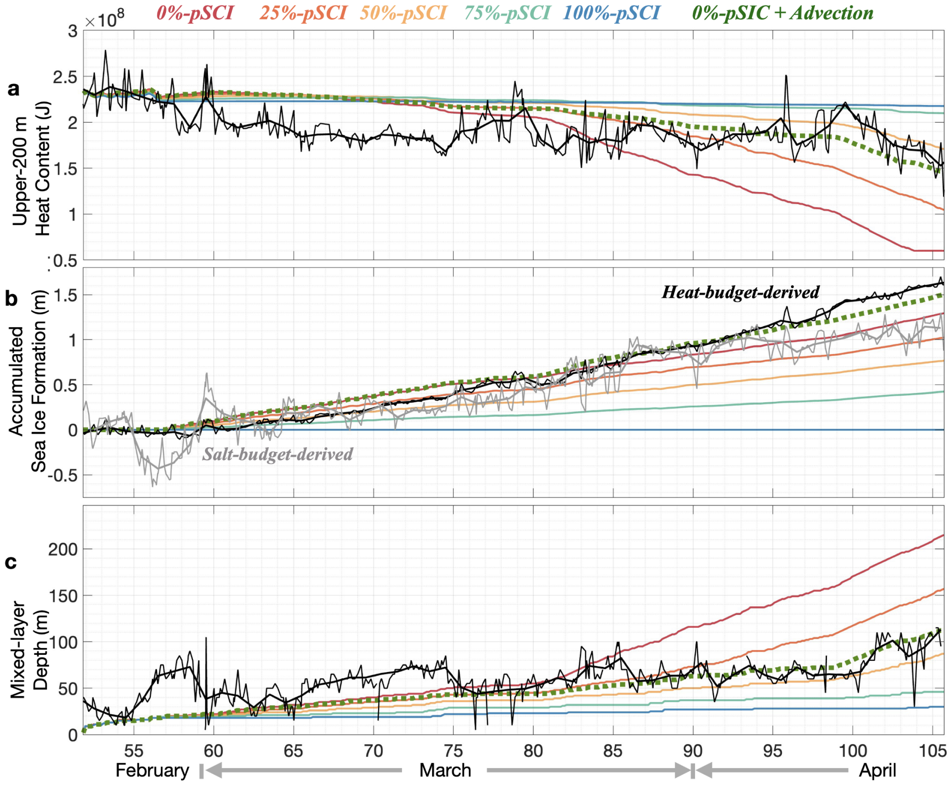

Figure 4.8: **Comparison among observations and model results with different *pSIC*. a** Upper 200 m heat content. Model results are coloured by the colour scheme shown on the top of the panel. Observations collected by *EM959* are coloured in black, with the thin line for the heat content of each profile and the thick line for daily-averaged heat content. **b** Same as **a** but for sea ice formation. The line for heat-budget-derived ice formation is coloured in black and the line for salt-budget-derived ice formation is coloured in grey. **c** Same as **a** but for mixed-layer depths.

4.6 Discussion

We acknowledge that reanalyses are known to exhibit large biases in the region, especially close to ice shelves and in the presence of strong katabatic winds (*Jones et al.*, 2016). This might be because the reanalysis often fails to capture high wind bursts that could cause strong wind stirring to deepen the mixed layer, and abrupt air temperature decreases that would increase ocean heat loss to the atmosphere (*Jones et al.*, 2016). Hence, the effect of high wind and abrupt air temperature drop can only be shown in the observed heat content change, but not in the heat flux calculated from reanalysis.

The model captures the trends of the observed heat content, accumulated sea ice formation and mixed-layer deepening well when appropriate atmospheric forcings and simulated advection are applied. However, it cannot explain the observed irregular and abrupt cooling, salinification and/or mixed-layer deepening events (Figure.4.5-4.7). This discrepancy between our model results and the observations might be because of 3-D ocean processes not accounted for in our 1-D model. The intrusion of warm mCDW from deeper site was reported in summer on a fast ice to the west of Bear Island (*Ackley et al.*, 2015), potentially that mCDW intrusion also occurred during *EM959* measuring period. As mentioned above in Section 4.3.1, eddies and topographic Rossby waves that can result in the vertical fluctuation of the isopycnals have been observed in to north of ASP (*St-Laurent et al.*, 2015, *Wåhlin et al.*, 2016) and cause the pattern we observed.

4.7 Conclusions

In this study, we use a full-depth hydrographic dataset measured in high frequency by a recovered seal tag to investigate upper-ocean processes close to the Antarctic continent during austral autumn (mid-February to late-April). During our observational period, available satellite images show mostly frazil sea ice (Figure 4.3), which has little effect on air-sea heat exchange. Our dataset reveals upper-ocean cooling, salinification and densification, and the consequent erosion of stratification. It also captures a gradual and constant mixed-layer deepening with several abrupt deepening events (Figure 4.6). A 3 cm per day sea ice formation rate and a 2 m per day mixed layer deepening are observed, comparable to previous studies (e.g. *Charrassin et al.*, 2008). We use a 1-D mixed layer model to investigate the possible mechanisms controlling the upper-ocean processes with a focus on exploring the influence of sea ice in reducing the air-sea heat flux. Our model results show the effect of sea ice cover reducing the air-sea heat flux. Some of the discrepancies between the model and observations further emphasise the uncertainty introduced by poorly constrained lateral advection, both within and beneath the mixed layer. The results of this study are not only important for the ASP and the local carbon cycle and ecosystem but may also apply to other coastal polynyas in Antarctica and beneficial for future model parameterisation. Understanding the polynya formation processes previously limited by sparse observations is of high interest to ocean and cryosphere research.

5

Conclusions

5.1 Summary

5.1.1 Background to the thesis

The accelerating ice mass loss of Antarctica is primarily due to the oceanic melting of ice shelves (e.g. *Pritchard et al.*, 2012). The most rapid melt has been reported in some ice shelves in the southeastern Amundsen Sea, such as Pine Island Ice Shelf, Thwaites Ice Shelf and Dotson Ice Shelf (e.g. *Paolo et al.*, 2015). The ocean-atmosphere-ice interaction in the southeastern Amundsen Sea determines the amount of poleward heat transport that contributes to ice shelf melt and hence is crucial for the ice shelves' future. However, the study of the marine environment in the southeastern Amundsen Sea has been greatly limited by the lack of observations. Fortunately, cruises to the Amundsen Sea in the past two decades have greatly increased the amount of observations available in this region, especially in non-summer seasons. Combined with some idealised model simulations, these new measurements allow me to investigate the physical mechanisms controlling regional hydrography in detail. This thesis focuses on three aspects regarding the interactions between the ocean, ice shelves and sea ice, with the main results summarised in subsequent subsections, suggestions for future work outlined in Section 5.2, and the broader implications of the thesis results discussed in Section 5.3.

5.1.2 Meltwater pathways in winter in front of Pine Island Ice Shelf

Chapter 2 presented the first full-depth winter temperature and salinity measurements in front of the Pine Island Ice Shelf obtained by seal tags in 2014. These observations reveal a highly variable meltwater distribution, featuring two meltwater-rich layers at about 450 m and above 250 m, connected by scattered meltwater-rich columns. The relatively warm meltwater-rich water can be unambiguously identified from the near-freezing ambient water. In contrast to winter observations, summer observations collected by ship-based CTD in similar locations show a homogeneous distribution of meltwater in the top 450 m.

My co-authors and I hypothesise that this seasonal difference in meltwater distribution is caused by the seasonal stratification of the upper ocean ($>$ 450 m). In summer when the upper ocean is heated by solar radiation and freshened by sea ice meltwater and glacial surface runoff, the upper ocean becomes highly stratified. The meltwater coming out from the ice cavity rises due to its relatively high buoyancy, tilting the isopycnals and triggering centrifugal instability that results in vigorous mixing (*Naveira Garabato et al.*, 2017). On the contrary, in winter the upper ocean experiences surface cooling, wind stirring and brine rejection, consequently forming a uniform Winter Water layer that is cold and dense. This uniform Winter Water layer allows meltwater to rise to the near surface via those meltwater-rich columns, without undergoing intense mixing. In addition, more meltwater is buoyant enough to rise to the near surface when the upper ocean is dense in winter.

Hence, in winter more meltwater-rich water can rise to the near surface nearly unmodified, with the heat and nutrients it carries, affecting the near-surface hydrography. The heat brought to the near surface helps to maintain the coastal polynya, and the nutrients brought to the euphotic zone boost the phytoplankton bloom in the next spring/summer.

5.1.3 The influence of wind-ice interactions on ocean gyres

Chapter 3 presented velocity measurements obtained in a habitually ice-covered region to the west of the Thwaites Ice Shelf in 2019. These velocity measurements reveal an anti-cyclonic ocean gyre (i.e. anti-clockwise in the Southern Hemisphere; hereafter, Thwaites gyre) for the first time, despite the climatologically cyclonic wind stress curl (i.e. clockwise in the Southern Hemisphere) in the southeastern Amundsen Sea. The only other ocean gyre that has been reported in the southeastern Amundsen Sea is the gyre in front of the Pine Island Ice Shelf, which is cyclonic (e.g. *Thurnherr et al.*, 2014), consistent with the cyclonic wind stress curl there. Except for the gyre direction, the main difference between this Pine Island Ice Shelf gyre, and the new Thwaites gyre, is the sea ice conditions in the gyre region. Pine Island Ice Shelf gyre is in open ocean during summer, while the Thwaites gyre is partially covered by sea ice. Hence, we hypothesise that the sea ice conditions in the gyre region can reverse ocean gyre direction relative to ice-free conditions.

To test this hypothesis, my co-authors and I designed numerical experiments based on a barotropic set-up of the MITgcm with a range of combinations of different wind stress curl fields and sea ice conditions comparable to the observations. The model reproduces the observed gyre features well, when appropriate representations of the observed wind field and sea ice distribution are applied. The modelled gyre direction depends upon the area-integrated ocean surface stress curl, which is determined by the applied wind stress curl field, the percentage of wind stress transferred through the ice, and the angle between the wind direction and the sea ice edge. When the sea ice blocks the majority of the wind stress, the magnitude of the integrated ocean surface stress curl along the sea ice edge can exceed that in the open water region, thus allowing the gyre to rotate in the opposite sense to the wind stress curl. This chapter demonstrates the potential of sea ice and ice shelves to play a key role in regulating ocean gyre direction and strength.

5.1.4 Upper-ocean processes in the Amundsen Sea Polynya in austral autumn

Chapter 4 presented the first full-depth autumn salinity and temperature time series from the southeastern corner of the Amundsen Sea Polynya, obtained by a recovered seal tag deployed in 2014. These observations are vertically well-resolved (i.e. measured at 1-Hz frequency), giving much more precise details of the stratification than seal-tag observations we normally obtain, which only have about eighteen points over each profile. These new observations capture the evolution of the mixed layer during a polynya formation period. The upper ocean experiences intense cooling, salinification and mixed-layer deepening, with occasional abrupt (i.e. within a few days) cooling events that may be due to short-lived storms or lateral ocean advection by eddies and currents. From the observations, we calculate an average sea ice formation rate of approximately 3 cm per day. This sea ice formation rate is comparable to high-sea-ice-concentration region (about 3 cm per day on average, e.g. *Charrassin et al.*, 2008) and much higher than the low-sea-ice-concentration region (about 1 cm per day on average, e.g. *Meredith et al.*, 2011) in austral Autumn.

To investigate the physical mechanisms that control the upper ocean hydrography, my co-authors and I ran a 1-D bulk ocean mixed-layer model forced with ERA5 reanalysis. We assume that sea ice reduces the air-sea heat flux by a certain percentage and test various levels of this effect. Although the model, or perhaps the meteorological forcing, cannot capture the short-term cooling events, the model reproduces a gradual cooling, salinification and mixed-layer deepening similar to the observed upper ocean.

During most of the observational period of the seal tag, the study area is either ice-free or covered by frazil ice only. Hence, the air-sea heat flux is not likely to be affected by sea ice. However, the modelled upper ocean is most similar to the observations when an assumption of sea ice reducing half of the heat flux is applied. This may indicate that warm and fresh water is advected into our study region, which might come from the westward coastal current from Pine Island Bay (e.g. *Biddle et al.*, 2017), which passes under a large region of fast ice, thus likely to be influenced by reduced air-sea heat flux.

5.2 Future work

Chapter 2 identified the meltwater pathways and reveals a seasonal meltwater distribution that may be attributed to the seasonal upper-ocean stratification. Some further improvements and future work could be done to extend this work, as listed below:

- More seal tags were deployed and collected hydrographic measurements in a similar region in 2019, 2020 and 2022. A comparison between those years and the observations we obtained in 2014 would allow us to study the inter-annual variability of meltwater distribution. One could also use the observations from those three new years to test whether, and under what circumstances, the hypothesis Chapter 3 suggested is valid.
- The meltwater can be unambiguously identified from sea surface temperature, which makes satellite-based monitoring of meltwater pathways possible. I have been involved with new work using remote sensing to do this, led by Elena Savidge, and these results will be submitted for publication shortly. This study tests the application of using the remotely-sensed brightness temperature to monitor the meltwater and the polynyas that are formed by the meltwater (i.e. meltwater melts the sea ice to form polynyas).
- A comparison between different ice shelves could be conducted. For example, Chapter 2 also mentions briefly that, similar to what was observed in winter in front of the Pine Island Ice Shelf, a weakly stratified upper ocean was identified along with a patchy meltwater distribution in summer near the Totten Ice Shelf. More observations of different ice

shelves, especially in winter, could allow further investigation and comparison between different ice shelves to better understand regional influences.

- Moreover, although Chapter 2 highlights only the seasonal meltwater pathway, it is expected that seasonality is experienced by other hydrographic features, such as the local circulation and mixed layer depths. The lack of non-summer observations has greatly limited the verification of non-summer climate model output. The results presented in this chapter might help to verify and explain the model output. In addition, I urge that more effort should be made towards obtaining non-summer measurements and the investigation of the local seasonality of polar environments.

Chapter 3 suggested that the presence of sea ice or ice shelves might reverse the ocean gyre direction relative to the ice-free condition. Some future work regarding model design and gyre observations could be done to extend this work, as listed below:

- In this chapter, my colleagues and I used a range of sea ice conditions and wind fields to cover scenarios that may occur in reality; nonetheless, this work was purely based on a barotropic setup. Hence, the main future focus could be using a baroclinic set-up with different water stratifications that are similar to observations to test how the wind-ice interactions are influenced by vertical stratification.

- The buoyant glacial meltwater coming out from the ice cavities turns left due to Coriolis force (in the Southern Hemisphere), which may drive a current along the ice shelf, potentially maintaining ocean gyres (e.g. *Yoon et al.*, 2022, *Zheng et al.*, 2021). With the baroclinic set-up, one could also add a meltwater injection into the model and quantify the impact of meltwater on gyre circulation.

- Although regional numerical models have shown gyres and eddies in the continental shelf seas (e.g. *Nakayama et al.*, 2019), there are very few gyres that have been observed in situ. In the Amundsen Sea, the winds are stronger during non-summer seasons, when sea ice covers most of the open ocean, which might mean that the air-sea momentum exchange is rather small. Therefore, it brings an intriguing question: are there many gyres in the Amundsen Sea that have not been detected? Or is the momentum flux from the wind too weak, or is its impact too brief (due to sea ice blocking), such that it cannot maintain gyres? More comprehensive in situ surveys are required for answering these questions.
- Another feasible way to monitor the gyres may be using altimeters or sea surface temperature products. Sea surface height at the gyre centre is likely to be higher when it is anticyclonic and lower when it is cyclonic. Warm or cold surface water that is circulated by gyres can leave a circle or half circle feature of sea surface temperature anomaly that can be identified from radar infrared observations (e.g. *Mankoff et al.*, 2012).

Chapter 4 used full-depth seal-tag observations to present the formation processes of the Amundsen Sea Polynya in austral autumn, and a 1-D model to reproduce observed upper-ocean features. However, there are a few aspects that remain to be investigated to make the most use of these well-resolved measurements and understand the physical processes of the upper ocean after summer, as listed below:

- This chapter mentioned that the abrupt cooling events may be caused by short-lived storms, eddies or waves, but this is not certain. A mooring that is located at the eastern edge of the Dotson Ice Shelf measured the temperature, salinity and velocity from Feb 2014 to Feb 2016 at several fixed depths below $\sim$ 200 m (e.g. *Yang et al.*, 2022). This mooring may have captured some processes on similar time scales, giving us more insights into what those processes are. When short-lived storms happen, the sea ice concentration will change rapidly within days. Hence, the sea ice concentration products could help to identify the contribution of storms to the observed abrupt cooling events.

- Recent observations from seal tags show that seals in the Amundsen Sea are particularly interested in lingering around the Amundsen Sea Polynya in 2019, 2020 and 2022 (personal communications with Guilherme A. Bortolotto). This indicates that the high productivity in this polynya has attracted more marine mammals, and should be a focus for future marine mammal research campaigns.

5.3 Broader implications of this thesis

This thesis investigates the oceanography of the southeastern Amundsen Sea from three different aspects in Chapters 2–4, regarding the glacial meltwater pathway in winter, the influence of wind-ice interactions on ocean gyres, and upper ocean evolution in autumn. The implications of the results of each chapter are discussed below.

Chapter 2 has suggested that the meltwater in winter is likely to penetrate through the Winter Water layer without undergoing intense mixing, transporting heat and nutrients to the near surface more efficiently than we expected. This will increase the temperature of the near-surface layer to up to about 1 °C above freezing, melting sea ice and maintaining polynyas, and eventually will enhance the air-sea fluxes. The enhanced fluxes could further influence iceberg calving (e.g. *Bintanja et al.*, 2015, *Silvano et al.*, 2018) and ice shelf melting (*Fogwill et al.*, 2015, *Webber et al.*, 2019). This rising of meltwater from depth might also reinforce local ventilation and the overturning circulation near ice shelves (e.g. *Naveira Garabato et al.*, 2017, *Webber et al.*, 2019, *Yoon et al.*, 2022), resulting in more warm water into the ice cavity to melt ice shelves (e.g. *Webber et al.*, 2019). Meltwater brings the nutrients from mCDW and the base of glaciers to the euphotic zone, which may boost productivity in the following spring/summer, so its pathways are of interest to biologists studying local phytoplankton blooms. The high concentration of meltwater in the euphotic zone may cause a "biological pump" and partially explain why the Amundsen Sea is a significant carbon sink in the local carbon cycle (e.g. *Yager et al.*, 2016).

Meltwater in the Amundsen Sea is not only important for local hydrography and biochemistry, but also has an impact on the Antarctic Bottom Water formation as it freshens the upper ocean and prohibits deep convection (e.g. *Lago and England*, 2019, *Silvano et al.*, 2018), leading to further impact to global climate. Quantifying the effect of meltwater on local hydrography is especially important in the Antarctic continental shelf seas as ice shelf melting here is accelerating (e.g. *Paolo et al.*, 2015), exporting an increasing amount of glacial meltwater into the ocean.

The meltwater pathways have been presented in climate models as a surface injection or uniform layers at specific depths without seasonality (e.g. *Bronselaer et al.*, 2020). This might result in significant biases in the representation of ocean circulation, ocean-ice shelf interaction, surface heat exchanges, local primary production and carbon uptake. The results shown in Chapter 2 can be applied to the representation of meltwater injection in depth in climate models, improving the prediction of future climate.

Basal channels of ice shelves may reduce the ice-shelf structural integrity and potentially destabilise ice shelves (e.g. *Alley et al.*, 2016). Basal channels concentrating and steering basal meltwater are also melted and enlarged by the basal meltwater flowing along them. Chapter 2 shows that in winter the meltwater-rich water exported from the ice cavities is less likely to mix with ambient water and can leave warm signals at the sea surface that can be identified from remote sensing. If a warm signal is present in front of a basal channel, it might indicate that the basal channels are experiencing rapid melt from the heat of meltwater-rich water. Hence, winter sea surface temperature may allow glaciologists to monitor and predict the fate of basal channels.

Chapter 3 emphasised again the importance and complexity of the ocean-ice-wind interactions, especially the close relationship between the ocean currents, wind fields and ice types. Most sea ice products focus only on the sea ice concentration, ignoring the types of sea ice, which are suggested to be crucial for the ocean gyres via the impact on the transfer of wind stress through the sea ice in Chapter 3. I suggest the processes revealed in Chapter 3 should be parameterised into coupled models, and more remote-sensed observations for sea ice types should be considered.

For ice shelves that are close to ocean gyres, the gyres' effect on melt rate should be considered. The change of direction of gyres might be responsible for the interannual variabilities of melt rates. The depth of pycnocline separating mCDW and Winter Water is critical for warm-cavity ice shelves because it determines the thickness of warm mCDW that can melt ice shelves. As gyres generate vertical displacement of the pycnocline, they might control the portions of bases of ice shelves that are in contact with mCDW, and might alter the amount of heat that can be transported into ice cavities. A recently published work has revealed that the location change of the gyre in front of Pine Island Bay reduces the heat fluxes towards the ice cavity (*Yoon et al.*, 2022).

The gyres near ice shelves may also circulate the water around ice shelves. *Zheng et al.* (2021) reveal that meltwater is entrained into the gyre in front of the Pine Island Ice Shelf and transported away from the ice shelf. Hence, gyres can expand the meltwater-influenced region, potentially impeding sea ice formation, causing polynyas, and altering the locations and timing of local phytoplankton bloom.

Chapter 5 highlighted the importance of sea ice on upper-ocean stratification. Antarctic sea ice concentration reached its minimum recorded level since 1979 in February 2022, while the southeastern Amundsen Sea experienced a high sea ice concentration anomaly (*Turner et al.*, 2022). This unusual sea ice concentration pattern might have a further impact on the 2022 autumn/winter and future water stratification and hence influence circulation due to baroclinicity in the surface water layers. These changes could ultimately influence the formation, timing and extent of the polynyas, thus influencing productivity and carbon uptake, and could generate feedback on the sea ice variability. Further in-situ observations, perhaps from tagged seals, would be needed to study such processes.

Bibliography

Ackley, S, Xie, H., & Tichenor, E. Ocean heat flux under Antarctic sea ice in the Bellingshausen and Amundsen Seas: two case studies. *Ann. Glaciol.* **56**, 200–210 (2015).

Ackley, S. et al. Sea-ice production and air/ice/ocean/biogeochemistry interactions in the Ross Sea during the PIPERS 2017 autumn field campaign. *Ann. Glaciol.* **61**, 181–195 (2015).

Alley, K. et al. Impacts of warm water on Antarctic ice shelf stability through basal channel formation. *Nat. Geosci.* **9**, 290–293 (2016).

Arrigo, K. R., & G. L. van Dijken, Phytoplankton dynamics within 37 Antarctic coastal polynya systems. *J. Geophys. Res.* **108**, C83271 (2003).

Arrigo, K. R. van Dijken, G. L. & Long, M. Coastal Southern Ocean: A strong anthropogenic CO_2 sink. *Geophys. Res. Lett.* **35**, L21602 (2008).

Arrigo, K. R., van Dijken, G. L. & Bushinsky, S. Primary production in the Southern Ocean, 1997–2006. *J. Geophys. Res.* **113**, C08004 (2008).

Arrigo, K. R., Lowry K. E. & van Dijken, G. L. Annual changes in sea ice and phytoplankton in polynyas of the Amundsen Sea, Antarctica. *Deep Sea Res. Part II* **71**, 5–15 (2012).

Assmann, K. M. et al. Variability of Circumpolar Deep Water transport onto the Amundsen Sea continental shelf through a shelf break trough. *J. Geophys. Res. Oceans* **118**, 6603–6620 (2013).

Bamber, J. L. et al. Ice sheet contributions to future sea-level rise from structured expert judgment, *P. Natl. Acad. Sci. USA* **116**, 11195–11200 (2019).

Beaird, N., Straneo, F. & Jenkins, W. Spreading of Greenland meltwaters in the ocean revealed by noble gases. *Geophys. Res. Lett.* **42**, 7705–7713 (2015).

Bett, D. T. et al. The impact of the Amundsen Sea freshwater balance on ocean melting of the West Antarctic Ice Sheet. *J. Geophys. Res. Oceans* **125**, e2020JC016305 (2020).

Biddle, L. C., Heywood, K. J., Kaiser, J. & Jenkins, A. Glacial meltwater identification in the Amundsen Sea. *J. Phys. Oceanogr.* **47**, 933–954 (2017).

Biddle, L. C., Loose, B. & Heywood, K. J. Upper ocean distribution of glacial meltwater in the Amundsen Sea, Antarctica. *J. Geophys. Res. Oceans* **124**, 6854–6870 (2019).

Bindschadler, R., Vaughan, D. G. & Vornberger, P. Variability of basal melt beneath the Pine Island Glacier ice shelf, West Antarctica. *J. Glaciol.* **57**, 581–595 (2011).

Bintanja, R., Van Oldenborgh, G. J., & Katsman, C. A. The effect of increased fresh water from Antarctic ice shelves on future trends in Antarctic sea ice. *Ann. Glaciol.* **56**, 120–126 (2015).

Boehme, L. et al. Animal-borne CTD-Satellite Relay Data Loggers for realtime oceanographic data collection. *Ocean Sci.* **5**, 685–695 (2009).

Boehme, L., & Rosso, I. Classifying oceanographic structures in the Amundsen Sea, Antarctica. *Geophys. Res. Lett.* **48**, e2020GL08941 (2021).

Bronselaer, B. et al. Importance of wind and meltwater for observed chemical and physical changes in the Southern Ocean. *Nat. Geosci.* **13**, 35–42 (2020).

Charrassin, J. -B., et al. Southern Ocean frontal structure and sea-ice formation rates revealed by elephant seals. *Proc. Natl Acad. Sci. USA* **105**, 11634–11639 (2008).

Chelton, D. B., et al. Geographical variability of the first baroclinic Rossby radius of deformation, *J. Phys. Oceanogr.* **28**, 433–460 (1998).

Coale, K.H., Gordon, R.M., Wang, X., 2005. The distribution and behavior of dissolved and particulate iron and zinc in the Ross Sea and Antarctic circumpolar current along 170°W. *Deep-Sea Res. I* **52**, 295–318.

Davis, P. E. et al. Variability in basal melting beneath Pine Island Ice Shelf on weekly to monthly timescales. *J. Geophys. Res. Oceans* **123**, 8655–8669(2018).

DeConto, R. & Pollard, D. Contribution of Antarctica to past and future sea-level rise. *Nature* **531**, 591–597 (2016).

DeConto, R. M. et al. The Paris Climate Agreement and future sea-level rise from Antarctica, *Nature* **593**, 83–89 (2021).

Dutrieux, P. et al. M. Strong sensitivity of Pine Island ice-shelf melting to climatic variability. *Science* **343**, 174–178 (2014).

Elvidge, A. D. et al. Observations of surface momentum exchange over the marginal ice zone and recommendations for its parametrisation, *Atmos. Chem. Phys.* **16**, 1545–1563 (2016).

Copernicus Climate Change Service, Fifth generation of ECMWF atmospheric reanalyses of the global climate (ERA5). Copernicus Climate Change Service Climate Data Store `https://cds.climate.copernicus.eu/cdsapp#!/home`, (2017).

Fedak, M., Lovell, P., McConnell, B. & Hunter, C. Overcoming the constraints of long range radio telemetry from animals: getting more useful data fromsmaller packages. *Integr. Comp. Biol.* **42**, 3–10 (2002).

Fedak, M. Marine animals as platforms for oceanographic sampling: a“win/win” situation for biology and operational oceanography. *Mem. NatlInst. Polar Res.* **58**, 133–147 (2004).

Fogwill, C. J., Phipps, S. J., Turney, C. S. M. & Golledge, N. R. Sensitivity of the Southern Ocean to enhanced regional Antarctic ice sheet meltwater input. *Earth's Future* **3**, 317–329 (2015).

Foldvik, A., Gammelsrød, T., and Tørresen, T.: Circulation and water masses on the southern Weddell Sea shelf, *Oceanology of the Antarctic continental shelf* **43**, 5–20, (1985).

Gade, H. G. Melting of ice in sea water: a primitive model with application to the Antarctic ice shelf and icebergs. *J. Phys. Oceanogr.* **9**, 189–198 (1979).

Gill, A. (1982) Atmosphere-Ocean Dynamics. *Academic Press, New York*, pp 662.

Greene, C. A. et al. Antarctic calving loss rivals ice-shelf thinning. *Nature* (2022).

Golledge, N. R.et al. Global environmental consequences of twenty-first-century ice-sheet melt, *Nature* **566**, 65–72, (2019).

Heimbach, P. & Losch, M. Adjoint sensitivities of sub-iceshelf melt rates to ocean circulation under the Pine Island Ice Shelf, West Antarctica, *Ann. Glaciol.* **53**, 59–69, (2012).

Hellmer, H., Kauker, F., Timmermann, R., Determann, J. & Rae, J. Twenty-first-century warming of a large Antarctic ice-shelf cavity by a redirected coastal current. *Nature* **485**, 225–228 (2012)

Hersbach, H. et al. ERA5 hourly data on single levels from 1959 to present, Copernicus Climate Change Service (C3S) Climate Data Store (CDS) [data set], `https://doi.org/10.24381/cds.adbb2d47` (2018).

Hersbach, H. et al. The ERA5 global reanalysis. *Q. J. Roy. Meteor. Soc.* **146**,1999–2049 (2020).

Heywood, K. J. et al. Ocean processes at the Antarctic continental slope. *Philos. Trans. R. Soc.* **372**, 20130047 (2014).

Heywood, K. J. et al. Between the devil and the deep blue sea: the role of the Amundsen Sea continental shelf in exchanges between ocean and ice shelves. *Oceanography* **29**, 118–129 (2016).

Hohmann, R., Schlosser, P., Jacobs, S., Ludin, A. & Weppernig, R. Excess helium and neon in the southeast Pacific: Tracers for glacial meltwater. *J.Geophys. Res.Oceans* **107**, 3198 (2002).

Holland, D., Nicholls, K. and Basinski, A. The Southern Ocean and its interaction with the Antarctic Ice Sheet. *Science* **367**, 1326–1330 (2020).

Jacobs, S. S., Jenkins, A., Giulivi, C. F. & Dutrieux, P. Stronger ocean circulation and increased melting under Pine Island Glacier ice shelf. *Nat. Geosci.* **48**, 519 (2011).

Jacobs, S. S. et al. The Amundsen Sea and the Antarctic Ice Sheet. *Oceanogr.* **25**, 154–163 (2012).

Jenkins, A. The impact of melting ice on ocean waters. *J. Phys. Oceanogr.* **29**,2370–2381 (1999).

Jenkins, A. et al. Observations beneath Pine Island Glacier in West Antarctica and implications for its retreat. *Nat. Geosci.* **3**, 468–472 (2010).

Jenkins, A. et al. West Antarctic Ice Sheet retreat in the Amundsen Sea driven by decadal oceanic variability. *Nat. Geosci.* **11**, 733–738 (2018).

Jones, R. W., et al. Evaluation of four global reanalysis products using in situ observations in the Amundsen Sea Embayment, Antarctica. *J. Geophys. Res. Atm.* **121**, 6240–6257 (2016).

Jourdain, N. C. et al. Ocean circulation and sea-ice thinning induced by melting ice shelves in the Amundsen Sea. *J. Geophys. Res. Oceans* **122**, 2550–2573 (2017).

Jourdain, N. C. et al. Simulating or prescribing the influence of tides on the Amundsen Sea ice shelves, *Ocean Model.* **133**, 44–55, (2019).

Kim, I. et al. The distribution of glacial meltwater in the Amundsen Sea,Antarctica, revealed by dissolved helium and neon. *J. Geophys. Res. Oceans* **121**, 1654–1666 (2016).

Kim, T. et al. Interannual Variation of Modified Circumpolar Deep Water in the Dotson-Getz Trough, West Antarctica. *J. Geophys. Res. Oceans* **126**, e2021JC017491 (2021).

Kimura, S. et al. Ocean mixing beneath Pine Island Glacier ice shelf. WestAntarctica. *J. Geophys. Res. Oceans* **121**, 8496–8510 (2016).

Kimura, S. et al. Oceanographic controls on the variability of ice-shelf basal melting and circulation of glacial meltwater in the Amundsen SeaEmbayment. Antarctica. *J. Geophys. Res. Oceans* **122**, 10131–10155 (2017).

Lago. V & England, M. Projected Slowdown of Antarctic Bottom Water Formation in Response to Amplified Meltwater Contributions.*J. Clim.* **32**, 6319–6335 (2019).

Lazarevich, P., Stoermer, S., 2001. A Matlab version of the Price, Weller, Pinkel model. `http://www.po.gso.uri.edu/rafos/research/pwp/`.

Lazarevich, P., Rossby, T. & McNeil, C. Oxygen variability in the near-surface waters of the northern North Atlantic: observations and a model. *J. Mar. Res.* **62** 663–683 (2004).

Le, Brocq et al. Evidence from ice shelves for channelized meltwater flow beneath the Antarctic Ice Sheet. *Nat. Geosci.* **6**, 945–948 (2013).

Loose, B., Schlosser, P., Smethie, W. M. & Jacobs, S. An optimized estimate of glacial melt from the Ross Ice Shelf using noble gases, stable isotopes, and CFCtransient tracers. *J. Geophys. Res. Oceans* **114**, C8 (2009).

Loose, B. & Jenkins, W. J. The five stable noble gases are sensitive unambiguous tracers of glacial meltwater. *Geophys. Res. Lett.* **41**, 2835–2841 (2014).

Loose, B. et al. Estimating the recharge properties of the deep ocean using noble gases and helium isotopes. *J. Geophys. Res. Oceans* **121**, 5959–5979 (2016).

Loose, B. et al. Evidence of an active volcanic heat source beneath the PineIsland Glacier. *Nat. Commun.* **9**, 1–9 (2018).

Lott, D. E. Improvements in noble gas separation methodology: a nude cryogenic trap. *Geochem. Geophys. Geosyst.* **2**, 2001GC000202 (2001).

Liu, A.Q., The effect of the sea-ice zone on the development of boundary-layer roll clouds during cold air outbreaks. *Bound-Lay. Meteorol.* **118(3)**, 557–581(2006).

Mackie, S., Smith, I. J., Ridley, J. K., Stevens, D. P. & Langhorne, P. J. Climate response to increasing Antarctic iceberg and ice shelf melt. *J. Clim.* **33**, 8917–8938 (2020).

Mallett, H. K. W. et al. Variation in the Distribution and Properties of Circumpolar Deep Water in the Eastern Amundsen Sea, on Seasonal Timescales, Using Seal-Borne Tags. *Geophys. Res. Lett.* **45**, 4982–4990 (2018).

Mankoff, K. D., Jacobs, S. S., Tulaczyk, S. M. & Stammerjohn, S. E. The role of Pine Island Glacier ice shelf basal channels in deep-water upwelling, polynyas and ocean circulation in Pine Island Bay, Antarctica. *Ann. Glaciol.* **53**, 123–128 (2012).

Mathis, J. T. et al. Determining net dissolved organic carbon production in the hydrographically complex western Arctic Ocean, *Limnol. Oceanogr.* **52**, 1789–1799, (2007).

Mathiot, P., Jenkins, A., Harris, C., & Madec, G. Explicit representation and parametrised impacts of under ice shelf seas in the z–coordinate ocean model NEMO 3.6, *Geosci. Model Dev.* **10**, 2849–2874, (2017).

Martin, S. and Kauffman, P.: A field and laboratory study of wave damping by grease ice. *J. Glaciol.* **27**, 283–313 (1981).

Martin, T., Steele, M., & Zhang, J. Seasonality and long-term trend of Arctic Ocean surface stress in a model, *J. Geophys. Res. Oceans* **119**, 1723–1738, (2014).

Mazur, A. K., Wåhlin, A. K & Kręzel, A. An object-based SAR image iceberg detection algorithm applied to the Amundsen Sea. *Remote Sensing of Environment* **189**, 67–83 (2017).

Meredith, M., et al. Polar Regions. Chapter 3, *IPCC Special Report on the Ocean and Cryosphere in a Changing Climate.* (2019).

McDougall, T. J. & Barker, P. M. Getting started with TEOS-10 and the Gibbs Seawater (GSW) oceanographic toolbox. *SCOR/IAPSO WG* **127**, 1–28 (2011).

Meneghello, G., Marshall, J., Campin, J. M., Doddridge, E., & Timmermans, M. L. The ice-ocean governor: Ice-ocean stress feedback limits Beaufort Gyre spin-up, *Geophys. Res. Lett.* **45**, 11293–11299, (2018).

Meneghello, G. et al. Genesis and decay of mesoscale baroclinic eddies in the seasonally ice-covered interior Arctic Ocean, *J. Phys. Oceanogr.* **51**, 115–129, (2021).

Meredith, M. et al. Seasonal evolution of the upper-ocean adjacent to the South Orkney Islands, Southern Ocean: Results from a "lazy biological mooring". *Deep Sea Res. Part II* **58**, 1569–1579 (2011).

Nakayama, Y., Schröder, M. & Hellmer, H. H. From circumpolar deep water to the glacial meltwater plume on the eastern Amundsen Shelf. *Deep Sea Res. Part I* **77**, 50–62 (2013).

Nakayama, Y., Timmermann, R., Rodehacke, C. B., Schröder, M. & Hellmer, H. H. Modeling the spreading of glacial meltwater from the Amundsen and Bellingshausen Seas. *Geophys. Res. Lett.* **41**, 7942–7949 (2014).

Nakayama, Y., Menemenlis, D., Zhang, H., Schodlok, M. & Rignot, E. Originof circumpolar deep water intruding onto the Amundsen and BellingshausenSea continental shelves. *Nat. Commun.* **9**, 1–9 (2018).

Nakayama, Y. et al. Pathways of ocean heat towards Pine Island and Thwaites grounding lines, *Sci. Rep.-UK* **9**, 16649, (2019).

Naveira Garabato, A. C. et al. Vigorous lateral export of the meltwater outflow from beneath an Antarctic ice shelf. *Nature* **542**, 219–222 (2017).

Paolo, F. S., Fricker, H. A. & Padman, L. Volume loss from Antarctic ice shelves is accelerating. *Science* **348**, 327–331 (2015).

Pattyn, F. & Morlighem, M. The uncertain future of the Antarctic Ice Sheet. *Science* **367**, 1331–1335 (2020).

Payne, A. J. et al. Numerical modeling of ocean-ice interactions under PineIsland Bay's ice shelf. *J. Geophys. Res. Oceans* **112**, C10 (2007).

Pellichero, V., J.-B. Sallée, S. Schmidtko, F. Roquet, & J.-B. Charrassin The ocean mixed layer under Southern Ocean sea-ice: Seasonal cycle andforcing. *J. Geophys. Res. Oceans* **122**, 1608–1633, (2017).

Porter, D. et al. Evolution of the seasonal surface mixed layer of the Ross Sea, Antarctica, observed with autonomous profiling floats. *J. Geophys. Res. Oceans* **124**, 4934–4953 (2018).

Photopoulou, T., Fedak, M. A., Matthiopoulos, J., McConnell, B. & Lovell, P.The generalized data management and collection protocol for conductivitytemperature-depth satellite relay data loggers. *Animal Biotelem.* **3**, 21 (2015).

Price, J. F., Weller, R. A. & Pinkel, R. Diurnal Cycling: Observations and Models of the Upper Ocean Response to Diurnal Heating, Cooling and Wind Mixing. *J. Geophys. Res.* **91**, 8411–8427 (1986).

Pritchard, H. et al. Antarctic ice-sheet loss driven by basal melting of ice shelves. *Nature* **484**, 502–505 (2012).

Poulton, S. W. & Raiswell, R. Chemical and physical characteristics of iron oxides in riverine and glacial meltwater sediments. *Chem. Geolog.* **218**, 203–221 (2005).

Queste, B. Y. & Wåhlin, A. K. CTD data from the NBP 19/02 cruise as part of the NERC-NSF ITGC TARSAN project in the Amundsen Sea, campaign during austral summer 2018/2019, NERC EDS British Oceanographic Data Centre (NOC) [data set], `https://doi.org/10.5285/e338af5d-8622-05dee053-6c86abc06489`, (2022).

Randall-Goodwind, E. et al. Freshwater distributions and water mass structure in the Amundsen Sea Polynya region, Antarctica. *Elementa: Science of the Anthropocene* **3**, (2015).

Regan, H., Lique, C., Talandier, C., & Meneghello, G. Response of total and eddy kinetic energy to the recent spinup of the Beaufort Gyre, *J. Phys. Oceanogr.* **50**, 575–594, (2020).

Rignot, E. et al. Four decades of Antarctic Ice Sheet mass balance from 1979–2017. *Proc. Natl Acad. Sci. USA* **116**, 1095–1103 (2019).

Robel, A. A., Wilson, E., & Seroussi, H. Layered seawater intrusion and melt under grounded ice. *The Cryosphere* **16**, 451–469, (2022).

Robin Robertson, Tidally induced increases in melting of Amundsen Sea ice shelves. *J. Geophys. Res. Oceans* **118**, 3138–3145 (2013).

Roquet, F. et al. Estimates of the Southern Ocean general circulation improved by animal-borne instruments. *Geophys. Res. Lett.* **40**, 6176–6180 (2013).

Roquet, F. et al. A Southern Indian Ocean database of hydrographic profiles obtained with instrumented elephant seals. *Sci. Data* **1**, 140028 (2014).

Scambos, T. A. et al. Detailed ice loss pattern in the northern Antarctic Peninsula: widespread decline driven by ice front retreats, *The Cryosphere* **8**, 213–2145 (2014).

Schaffer, J. & Timmermann, R. An update to Greenland and Antarctic ice sheet topography, cavity geometry, and global bathymetry (RTopo-2.0.4). PANGAEA, `https://doi.org/10.1594/PANGAEA.905295` (2019).

Schodlok, M. P., Menemenlis, D., Rignot, E. & Studinger, M. Sensitivity of the ice-shelf/ocean system to the sub-ice-shelf cavity shape measured by NASA IceBridge in Pine Island Glacier, West Antarctica. *Ann. Glaciol.* **53**, 156–162 (2012).

Shepherd, A. et al. Mass balance of the Antarctic Ice sheet from 1992 to 2017. *Nature* **558**, 219–222 (2018).

Silvano, A., Rintoul, S. R., Peña-Molino, B. & Williams, G. D. Distribution of water masses and meltwater on the continental shelf near the Totten andMoscow University ice shelves. *J. Geophys. Res. Oceans* **122**, 2050–2068(2017).

Silvano, A. et al. Freshening by glacial meltwater enhances melting of ice shelves and reduces formation of Antarctic Bottom Water. *Sci. Adv.* **4**, eaap9467 (2018).

Spensberger, C. & Spengler, T. Sensitivity of Air-Sea Heat Exchange in Cold-Air Outbreaks to Model Resolution and Sea-Ice Distribution. *J. Geophys. Res. Atmos.* **126(5)**, e2020JD033610 (2021).

Stammerjohn, S. E., et al. Seasonal sea ice changes in the Amundsen Sea, Antarctica, over the period of 1979–2014Seasonal sea ice changes in the Amundsen Sea. *Elementa: Science of the Anthropocene* **3** (2015).

Stanley, R. H., Jenkins, W. J., Lott, D. E. III. & Doney, S. C. Noble gas constraints on air-sea gas exchange and bubble fluxes. *J. Geophys. Res. Oceans* **114**, C11 (2009).

Steiger, N., Darelius, E., Wåhlin, A. K., & Assmann, K. M. Intermittent reduction in ocean heat transport into the Getz Ice Shelf cavity during strong wind events. *Geophys. Res. Lett.* **48**, e2021GL093599 (2021).

St-Laurent, P., Klinck, J. M., & Dinniman, M. S. Impact of local winter cooling on the melt of Pine Island G lacier, Antarctica. *J. Geophys. Res. Oceans* **120**, 6718–6732, (2015).

St-Laurent, P. Yager, P., Sherrel, R., Stammerjohn, S. & Dinniman, M. Pathways and supply of dissolved iron in the Amundsen Sea (Antarctica). *J. Geophys. Res. Oceans* **122**, 7135–7162 (2017).

St-Laurent, P. et al. Modeling the seasonal cycle of iron and carbon fluxes in the Amundsen Sea Polynya, Antarctica. *J. Geophys. Res. Oceans* **124**, 1544–1565 (2019).

Stommel, H. The westward intensification of wind-driven ocean currents. *EOS T. Am. Geophys. Union* **29**, 202–206, (1948).

Smith, N. R., Zhaoqian, D., Kerry, K. R., & Wright, S Water masses and circulation in the region of Prydz Bay, Antarctica. *Deep-Sea Res. Pt. I* **31**, 1121–1147, (1984).

Tamura, T., Ohshima, K. I. & Nihashi, S. Mapping of sea ice production forAntarctic coastal polynyas. *Geophys. Res. Lett.* **35**, 7 (2008).

Tamura, T., Ohshima, K. I., Nihashi, S. & Hasumi, H. Estimation of surface heat/salt fluxes associated with sea ice growth/melt in the Southern Ocean. *Sci.Online Lett. Atmos.* **7**, 17–20 (2011).

Thurnherr, A. M., Jacobs, S. S., Dutrieux, P. & Giulivi, C. F. Export and circulation of ice cavity water in Pine Island Bay. West Antarctica. *J. Geophys. Res.* **119**, 1754–1764 (2014).

Tortell, P. D. et al. Spatial distribution of pCO2, δO2/Ar and dimethylsulfide (DMS) in polynya waters and the sea ice zone of the Amundsen Sea, Antarctica. *Deep-Sea Res. Pt. II* **71**, 77–93, (2012).

Turner, J. et al. (2022). Record low Antarctic sea ice cover in February 2022. *Geophys. Res. Lett.* **49**, e2022GL098904 (2022).

Wadhams, P. et al. (2018). Pancake ice thickness mapping in the Beaufort Sea from wave dispersion observed in SAR imagery. *Journal of Geophysical Research: Oceans.* **123(3)**, 2213-2237 (2018).

Wåhlin, A. K. et al. Subinertial Oscillations on the Amundsen Sea Shelf, Antarctica. *J. Phys. Oceanogr.* '46, 3573–2582, (2016).

Wåhlin, A. K. et al. Pathways and modification of warm water flowing beneath Thwaites Ice Shelf, West Antarctica. *Sci. Adv.* **7**, eabd7254, (2021).

Webber, B. G. et al. Mechanisms driving variability in the ocean forcing of Pine Island Glacier. *Nat. Commun.* **8**, 1–8, (2017).

Webber, B. G., Heywood, K. J., Stevens, D. P. & Assmann, K. M. The impact of overturning and horizontal circulation in Pine Island Trough on ice shelf melt in the eastern Amundsen Sea. *J. Phys. Oceanogr.* **49**, 63–83 (2019).

Yager, P. L. et al. A carbon budget for the Amundsen Sea Polynya, Antarctica: Estimating net community production and export in a highly productive polar ecosystemAmundsen Sea Polynya carbon budget. *Elementa: Science of the Anthropocene* **4** (2016).

Yang, H. W. et al. Seasonal variability of ocean circulation near the Dotson Ice Shelf, Antarctica. *Nat. Commun.* **13**, 1138 (2022).

Yoon, S. T. et al. Ice front retreat reconfigures meltwater-driven gyres modulating ocean heat delivery to an Antarctic ice shelf. *Nat. Commun.* **13**, 1–8, (2022).

Zhao, M., M.-L. Timmermans, S. Cole, R. Krishfield, A. Proshutinsky, and J. Toole Characterizing the eddy field in the Arctic Ocean halocline. *J. Geophys. Res. Oceans* **119**, 8800–8817 (2014).

Zheng, Y. et al. Winter seal-based observations reveal glacial meltwater surfacing in the southeastern Amundsen Sea. *Communications: Earth & Environment* 2, 1–9, (2021).

Zheng, Y., Stevens, D. P., Heywood, K. J., Webber, B. G. M., & Queste, B. Y. Reversal of ocean gyres near ice shelves in the Amundsen Sea caused by the interaction of sea ice and wind. *The Cryosphere* **16**, 3005–3019, (2022).

Zheng, Y. et al. Shipborne ADCP data in the Thwaites Gyre region 2019. *Zenodo* [data set], `https://doi.org/10.5281/zenodo.6757570`, (2022).

Zheng, Y. et al. An Idealised Barotropic Ocean Gyre Model Code, Based on MITgcm. *Zenodo* [data set], `https://doi.org/10.5281/zenodo.6757626`, (2022).